

# Drone Flow User Guide

**Prepared by: H. J. Biggs, National Institute of Water and Atmospheric Research (NIWA), Christchurch, New Zealand**

Email: [Hamish.Biggs@niwa.co.nz](mailto:Hamish.Biggs@niwa.co.nz), Phone: +64 3 3437843

Version:	1.1
Release date:	29/06/2022
Link to GitHub repository:	<a href="https://github.com/HamishBiggs/DroneFlow">https://github.com/HamishBiggs/DroneFlow</a>
Citation:	Biggs, H.J. (2022). <i>Drone Flow User Guide</i> , NIWA, Christchurch, New Zealand.

## Summary

‘Drone flow’ is a MBIE Smart Ideas project that has been developing novel hardware, methods and software for Aerial Image Velocimetry (AIV), physical habitat mapping, and remote sensing of rivers. This user guide provides: a general introduction (Section 1); the hardware developed and deployed by the ‘drone flow’ project (Section 2); mission planning for fieldwork (Section 3); ‘drone flow’ measurement methods (Section 4); summary of general advice for improving surface image velocimetry measurements (Section 5); conclusions (Section 6); future recommendations (Section 7); and Appendices. The user guide provides an overview of a wide range of remote sensing methods that are applicable in rivers and is likely to be a useful starting point for those commencing work in this area. Included is information on which methods are: practical, impractical, or require further development, and where the different methods are likely to be suitable. The ‘drone flow’ project was originally conceived as a single remote sensing ‘system’, where two drones would fly simultaneously, with the upstream drone dropping tracer particles, while the downstream drone recorded surface velocities with a stereoscopic camera. This system was successfully developed and is included in this user guide, however, this ‘one size fits all’ approach was not really applicable to the wide range of channel types, flow conditions, deployment objectives, and environmental noise that were encountered. As such, ‘drone flow’ would be better considered to be a toolbox of hardware, software, and methods for a range of river remote sensing tasks. The appendices of this user guide provide an overview of the files that have been released through a GitHub project repository (including both CAD files for hardware development and open source software). The ‘drone flow’ project has been supported by a large team consisting of staff from NIWA, collaborators/stakeholders in New Zealand, and international collaborators. The work of the whole team is gratefully acknowledged.

## Contents

Summary: .....	1
Contents .....	2
Figures.....	4
Tables .....	8
1         Introduction .....	10
1.1     Motivation.....	10
1.2     Background - Remote sensing of river flow and bathymetry .....	10
1.3     Limitations of existing methods.....	11
1.4     Drone flow approach .....	12
1.5     User guide contents .....	15
2         Drone flow hardware.....	17
2.1     Cameras .....	17
2.1.1     RGB camera/gimbal modules.....	17
2.1.2     RGB stereoscopic camera .....	19
2.1.3     Hyperspectral camera .....	29
2.1.4     Underwater cameras .....	34
2.2     Drones.....	36
2.2.1     DJI Phantom 4 Pro .....	36
2.2.2     DJI Matrice 210.....	37
2.2.3     DJI Matrice 600 Pro .....	38
2.2.4     Aeronavics Skyjib .....	39
2.3     Tracer particles .....	41
2.3.1     Tracer particle selection .....	41
2.3.2     Dying tracer particles.....	44
2.3.3     Thresholding tracer particles to reduce environmental noise .....	46
2.3.4     Tracer particle distribution system.....	47
2.4     Surveying equipment.....	53
2.4.1     RTK GPS.....	53
2.4.2     Ground Control Points (GCPs) – Terrestrial.....	54
2.4.3     Ground Control Points (GCPs) – Underwater.....	56
2.4.1     Ground Control Points (GCPs) – Thermal infrared .....	57
2.5     Other equipment .....	58
2.5.1     Acoustic Doppler Current Profiler (ADCP) .....	58
2.5.2     ADCP benthic lander.....	59
2.5.3     Depth sounder.....	61
2.5.4     Ground Penetrating Radar (GPR) .....	62
2.5.5     Wind measurements .....	66

2.5.6	Mark Forged X7 3D printer.....	69
2.5.7	Miscellaneous.....	69
3	Mission planning.....	71
3.1	Site selection .....	71
3.2	CAA regulations.....	71
3.3	Deployment conditions.....	71
3.4	Ground control points and surveying .....	72
3.5	Flight planning.....	72
4	'Drone flow' measurement methods.....	74
4.1	Surface velocities (nadir from a drone) .....	74
4.2	Surface velocities (oblique from riverbanks) .....	76
4.3	Surface velocities (oblique from drones).....	77
4.4	Surface velocities from multiple sections for wide rivers and flood gauging.....	78
4.5	Aerial surveys of rivers (terrestrial regions).....	79
4.5.1	Georeferenced orthomosaics and DSMs.....	79
4.5.2	DEMs with drone mounted LiDAR.....	81
4.6	Underwater imagery surveys of clear rivers (wetted regions) .....	82
4.7	Bathymetry .....	83
4.7.1	ADCP – Moving boat cross sections .....	84
4.7.2	ADCP – Section-by-Section (SxS Pro).....	86
4.7.3	ADCP – Depth sounder and RTK GPS.....	87
4.7.4	Underwater imagery .....	88
4.7.5	Ground Penetrating Radar (GPR) .....	90
4.7.6	Water colour and spectral attenuation.....	93
4.7.7	Through water imagery corrected for surface refraction .....	96
4.7.8	Bathymetric LiDAR.....	97
4.7.9	Other techniques for bathymetry .....	99
4.7.10	Summary of practicality of bathymetry techniques .....	100
4.8	Surface velocity to depth averaged velocity (alpha).....	101
4.8.1	Wind effects on surface velocimetry.....	104
4.9	Sediment size estimation from imagery .....	105
5	Summary of general advice for improving surface image velocimetry measurements .....	108
6	Conclusions .....	110
7	Future work .....	111
	Acknowledgments.....	112
	Amendments .....	113
	References .....	114

Glossary .....	124
Appendix A : Drone flow toolbox – GitHub repository .....	127
Appendix B : Stereoscopic camera acquisition software and config settings for BFS-U3-51S5C-C cameras.....	129
Appendix C : Cross sections from moving boat ADCP gaugings .....	131
Appendix D : CAD files of ‘drone flow’ hardware .....	135
Appendix E : Camera and flight parameter calculator.....	138

## Figures

Figure 1.1: a) New Zealand rivers with mean annual flow greater than 1 m <sup>3</sup> /s; b) manual discharge gauging with an Acoustic Doppler Current Profiler (ADCP); c) automated discharge gauging with an ADCP; d) braided rivers are not well suited for ADCP gauging and pose safety issues for human operators crossing channels at higher discharges; e) Rakaia gorge during a flood, where ADCP gauging struggles due to high river velocity, floating debris, river depth and mobile bed materials (image Ashburton Guardian, 2013).	10
Figure 1.2: Drone formation flying where the upstream drone (yellow circle) scatters biodegradable tracer particles which are recorded by the downstream drone to resolve surface velocity fields.	14
Figure 1.3: Stereoscopic camera and tracer particle distribution system on 2x DJI M600 drones during a deployment in the Tekapo Canal, New Zealand.	14
Figure 1.4: Tracer particle distribution system in the Rangitata River, New Zealand.	15
Figure 1.5: Stereoscopic camera system during deployment in the Tekapo Canal, New Zealand.	15
Figure 2.1: (a) DJI Phantom 4 Pro RGB Camera, (b) DJI Zenmuse X5S RGB Camera.	17
Figure 2.2: Sony A5100 with Voigtlander 15 mm lens on Aeronavics Skyjib, with X-Cam A22-2H 2-axis gimbal. Showing the front of the aircraft (a), and the left side of the aircraft (b).	18
Figure 2.3: Stereoscopic camera system, with aluminium chassis, fibreglass top and side panels, and 3D printed mounting bracket.	19
Figure 2.4: Stereoscopic camera system with top plate and front face removed to show the top layer of internal components.	21
Figure 2.5: Stereoscopic camera system with bottom plate and front face removed to show the bottom layer of internal components.	21
Figure 2.6: Left: DJI M600 remote controller with channel expansion kit, used for triggering image recording by the stereoscopic camera; Right: PWM outputs from the A3 flight controller.	22
Figure 2.7: Chart showing the frame rate achievable with a single BFS-U3-S1S5 camera (in mono) as a function of image resolution. Maximum quoted frame rate is 75 FPS in mono at 2448 × 2048 resolution.	23
Figure 2.8: After successful synchronisation left camera (a) and right camera (b) images have no lag and can capture synchronous images of wind vane propellers spinning and bird wings flapping mid-flight.	24
Figure 2.9: Images of 8x7 checkerboard target with (a) left camera, and (b) right camera.	24
Figure 2.10: Example of stereoscopic camera calibration in MATLAB to evaluate intrinsic stereoscopic camera parameters.	25

Figure 2.11: Stereoscopic camera deployment in the Ashley River, New Zealand.	26
Figure 2.12: Stereoscopic camera deployment in the Rangitata River, New Zealand.	26
Figure 2.13: Stereoscopic camera setup in the Tekapo Canal, New Zealand.	27
Figure 2.14: Stereoscopic camera deployment in the Tekapo Canal, New Zealand.	27
Figure 2.15: Stereoscopic camera oblique deployment on a tripod in the Rangitata River, New Zealand.	28
Figure 2.16: (a) Headwall Nano-Hyperspec, (b) Resonon Pika L Airborne System.	30
Figure 2.17: Initial configuration of the Resonon Pika L hyperspectral camera on a DJI M600 drone, with rigid mounting, dual antenna booms, and downwelling irradiance sensor (what not to do!).	31
Figure 2.18: Recommended Resonon Pika L Hyperspectral Camera deployment configuration on a DJI Ronin MX Gimbal, with full shielding of the SSD and all USB3 plugs.	33
Figure 2.19: Resonon Pika L hyperspectral camera during deployments in the Avon-Heathcote Estuary in New Zealand.	34
Figure 2.20: EKEN H9R (left) and GoPro HERO9 (right) underwater cameras.	35
Figure 2.21: Left: EKEN H9R camera and LED ring light on a survey pole to collect underwater imagery for high resolution bathymetric mapping. Right: LED ring light and EKEN H9R camera.	35
Figure 2.22: DJI Phantom 4 Pro drone with integrated RGB camera/gimbal module.	37
Figure 2.23: DJI Matrice 210 (left), with a simple rain shield for the X5S camera and gimbal (right).	38
Figure 2.24: DJI Matrice 600 Pro drone used for most heavy lift payloads (up to 5 kg) during the ‘drone flow’ project.	39
Figure 2.25: Aeronavics Skyjib with the Sony A5100 RGB camera and X-Cam A22-2H gimbal in the Rangitata River, New Zealand.	40
Figure 2.26: Aeronavics Skyjib with the stereoscopic camera system in the Rangitata River, New Zealand.	40
Figure 2.27: Field tests of tracer particles in the Halswell River, New Zealand. Plain wood shavings are visible at the top of the image, while coloured wood shavings (light pink) are visible in the centre of the image.	42
Figure 2.28: (a) Large bag of wood shavings from ‘Kiwi Wood Shavings Ltd’, (b) plain wood shavings are easily distinguishable against a background of darker river water.	42
Figure 2.29: ‘Sierra Red’ mulch dye from EnviroColor Ltd, which is applied to faded bark chips (or wood shavings in our case) using a backpack sprayer after being diluted with water.	44
Figure 2.30: Preparing batches of coloured wood shavings by dying them with ‘Sierra Red’ mulch dye.	45
Figure 2.31: Left: Deployment of coloured tracer particles in the Waingawa River, New Zealand. Right: Zoomed example of coloured tracer particles in the Ashley River, New Zealand, where environmental noise due to sunglint and reflections off surface waves, as well as dappled lighting on the riverbed make it very challenging to resolve plain tracer particles (i.e. brightness is not suitable for separation).	45
Figure 2.32: (a) Coloured tracer particles and surface sunglint (Ashley River, New Zealand); (b) visualisation of all the image data in the HSV colour space; (c) thresholded image to only resolve the tracer particles; (d) visualisation of the thresholded image data in the HSV colour space.	46
Figure 2.33: Steel prototype of the first tracer particle distribution system design (with two counter rotating screw augers) during benchtop testing (a), and outdoor testing under a DJI M600 drone (b).	47

Figure 2.34: The final tracer particle distribution system design (featuring three screw augers): (a) oblique view, (b) section view, (c) front view, (d) top view, (e) side dimensions, (f) front dimensions.	48
Figure 2.35: (a) Final construction of the tracer particle distribution system and loading with wood shavings, (b) motor, gearbox, speed controller and bearing assembly, (c) the full system ready for field deployment.	49
Figure 2.36: The RC unit for the DJI M600 drone has a channel expansion kit, with a rotary switch used to control the feed rate of the tracer particle distribution system, through a PWM output from the DJI A3 flight controller to the speed controller on the tracer particle distribution system.	49
Figure 2.37: Tracer particle distribution system during laboratory testing of feed rates.	50
Figure 2.38: NIWA field technician Hamish Sutton loads the tracer particle distribution system in the Rangitata River, New Zealand, before a surface velocimetry mission.	51
Figure 2.39: Tracer particle distribution system in the Rangitata River, New Zealand.	52
Figure 2.40: The descending cloud of tracer particles, with individual wood shavings being visible.	52
Figure 2.41: Deployment of the tracer particle distribution system in the Tekapo Canal, New Zealand.	53
Figure 2.42: (a) Trimble R10 RTK GPS base station, (b) 2x Trimble R10 Rovers.	54
Figure 2.43: Ground control points that are easily visible in aerial imagery and have a clear centre to survey (Biggs, 2020).	55
Figure 2.44: Plain GCP with large numbers (left); coloured GCP with numbers and a well-defined centre for surveying, suitable for canvas (centre) or paper with corners holes cut out before lamination (right).	55
Figure 2.45: (a) Tests to select underwater Ground Control Point (GCP) colour. (b) Underwater GCP deployed in the Hutt River.	56
Figure 2.46: Using 25 mm stainless steel square washers as underwater GCPs.	57
Figure 2.47: Aluminium GCPs for thermal infrared remote sensing and mapping.	57
Figure 2.48: (a) Teledyne River Pro ADCP deployed in the Tekapo Canal in New Zealand, with a drogue for stabilisation and a flying fox traveller for consistent lateral velocity.	58
Figure 2.49: Aluminium stabilisation frame for River Pro ADCP to maintain orientation orthogonal to the cross section (left). Deployment of the ADCP and stabilisation frame in a hydro-power canal in New Zealand for wind and velocity profile measurements (right).	59
Figure 2.50: Design of the stainless-steel base plate and mounting brackets in Autodesk Inventor.	60
Figure 2.51: Up looking ADCP benthic lander following a 35 day deployment in the Tekapo hydro-canal. The ADCP benthic lander consists of a stainless-steel baseplate, Nortek Signature ADCP, battery, and Nortek Aquadopp ADCP.	60
Figure 2.52: Deployment of ADCP benthic lander in the Tekapo Canal from an inflatable boat.	61
Figure 2.53: Tritech PA500 depth sounder connected to Trimble R10 RTK GPS Rover and mounted on an ADCP boat hull.	62
Figure 2.54: MALÅ GeoDrone80 mounted on a DJI M600 drone and deployed in the Rangitata River, New Zealand for cross sections of bathymetry.	63
Figure 2.55: MALÅ GeoDrone80 mounted on a DJI M600 drone and deployed in the Waimakariri River, New Zealand for cross sections of bathymetry during a flood.	64
Figure 2.56: Using nadir FPV aerial imagery from a DJI M210 drone flown by a second pilot to fine tune proximity to the far bank of the river (river width and distance from the pilots is ~300 m).	65
Figure 2.57: Left: Basic handheld anemometer (ProTech QM1646) for characterising wind conditions during surface velocity measurements; Right: Vaisala WXT536 climate station for 2D	

measurements of wind velocities, with complementary measurements of temperature, pressure, and relative humidity.	67
Figure 2.58: NIWA field technicians Alec Dempster and Hamish Sutton deploy a River Pro ADCP and Vaisala WXT536 in a hydropower canal in New Zealand for measurements of the effect of wind on velocity profiles and surface velocities.	67
Figure 2.59: Wind tower deployed at the Tekapo Canal for long duration measurements of wind velocity profiles and turbulence, using 3x CSAT3B sonic anemometers.	68
Figure 2.60: Deployment of the Wind Tower (3x CSAT3B) and Climate Station (WXT536) for long term measurements of wind velocity profiles and turbulence in the Tekapo Canal. The WXT536 provided the complementary data required to calculate air density from temperature, pressure, and relative humidity.	68
Figure 2.61: Mark Forged X7 3D printer producing an end plate for the tracer particle distribution system.	69
Figure 4.1: Aerial tracer particle distribution system in the Rangitata River, New Zealand.	74
Figure 4.2: Surface velocities in the Hurunui River from STIV, processed with Hydro-STIV.	75
Figure 4.3: Surface velocities and GCPs in the Makarewa River at a fixed camera gauging site developed by Michael McDonald from Environment Southland during collaboration on the ‘drone flow’ project.	76
Figure 4.4: Wider channels can be divided into sections for nadir surface velocimetry measurements. Flood flow measurements in the Waimakariri River, New Zealand @ $813.7 \text{ m}^3/\text{s}$ .	79
Figure 4.5: Aerial imagery processing with Agisoft Metashape (Waingawa River, New Zealand). Blue rectangles are camera locations.	81
Figure 4.6: Lightweight terrestrial LiDAR from LiDAR USA (model Snoopy). Provides a convenient way to obtain digital elevation models of river reaches. LiDAR can penetrate through sparse vegetation canopies to resolve underlying terrain features.	82
Figure 4.7: Underwater orthomosaic from the Waingawa River, with underwater GCPs comprised of metal washers with holes in them, surveyed in with RTK GPS.	83
Figure 4.8: ADCP moving boat transects for cross section bathymetry (Tekapo Canal, New Zealand).	84
Figure 4.9: Left: ADCP displacement during a transect. Right: Cross section after vector projection of North/East displacement onto cross section unit vector, and resampling (linear interpolation) of depth.	85
Figure 4.10: Left: Rescaling of linear displacement to account for drift in distance sources. Width can be manually measured and entered, or an ADCP distance source can be used (VTG in this case). Right: Multiple transects are overlain, then averaged to improve the accuracy of the result (black dashed line) and exported as a .csv file. Example data from the Tekapo Canal in New Zealand.	86
Figure 4.11: RTK GPS measurement points are projected onto the cross section unit vector.	88
Figure 4.12: The cross section and depth measurements are linearly interpolated and smoothed with a 5 point moving average.	88
Figure 4.13: Tiled 3D model in the Waingawa River, derived from underwater imagery, with underwater GCPs comprised of metal washers, that were surveyed with RTK GPS.	89
Figure 4.14: Zoomed example of a tiled 3D model (left) and a 3D solid model (right) in the Waingawa River. DEMs and 3D models from underwater imagery are a useful way to map river bathymetry.	90
Figure 4.15: Flood gauging in the Waimakariri River in New Zealand, with aerial GPR used for cross section bathymetry.	90

Figure 4.16: GPS locations of measured GPR data, which are then projected onto the cross section and linearly interpolated.	91
Figure 4.17: Projection of data onto the cross section is important to account for the drone flight path (not perfectly straight) and to remove any small loops. Data are then sorted by cross stream displacement and linearly interpolated.	91
Figure 4.18: Cross section from aerial GPR in the Waimakariri River, New Zealand.	92
Figure 4.19: Comparison of surface velocities from STIV, depth from GPR, and cross stream distance (from the true left to the true right bank) in the Waimakariri River, New Zealand.	92
Figure 4.20: Braided gravel bed rivers such as the Rakaia River in New Zealand are suitable for estimation of bathymetry from colour during periods of relatively low flows. At higher flows turbidity increases and signals saturate, limiting the maximum detectable depth. (Image from Dave Allen)	94
Figure 4.21: Workflow diagram for selecting the alpha estimation method from Biggs <i>et al.</i> , (2021).	104
Figure 4.22: Grain size analysis with BASEGRAIN (Detert & Weitbrecht, 2013).	106
Figure 4.23: High resolution underwater georeferenced orthomosaic (Waingawa River, New Zealand).	107
Figure 4.24: Grain size analysis of underwater sediment including 3D spatial data (Detert <i>et al.</i> , 2019b), showing: 3D model derived from underwater imagery (a); segmented 3D model based on analysis of the 2D orthomosaic in BASEGRAIN (b); fitting ellipsoids to the segmented 3D points (c); comparison of size distribution with BASEGRAIN in 2D (blue line) and 3D (red line) (d).	107
Figure 5.1: NIWA environmental monitoring technician Hamish Sutton flying a tracer particle distribution system in the Tekapo Canal (left) and Rangitata River (right).	109
Figure 6.1: Surface velocity measurements with tracer particle distribution in a hydropower canal in New Zealand.	110
Figure C.1: A figure showing all of the selected transects will appear. Check how well the selected transects correspond, and if there are any outliers. If there are outliers, then reselect the transects to be used for the final average output cross section.	132
Figure C.2: Reselected transects without outliers (i.e. without Index 4 and 6). The average cross section is now ready for export.	133
Figure D.1: ADCP benthic lander with Nortek Signature and Nortek Aquadopp.	135
Figure D.2: Stereoscopic camera chassis top (left) and bottom (right).	135
Figure D.3: Stereoscopic camera full assembly with mounting brackets and GPS antenna booms.	136
Figure D.4: Stereoscopic camera frame, zoomed oblique view.	136
Figure D.5: The CAD files provided also contain mounting brackets for GPS antennas (left), mounting brackets for the tracer particle distribution system (centre) and various saddle clamps (right). Most of these components are well suited to 3D printing with a Markforged X7 machine, with layers of continuous carbon fibre used where high rigidity is needed.	136
Figure D.6: Tracer particle distribution system, oblique view (left), top down view (right).	137
Figure E.1: Example of the camera and flight parameter calculator with constants, variables, and outputs.	138

## Tables

Table 2-1: Hyperspectral camera specifications (as of April 2022).	30
Table 4-1: Examples of LiDAR systems for remote sensing river bathymetry (as of June, 2022).	98
Table 4-2: Estimating $\alpha$ based on site roughness and expected power law profile exponents (Le Coz <i>et al.</i> , 2011; Fujita, 2018), where the power law exponent is represented as 1/m or M.	103

Table 4-3: Estimating  $\alpha$  from relative depth and power law exponents using  $\alpha = 1/(M+1)$  (Smart, 2021b).  
Based on data from Hicks & Mason, (1991) covering more than 100 New Zealand rivers.

103

## 1 Introduction

### 1.1 Motivation

River monitoring is essential to assess river health, aquatic habitat, water abstraction and flood magnitude (Gluckman, 2017). Key monitoring parameters for the physical attributes of rivers are velocity, depth, and volumetric flow rate (discharge). Existing measurement techniques using boats and current meters have low spatial coverage, and struggle in shallow channels (e.g. summer low flows, braided rivers), or during large floods. This results in missing or inaccurate data at low and peak flows, and badly informed river management at key times (e.g. water harvesting during floods; flood warnings; water allocation during low flows (Booker *et al.*, 2016)). This situation is a significant challenge for effective monitoring (MFE, 2017) and management of New Zealand's rivers (Figure 1.1).

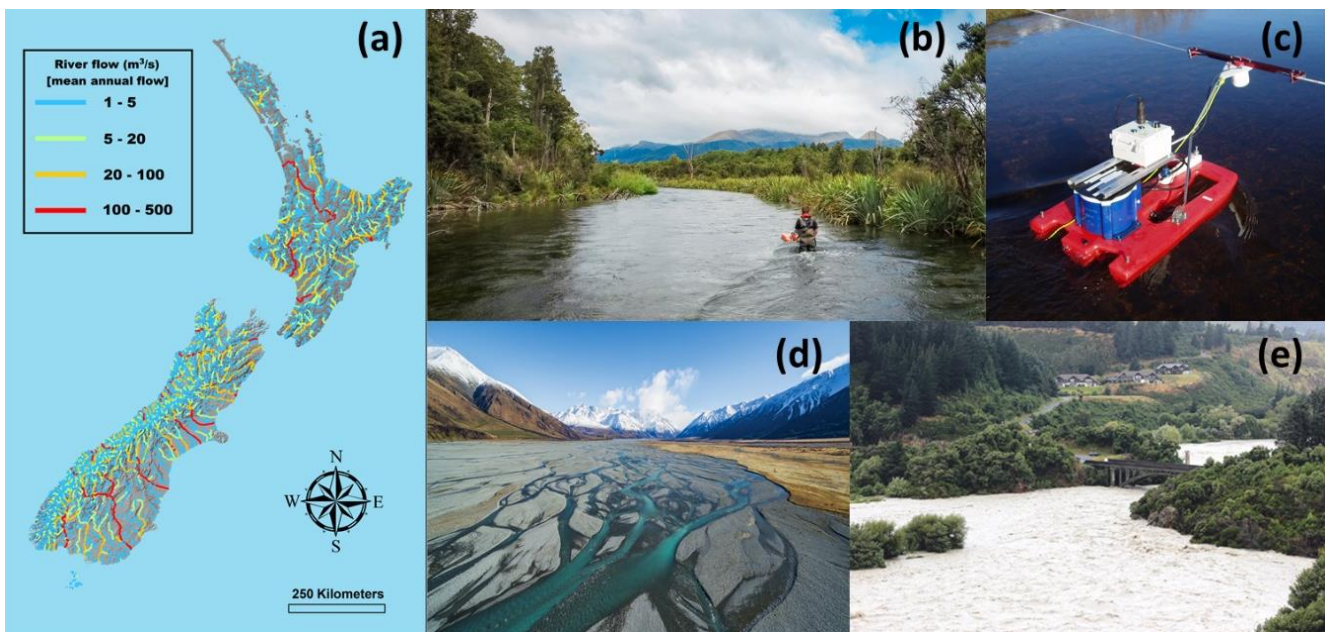


Figure 1.1: a) New Zealand rivers with mean annual flow greater than  $1 \text{ m}^3/\text{s}$ ; b) manual discharge gauging with an Acoustic Doppler Current Profiler (ADCP); c) automated discharge gauging with an ADCP; d) braided rivers are not well suited for ADCP gauging and pose safety issues for human operators crossing channels at higher discharges; e) Rakaia gorge during a flood, where ADCP gauging struggles due to high river velocity, floating debris, river depth and mobile bed materials (image Ashburton Guardian, 2013).

### 1.2 Background - Remote sensing of river flow and bathymetry

To overcome challenges with contact flow and bathymetry estimation methods, there have been a range of remote sensing methods developed, with rapid advances in this area of research over the last 10 years. A promising approach is the use of imagery to resolve surface velocities based on the movement of tracers (Le Coz *et al.*, 2010; Detert *et al.*, 2017; Detert *et al.*, 2019a). Bathymetry (depth) can then be remotely sensed using a wide range of methods (Polcyn *et al.*, 1970; Feurer *et al.*, 2008), such as: through water imagery corrected for surface refraction (Westaway *et al.*, 2001; Woodget *et al.*, 2015; Dietrich, 2017); turbulence metrics (Johnson & Cowen, 2016; Detert *et al.*, 2017; Jin & Liao, 2019); colour (i.e.

spectral attenuation and scattering of light with depth) (Polcyn *et al.*, 1970; Lyzenga, 1978; Mobley, 1994; Hicks *et al.*, 2006; Legleiter *et al.*, 2009; Jay & Guillaume, 2014; Legleiter, 2021); surface wave analysis (Polcyn *et al.*, 1970; Dolcetti *et al.*, 2022); Ground Penetrating Radar (GPR) (Annan & Davis, 1977; Spicer *et al.*, 1997; Costa *et al.*, 2000; Melcher *et al.*, 2002; Hong *et al.*, 2017); and bathymetric LiDAR (Mandlburger *et al.*, 2020; Kinzel *et al.*, 2021). With conversion from surface velocity to depth averaged velocity using the index velocity method (Le Coz *et al.*, 2010; Welber *et al.*, 2016; Biggs *et al.*, 2021). Discharge is then calculated from depth and depth-averaged velocity.

Surface image velocimetry techniques enable non-contact measurement of surface velocity distributions, through the movement of artificially added tracer particles, or visible ‘natural’ features on the water surface, such as eddies, boils, or floating debris. These techniques are very useful for discharge gauging (Randall, 2021) and measurement of 2D velocity distributions (Muste *et al.*, 2008; Detert *et al.*, 2017). Imagery of surface velocities can be obtained from bank, bridge, or mast based cameras (oblique imagery) (e.g. Le Coz *et al.*, 2010) or aerial vehicles such as drones and helicopters (nadir imagery) (e.g. Detert *et al.*, 2017). Oblique imagery needs to be orthorectified before further processing, whereas nadir imagery typically does not. Both imagery types need to be stabilised if there is any camera motion. Imagery can be scaled during the orthorectification step, or scaled later based on known distances in the imagery. Rectilinear lenses should typically be used, or distortion corrections applied to imagery collected with non-rectilinear (e.g. fish-eye) lenses. Once imagery has been orthorectified, scaled and stabilised it is ready for processing to obtain surface velocities. There are a range of techniques for processing imagery, such as: Particle Image Velocimetry (PIV)<sup>1</sup> (Creutin *et al.*, 2003; Raffel *et al.*, 2007; Muste *et al.*, 2008; Detert *et al.*, 2017); Space Time Image Velocimetry (STIV) (Fujita *et al.*, 2019); Particle Tracking Velocimetry (PTV) (Patalano *et al.*, 2017); or Feature Matching Velocimetry (FMV) (Cao *et al.*, 2020). The selection of an appropriate technique for processing imagery will depend on the density of tracers in the imagery (Manfreda *et al.*, 2019; Detert, 2020) and what the data is needed for (e.g. 2D distributions of surface velocity (LSPIV, PTV), or velocity orthogonal to a search line for discharge gauging (STIV)). There are a range of excellent software packages available for orthorectifying, stabilising and processing imagery to obtain surface velocities, for example: Fudaal-SPIV, Hydro-STIV, RIVeR, and RIVeR-STIV. Alternatively, custom algorithms can be developed, with MATLAB providing a convenient programming environment (Detert *et al.*, 2017).

### 1.3 Limitations of existing methods

The accuracy of surface velocimetry is dependent on multiple factors, such as: correct orthorectification of aerial imagery (Detert, 2020; Le Coz *et al.*, 2021); sufficient flow tracers (Manfreda *et al.*, 2019; Detert, 2020); surface wind (Hauet *et al.*, 2018; Peña-Haro *et al.*, 2020); capillary-gravity wave effects (Benetazzo *et al.*, 2017); and sources of environmental noise such as sunlight reflections off the water surface, moving shadows, or dappled sunlight on the river bed (Detert, 2020). Some of these environmental factors can be minimised by deployment in ideal conditions, for example flood measurements with plenty of natural tracer particles (Le Coz *et al.*, 2010; Al-Mamari *et al.*, 2019), deployment without wind, and deployment during overcast conditions with flat lighting. However, limiting deployments to ideal conditions greatly reduces the operational conditions in which surface velocimetry techniques can be used. Tracer particles (seeding) can be manually added to flows upstream of measurement locations (Detert, 2017), however this generally limits deployment locations to those with an upstream bridge, cableway, or narrow channels where tracers can be added from the banks. There are also other limitations of existing methods, such as: the need for static regions to be visible in aerial imagery for stabilisation and scaling (e.g. Detert *et al.*, 2017); measurement equipment (notably drones)

<sup>1</sup> When PIV is applied at large spatial scales it is typically referred to as Large Scale Particle Image Velocimetry (LSPIV)

that are limited to dry weather operations (limiting flood gauging deployments); and the requirement for ground control points to be used for orthorectification of oblique imagery.

There are also limitations of existing techniques for remote sensing bathymetry, such as:

- Bathymetry from through water imagery corrected for surface refraction requires clear/low turbidity water, limiting maximum depths that can be resolved, or deployment in flood conditions (Kasvi *et al.*, 2019).
- Bathymetry from colour and spectral attenuation is limited by:
  - Water turbidity for the maximum depth that can be achieved (Legleiter & Fosness, 2019).
  - Reflections off the water surface (such as those from specular reflection or cloud cover).
  - Shadows (Kasvi *et al.*, 2019).
  - Heterogenous bed substrate with difference reflectance characteristics.
  - Potentially time consuming site specific calibrations to depth. It is not yet clear how well calibrations translate to other surveys (at different times, or locations) with different water and substrate characteristics.
  - Surveys requiring hyperspectral data are also more expensive, challenging to process, and data intensive.
  - Likely consistent lighting conditions and normalised imagery are also very important. For example, imagery converted to reflectance through the use of calibration tarpaulins and downwelling irradiance sensors to remove changes in illumination due to changes in cloud cover, atmospheric conditions, and solar irradiance (as a function of time of day).
  - Likely also the angle that the sun intersects the water surface, which determines path length through the water and thus scattering and attenuation. Likely this limits the duration of surveys (and thus spatial coverage) that can be achieved for a specific training dataset.
- Bathymetry from LiDAR (Mandlburger *et al.*, 2020; Kinzel *et al.*, 2021) is currently limited by the cost of bathymetric LiDAR systems, turbidity (i.e. achievable depth), and likely water surface geometry/structure for complex wave fields.
- Bathymetry from turbulence metrics is limited by the high volumes of tracer particles needed to resolve time series of surface velocity fields, from which turbulent structures can be extracted (Johnson & Cowen, 2016; Detert *et al.*, 2017; Jin & Liao, 2019). While feasible for lab studies and one off field measurements, these methods are unlikely to be practical for routine bathymetry measurement, nor sufficiently accurate.

While all of these techniques are promising, they all have limitations, or are suitable for specific measurement conditions and not others. Further development of these techniques (and equipment) is an exciting area of research that is ongoing.

## 1.4 Drone flow approach

The aim of the ‘drone flow’ project was to contribute to advancing the measurement of surface velocities, depth, and discharge from the air. This was achieved by addressing some of the key knowledge gaps and limitations of existing methods. Notable contributions are:

- The development of an aerial tracer particle distribution system for seeding flows lacking natural tracers (Biggs *et al.*, 2022a).
- The development of techniques for colouring tracer particles and thresholding RGB aerial imagery to separate tracers from environmental noise due to sunglint, surface waves, and dappled light on the stream bed (Biggs *et al.*, 2022a).

- The development of a stereoscopic camera system for water surface geometry reconstruction and surface velocimetry from oblique imagery without requiring GCPs for orthorectification.
- The development of improved rainproof drones for discharge gauging in the rain by collaborators Aeronavics LTD (Skyjib model).
- Improved relationships between surface velocity and depth averaged velocity (Smart & Biggs, 2020; Smart, 2021a, 2021b).
- A comprehensive field guide on methods for measuring and estimating alpha (Biggs *et al.*, 2021).
- Novel rolling eddy model of boundary layer turbulence, that yields a log law velocity profile and explanation for von Karman's constant (Smart, 2022).
- Progress on automated grain size analysis that incorporates 3D spatial data (Detert *et al.*, 2019b).
- Contributions to the Australian National Industry Guidelines for hydrometric monitoring – Part 11: Application of surface velocity methods for velocity and open channel discharge measurements (Randall, 2021).
- Dissemination of ‘drone flow’ developments and results by the project lead and team members (18x conference talks and seminars, 1x project workshop).
- Dissemination of the potential of ‘Drones in hydraulics’ to wider audiences (e.g. Biggs, 2019).
- Bathymetry extraction from moving boat ADCP gaugings.
- Bathymetry from underwater camera imagery with underwater GCPs.
- Software toolbox from the ‘drone flow’ project released on GitHub.
- Contribution to the improvement of the software Hydro-STIV with collaborators at Hydro Technology Institute in Japan.
- Bathymetry from aerial Ground Penetrating Radar (GPR) for cross sections during floods. [Ongoing]
- Bathymetry from surface wave fields. [Ongoing]
- Raindrop splash points and texture as tracers for surface velocimetry. [Ongoing]
- The effect of wind on velocity profiles, tracer particle motion, and conversions from surface velocity to depth averaged velocity (alpha). [Ongoing]
- Stereoscopic flow gauging stations (oblique imagery) without GCPs. [Ongoing]

During the project existing methods for bathymetry estimation were also investigated and their practicality for routine monitoring and flow gauging assessed. These methods are summarised in this user guide, with references provided for further information. However, it should be noted that this field of research is rapidly evolving, and there have been significant advances in some of these areas during the 3 year period of the ‘drone flow’ project.

The original concept of the ‘drone flow’ project was that an upstream drone would release biodegradable tracer particles, while a downstream drone imaged their motion with a stereoscopic camera (Figure 1.2). This objective was achieved with the development of a tracer particle distribution system that releases biodegradable wood shavings and can carry a payload of 3 kg (Figure 1.3 and Figure 1.4). This system enables surface velocities to be evaluated in rivers and channels lacking natural tracers. A stereoscopic camera system was also developed (Figure 1.3 and Figure 1.5) that can be used for surface image velocimetry from drones (nadir imagery) or from riverbanks (oblique imagery). It can also be used for resolving water surface geometry (wave fields) if sufficient tracer particles are present. However, the stereoscopic camera system also has downsides compared to traditional RGB cameras, such as increased weight, increased complexity, lack of gimbal mounting, and decreased pixel resolution. As such it can be considered to be a specialised piece of equipment, and for most surface velocimetry tasks light weight combined camera/gimbal modules such as the DJI Zenmuse X5S, or DJI Phantom 4 Pro camera are more

suitable. The following section (Section 1.5) provides an overview of the contents and structure of the user guide.

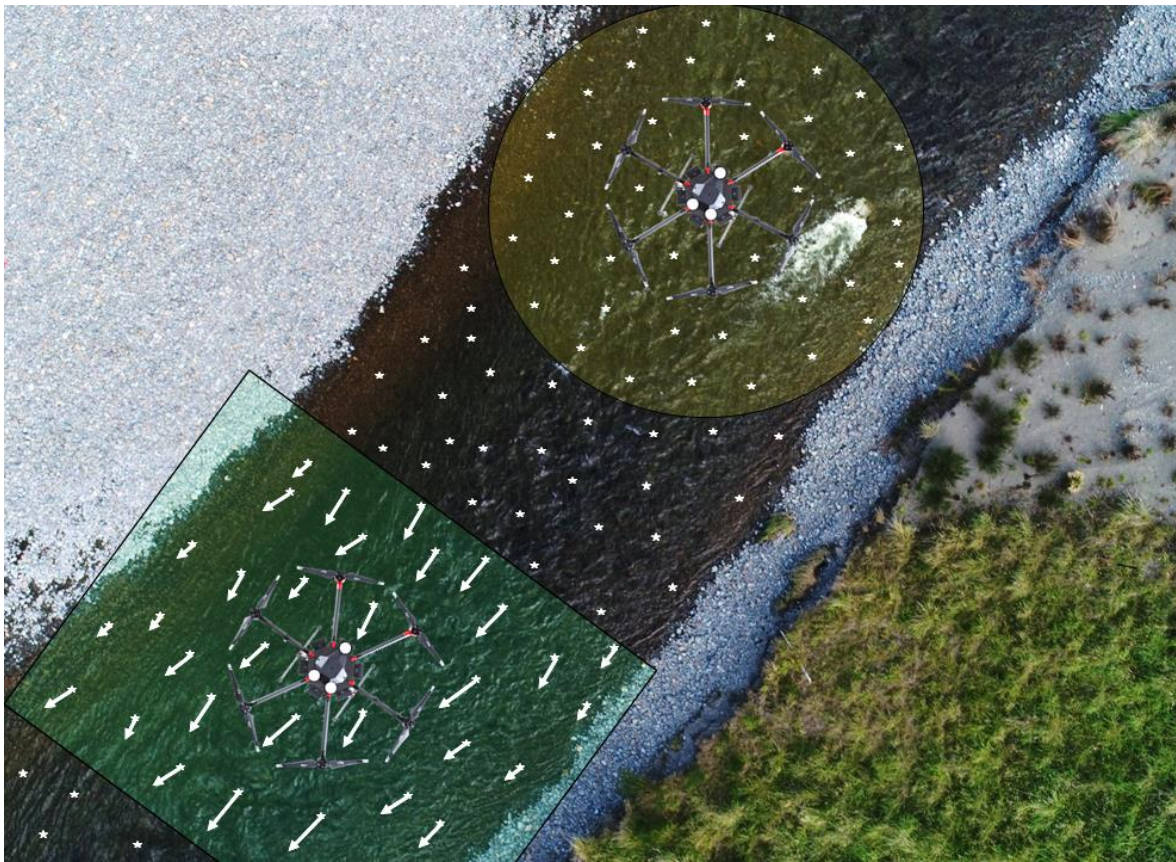


Figure 1.2: Drone formation flying where the upstream drone (yellow circle) scatters biodegradable tracer particles which are recorded by the downstream drone to resolve surface velocity fields.



Figure 1.3: Stereoscopic camera and tracer particle distribution system on 2x DJI M600 drones during a deployment in the Tekapo Canal, New Zealand.



Figure 1.4: Tracer particle distribution system in the Rangitata River, New Zealand.



Figure 1.5: Stereoscopic camera system during deployment in the Tekapo Canal, New Zealand.

## 1.5 User guide contents

This user guide provides a wide range of information, covering the equipment and software developed (and applied) during this project, methods for data collection and processing, and links to supplementary

resources such as CAD files and firmware for people seeking to develop similar systems. The user guide is divided into the following sections: Introduction (Section 1); Drone flow hardware (Section 2), which summarises the hardware developed and deployed during this project; Mission planning (Section 3); Drone flow measurement methods (Section 4), which summarises how to use the hardware to perform different measurement tasks; Summary of general advice for improving surface image velocimetry measurements (Section 5); Conclusions (Section 6); Future recommendations (Section 7); and a glossary. The user guide also includes appendices covering: Drone flow toolbox functions released through GitHub (Appendix A); Stereoscopic camera acquisition software and config settings for BFS-U3-51S5C-C cameras (Appendix B); Cross sections from moving boat ADCP gaugings (Appendix C); CAD files of ‘drone flow’ hardware (Appendix D); and a ‘Camera and flight parameter calculator’ (Appendix E).

It is hoped that the open source release of this information will accelerate the progress of other researchers in New Zealand and internationally seeking to undertake similar or related projects. Through work with stakeholders in New Zealand (such as collaborators at councils) many of the key knowledge gaps and challenges that they are facing around practical implementation of surface velocimetry techniques have also been identified. Some of these knowledge gaps have now been addressed by the ‘drone flow’ project, for example: selection of ‘alpha’ for converting from surface velocity to depth averaged velocity; and extraction of cross sections from moving boat ADCP gaugings. Other requests such as techniques to measure cross sections during large floods (when instream equipment cannot be deployed, and water turbidity prevents the use of most remote sensing techniques) are being addressed with the use of aerial Ground Penetrating Radar (GPR) and work is ongoing. Likewise, work is ongoing to investigate relationships between wind, surface velocities, and depth averaged velocities, including how wind may bias surface velocity measurements if not properly accounted for.

## 2 Drone flow hardware

### 2.1 Cameras

#### 2.1.1 RGB camera/gimbal modules

##### RGB camera selection for aerial imagery:

Red Green Blue (RGB) cameras are the standard digital cameras used for photography. They are affordable and easy to use, however not all RGB cameras are suitable (and convenient) to use for surface velocimetry and aerial surveying.

- Imagery (photos and videos) should be well illuminated, crisp (not blurry) and have constant zoom (prime lens is preferable but fixing a zoom lens at a specific setting is also a viable option).
- Cameras should be mounted in a gimbal to maintain a vertical orientation.
- Ideal cameras will have a large sensor, high quality rectilinear prime lens, and the ability to operate with wide aperture (for low lighting conditions).
- It is also critical that camera settings such as shutter speed can be controlled to avoid image blur (which will occur at slow shutter speeds).
- Cameras should record videos at a stable frame rate to maintain consistent time spacing between frames.
- Cameras and gimbals should ideally be light weight to maximise flight times.
- The use of action cameras, which often have fish-eye lenses and limited control of image settings, are not recommended.

Light weight integrated camera/gimbal modules (Figure 2.1) are the most convenient for aerial surveying, and offer many advantages over high end digital cameras (even if they have much larger 100+ Megapixel (MP) sensors). The problem with large, high-resolution digital cameras is their weight (plus the weight of a suitably large gimbal for them), which increases the size of the drone needed to carry them, decreases flight times (and thus spatial coverage) for each battery set, and increases overall mission complexity. Thus, simple integrated aerial surveying cameras such as the DJI Phantom 4 Pro Camera and DJI X5S are recommended (Figure 2.1). For nadir aerial imagery (i.e. pointing straight down) the use of polarising filters for recording through water imagery is not recommended, as it mainly reduces brightness, requiring longer shutter times, and increasing motion blur (Biggs, 2020). The cost of a DJI Phantom 4 Pro drone and integrated RGB camera/gimbal module is less than \$3,000 NZD.

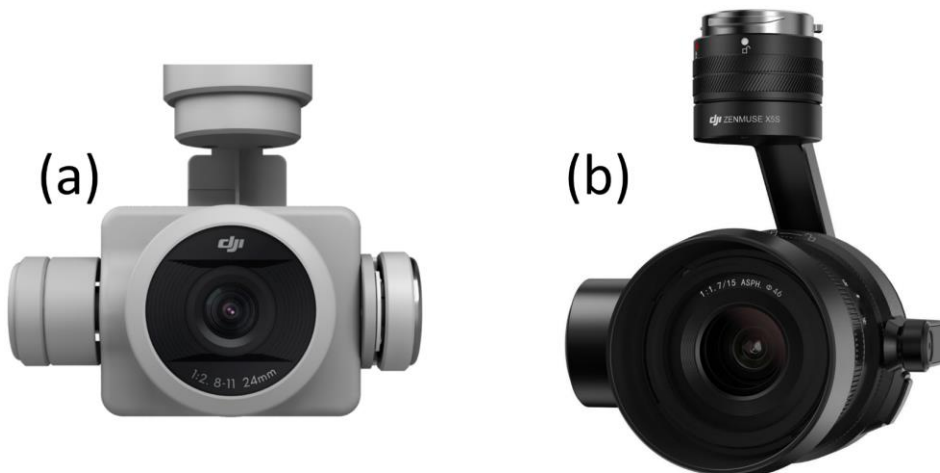


Figure 2.1: (a) DJI Phantom 4 Pro RGB Camera, (b) DJI Zenmuse X5S RGB Camera.

Integrated camera and gimbal packages are usually only compatible with a specific brand of drone (e.g. DJI cameras and drones). For other drone manufacturers it may be necessary to use other camera and gimbal combinations. We also use a Sony A5100 with a Voigtlander 15 mm lens on an X-Cam A22-2H 2-axis gimbal on a range of other drones (such as the Aeronavics Skyjib). We usually operate this camera in timelapse mode for aerial surveys, with flight parameters (such as aircraft speed, flight line spacing etc) calculated with the ‘Camera and flight parameter calculator’ (Appendix E) based on desired image overlap and altitude. For surface velocimetry with this camera, we usually start the video recording before takeoff, then trim the video after the flight. We have developed external triggers for this camera from the drone and RC unit, however the added complexity does not usually justify using them (compared to running the camera independently). The quality of the imagery from the Sony A5100 and the Voigtlander lens is slightly better (sharper) than the integrated camera/gimbal modules, however the added weight and complexity does not usually justify its use over the combined camera gimbal modules.



Figure 2.2: Sony A5100 with Voigtlander 15 mm lens on Aeronavics Skyjib, with X-Cam A22-2H 2-axis gimbal. Showing the front of the aircraft (a), and the left side of the aircraft (b).

#### RGB camera setup for aerial surveying:

To collect quality aerial imagery, it is critical to fly with suitable camera settings (Biggs, 2020). Failure to do this can result in motion blur, over/under exposed imagery, and out of focus imagery. The recommended camera settings are:

- Shutter priority mode with 1/1000 shutter (or 1/1600 in bright lighting conditions).
- Focus: auto, or manual infinity.
- Aperture: auto.
- ISO: auto.

Fast shutter speeds are the most critical parameter to avoid blurry imagery. Setting aperture to auto will allow the camera control software to adjust aperture to maintain sufficient sensor illumination (incoming light) as ambient lighting conditions change (e.g. time of day, variable cloud cover etc). If the widest aperture setting is reached (i.e. in very low light conditions), the camera starts to increase ISO to compensate. For drone surveys (usually above 30 m) wide aperture does not result in depth of field issues (the river is approximately a 2D surface) and auto focus (or manual focus at infinity) is suitable. Camera settings are usually set in software such as DJI Go 4 (for integrated DJI camera/gimbal modules) or set on the camera itself (for independent cameras such as the Sony A5100), before flights commence. Flight speeds, altitudes, imagery overlap, and other relevant settings are discussed in Section 3.5 which covers Flight planning.

### RGB camera setup for surface velocimetry:

For surface velocimetry, cameras should usually record videos at the maximum resolution that they are capable of (for example 4K) to maximise pixel resolution. The DJI Phantom 4 Pro is an excellent choice for practical surface velocimetry, as it is capable of shooting 4K video (i.e.  $3840 \times 2160$  pixels) at 60 Frames Per Second (FPS). Usually 60 FPS is an unnecessarily high frame rate (unless the flow is very fast and particle displacements are large) and 25 or 30 FPS is sufficient. The slight downside of commercially available cameras recording in video mode, is that they can be susceptible to rolling shutter, and imprecise spacing between frames. However, in practice if the water surface is well illuminated (i.e. mid-day deployment), then shutter times are brief compared to the small displacement of tracers and rolling shutter effects are negligible. Rolling shutter is primarily apparent for very fast-moving objects such as aircraft/helicopter propellers and rotor blades. If using instantaneous velocity data (for example for depth from turbulence metrics) then rolling shutter and irregular frame spacing may be slightly problematic (manifesting as increased high frequency turbulence). However, for time averaged velocity fields, these small discrepancies should average out to a stable mean velocity. For high precision PIV applications global shutter cameras with precise triggering times and raw image sequences (i.e. no video compression) are preferable, however these systems have significantly increased complexity, usually decreased resolution (due to global shutter sensors), and usually decreased frame rate (due to the higher data transfer and storage required without compression). During flights, video recording is usually commenced on the RC unit, or phone/tablet device for integrated cameras (i.e. DJI Phantom 4 Pro), or videos are started in advance for independent cameras. Video duration, altitude, and camera angle are discussed in Section 3.5 which covers flight planning.

#### **2.1.2 RGB stereoscopic camera**

The ‘drone flow’ project developed a RGB stereoscopic camera (Figure 2.3) for surface image velocimetry and 3D scene reconstruction. The camera can be mounted on a drone for nadir aerial imagery (Figure 1.3), or a tripod from riverbanks for oblique imagery.

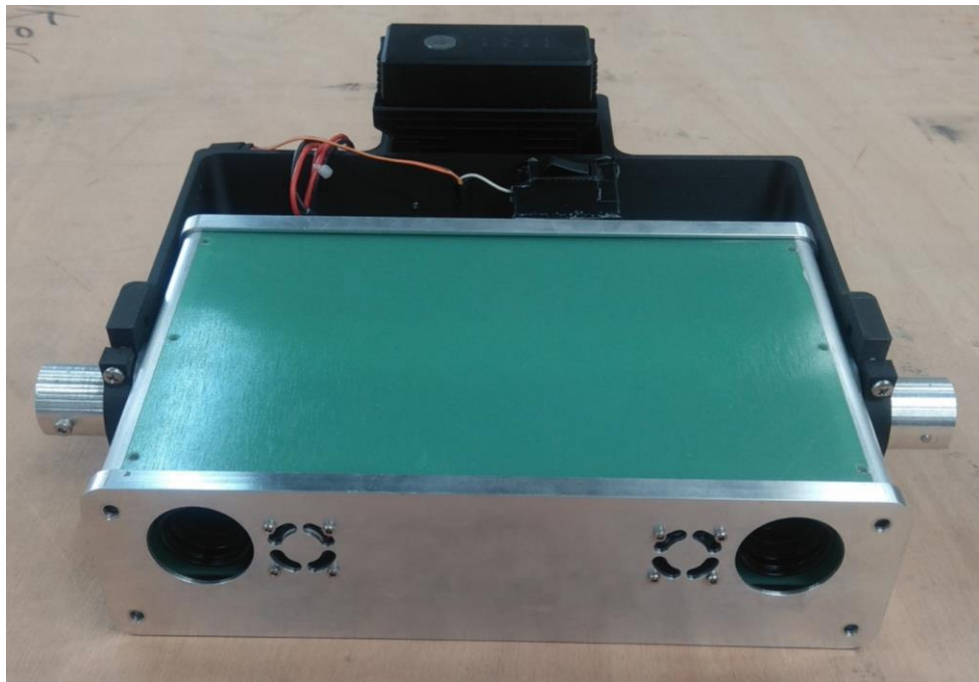


Figure 2.3: Stereoscopic camera system, with aluminium chassis, fibreglass top and side panels, and 3D printed mounting bracket.

### Stereoscopic camera hardware:

The stereoscopic camera consists of:

- 2x BFS-U3-51S5C-C global shutter RGB cameras from PTGrey/FLIR, with resolution of 2448 × 2048 pixels, maximum frame rate of 75 FPS (in mono), USB3.1 interface, and weight 36 g.
- 2x wide angle lenses for low altitude or low-resolution applications:
  - Fujinon HF1218-12M, 12 mm EFL, F1.8-22, TV distortion 0.18%, and weight 85g.
- 2x narrow angle lenses for high altitude or high-resolution applications:
  - Fujinon HF3520-12M, 35 mm EFL, F2.0-22, TV distortion 0.01%, and weight 85 g.
- Intel NUC i7-8650U, 16 GB RAM, 1 TB Samsung SSD (PCIe for high data transfer rates), 4x USB3.1 ports, and weight 500 g (including case).
- Septentrio AsteRx-i S (UAS), miniature RTK/PPK GPS and IMU, with weight <70 g.
- DJI TB47S Intelligent Flight Battery (LiPo 6S with nominal voltage of 22.2 V) and battery mounting backpack (weight 633 g).
- Power regulation board.
- External timing PCB for synchronous camera triggering and consistent frame interval.
- Machined aluminium chassis, with fiberglass plates for the top, bottom and centre panels.
  - The chassis needed to be as stiff as possible to maintain relative camera orientation and offset, but light enough for aerial deployment.
- 3D printed mounting bracket (from Onyx material with layers of continuous carbon fibre), printed on a Markforged X7 3D printer (see Section 2.5.6 and Appendix D).
- DJI dove tail quick release compatible with DJI M600 Pro drone (sourced from Lidar USA).
- Manual camera trigger (for commencing recording at the start of a flight, or on a tripod).
- PWM camera trigger (for commencing recording mid-flight using a switch on the RC unit).
- GPS extension booms and antennas (weight ~600 g).
- 2x fans to keep the system cool.

Most machine vision and PIV applications use mono (single channel) rather than RGB (3 channel) cameras, since mono camera can achieve a 3x higher frame rate for the same bit rate. However, these applications usually have consistent scene illumination, and separation of tracers occurs from brightness (for example PIV with tracer particle illumination by a laser (Biggs *et al.*, 2019)). For field applications with 3D scene reconstruction and to separate coloured tracer particles from environmental noise through colour (rather than brightness) we elected to use RGB cameras. These cameras and lenses are also very light weight, enabling them to be integrated into a stereoscopic camera suitable for deployment on a drone. The total weight of the camera, housing, battery, mounting bracket, quick release, GPS antennas and extension booms is 3888 g, making it a suitable payload for heavy lift drones such as the DJI Matrice 600 Pro, or Aeronavics Skyjib (with an associated DJI mounting bracket sourced from Small Rig Ltd). If GPS data are not required, then the GPS extension booms and antennas can be removed, saving ~ 600 g and increasing flight times. The stereoscopic camera could not be mounted in a gimbal due to its size, weight, and GPS booms. Therefore, the drone was usually hovered with the stereoscopic camera in a nadir orientation, with image stabilisation either from tracking static reference points within the FoV, or from the IMU and GPS data. When the stereoscopic camera was mounted in a tripod on the channel banks (oblique imagery) stabilisation was generally not needed (unless conditions were very windy). The top components of the stereoscopic camera are shown in Figure 2.4 and the bottom components are shown in Figure 2.5.

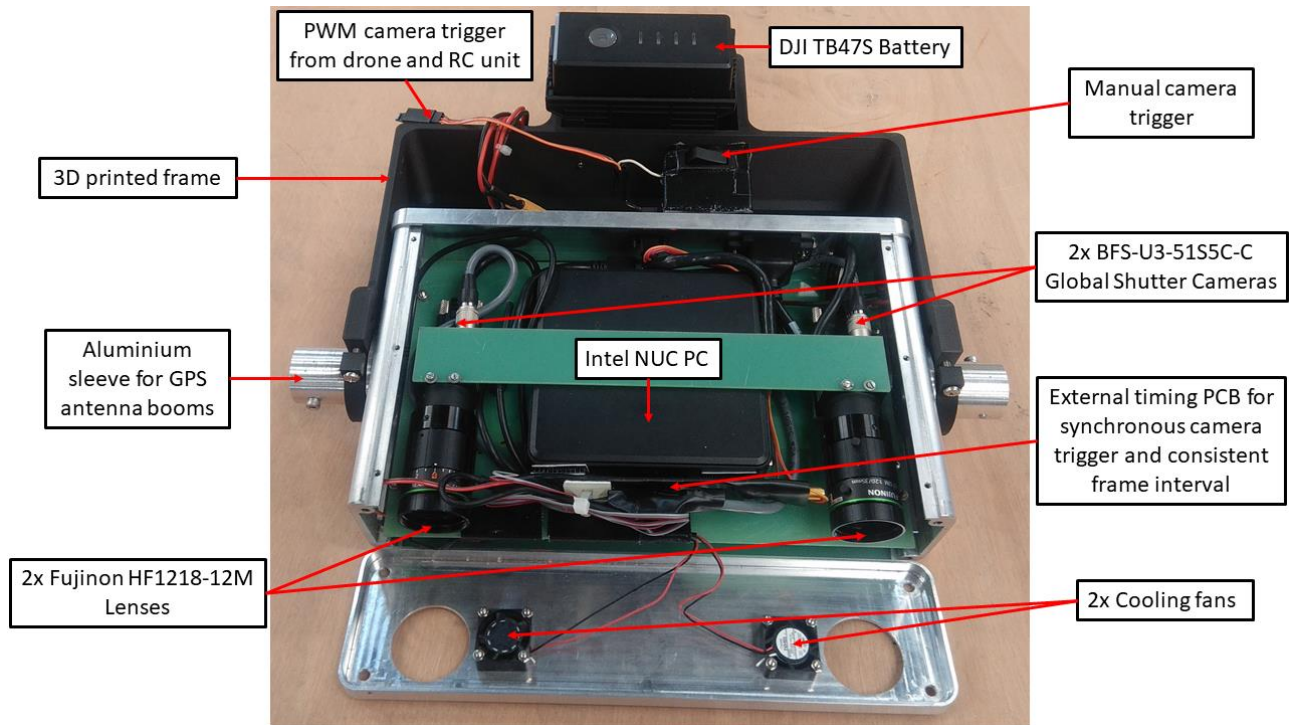


Figure 2.4: Stereoscopic camera system with top plate and front face removed to show the top layer of internal components.

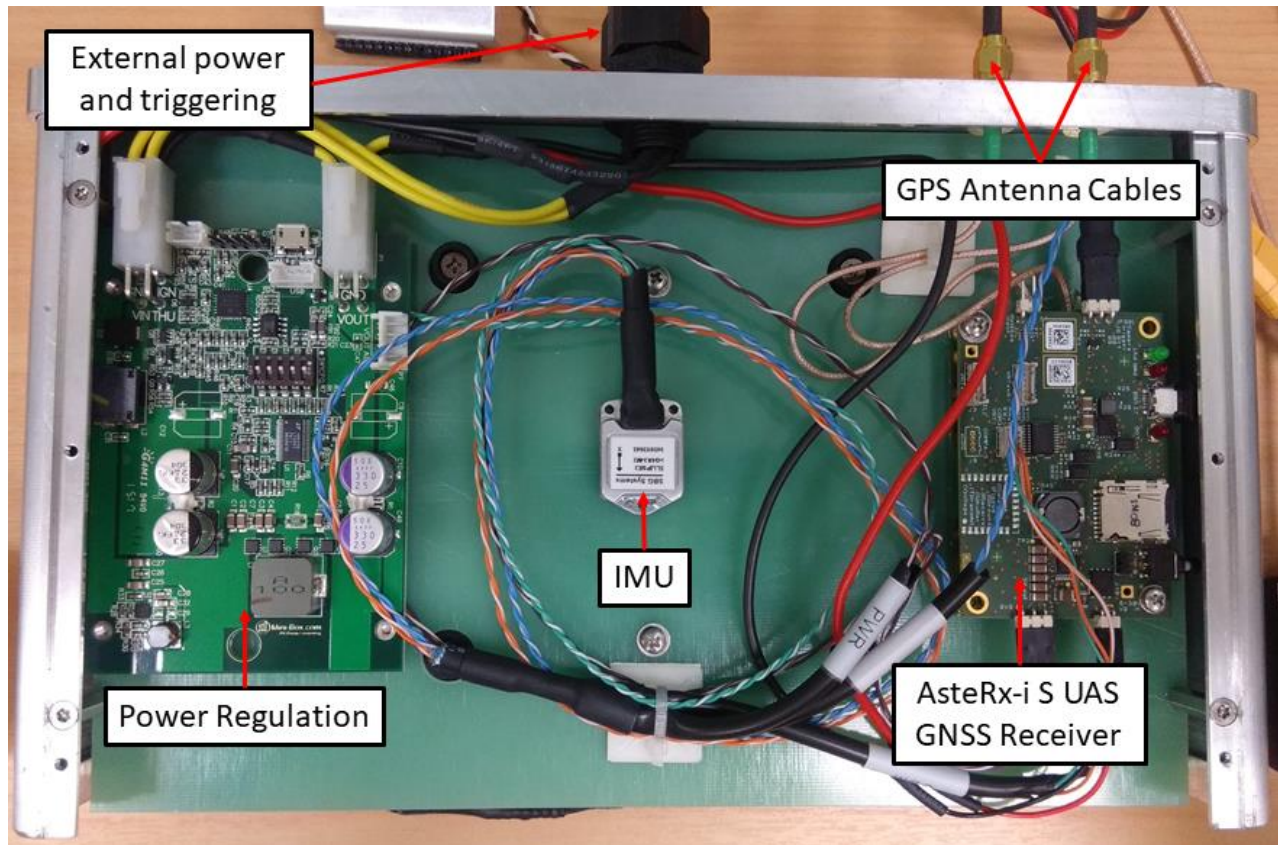


Figure 2.5: Stereoscopic camera system with bottom plate and front face removed to show the bottom layer of internal components.

### Triggering image acquisition:

To trigger the stereoscopic camera on a DJI Matrice 600 Pro drone, a switch on the RC unit was used (Figure 2.6: Left). This switch was situated on a channel expansion kit for the RC unit, with the switch setup as a PWM output in DJI Assistant 2 for Matrice, and set to 400 Hz frequency with 2500  $\mu$ s on time, which essentially corresponds to a ‘high’ signal. The PWM cable to the stereoscopic camera was connected to the PWM outputs from the A3 flight controller on the drone (Figure 2.6: Left). The PWM output from the drone was diode-OR connected with the manual switch on the stereoscopic camera so that either would work for triggering image recording. Overall, the triggering system worked well, and provided the best of both worlds for convenient manual triggering on the ground (oblique imagery and calibrations) and automatic triggering during flights (nadir imagery).



Figure 2.6: Left: DJI M600 remote controller with channel expansion kit, used for triggering image recording by the stereoscopic camera; Right: PWM outputs from the A3 flight controller.

### Camera acquisition and control software:

Development of the camera acquisition and control software was non-trivial<sup>2</sup>, and it is provided in Appendix B to accelerate any similar developments by other researchers. It also took some time to test the camera, and adjust this software to include all of the required settings needed to provide suitable exposure and colour balances for our field applications, which are more challenging than PIV in laboratories with consistent illumination. The variable settings available in the acquisition software are adjusted in a text file, with an example of suitable settings and their descriptions provided in Appendix B. The stereoscopic camera can either record RAW images, or JPG images. RAW images are sharper, since they do not use any compression, however they are larger files and take up more space on the SSD. JPG images are compressed (so they are less sharp) but take up less space on the SSD, however there is a time penalty with how long the CPU takes to perform image compression. This limits the continuous acquisition rate of JPG images to ~1 Hz. JPG images can be recorded at the same frequency as RAW images for short durations in ‘burst mode’ using the buffers of the cameras, however they cannot be recorded continuously at these frequencies. RAW images are stored as 24 BPP (Bytes Per Pixel) in interleaved RGB colour order. RAW images are opened directly in MATLAB, or converted to JPG images using the Irfan View batch processor for quick visualisation (or processing with other software). At maximum resolution of 2448  $\times$  2048 pixels, and 3 colour channels, RAW images are 15.04 MB each (in decimal representation<sup>3</sup>). The maximum frame rates that could be achieved with the stereoscopic

<sup>2</sup> Credit due to ‘Drone flow’ team member Andrew Starr for most of the work on electronics integration and acquisition software for the stereoscopic camera system.

<sup>3</sup> <https://www.gmb.org/mb-to-bytes>

cameras were 10-12 Hz, corresponding to 300.8-361.0 MB/s of data transfer from the two cameras (with 10 Hz used to provide some overhead to ensure stability). Maximum frame rate was limited by the bandwidth of the USB3.1 bus in the Intel NUC PC, since all USB3.1 ports were sharing the same bus. Data transfer to the SSD did not provide a bandwidth limitation since it was directly connected to a PCIe slot on the motherboard. Higher frame rates could be achieved at the expense of resolution by decreasing the interrogation area, or recording in mono (Figure 2.7). The system could be improved by using separate USB3.1 busses for each camera, thus doubling the achievable frame rate. Further improvements and general discussion of the stereoscopic camera are provided at the end of this section.



Figure 2.7: Chart showing the frame rate achievable with a single BFS-U3-S1S5 camera (in mono) as a function of image resolution. Maximum quoted frame rate is 75 FPS in mono at  $2448 \times 2048$  resolution.

### Synchronisation:

Synchronisation of image pairs from the stereoscopic camera is essential for accurate PIV and feature matching. We were not able to achieve precise image synchronisation using the image acquisition software on the Intel NUC, but instead developed a small external PCB with a real time clock (Figure 2.4) that provided a synchronous camera acquisition trigger with consistent time spacing. After adding the external PCB trigger, images acquired with the left and right cameras had no lag, and it was possible to capture high speed movements such as spinning wind vane propellers, or a bird flapping its wings in mid-flight with both cameras (Figure 2.8). The use of global shutter, rather than rolling shutter cameras makes these images particularly crisp. The stereoscopic camera system could be used for a wide range of applications beyond its original design specifications, such as bird tracking and velocity evaluation in three dimensions (i.e. wind), although improvements to the acquisition frame rate would be recommended for higher speed applications.

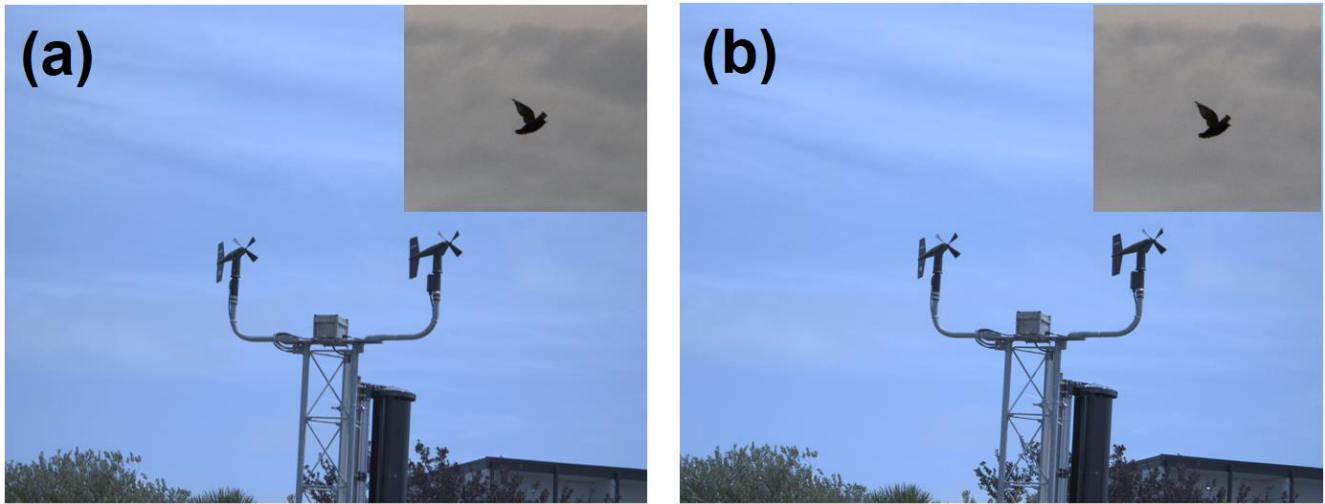


Figure 2.8: After successful synchronisation left camera (a) and right camera (b) images have no lag and can capture synchronous images of wind vane propellors spinning and bird wings flapping mid-flight.

#### Calibration:

Calibration of the stereoscopic camera system was performed for each lens pair, using an  $8 \times 7$  checkerboard target<sup>4</sup>. The development of a lightweight, but flat and durable calibration target was slightly more challenging than expected, since most backing materials deform/bend (i.e. wood, or thin metal), or are too heavy (thick metal). To resolve this issue an aluminium honeycomb panel  $25 \times 1436 \times 1490$  mm, was sourced from Paynes Aluminium Ltd. The aluminium honeycomb panel was very flat, yet light weight and stiff, due to its 25 mm thickness and construction technique. An  $8 \times 7$  checkerboard pattern was printed on canvas and glued to the aluminium honeycomb panel. The printer had excellent spatial accuracy and consistency between the  $x$  and  $y$  printing directions (very important to check), with a square size of 183.4286 mm along the  $x$  axis, and 183.3750 mm along the  $y$  axis, yielding an average square size of  $183.4018 \pm 0.0268$  mm, with the very low error between each axis direction making it a suitable target for camera calibration (Figure 2.9).



Figure 2.9: Images of  $8 \times 7$  checkerboard target with (a) left camera, and (b) right camera.

<sup>4</sup> Calibration targets should be asymmetric and  $8 \times 7$  is a common size.

During calibration image pairs were recorded at a range of distances and angles between the stereoscopic camera and checkerboard target. Image pairs were selected where the target was present in different portions of the image frames (i.e. North, West, South-East etc) to fully cover the overlapping portion of the camera field of view. Approximately 20 image pairs were used for calibration, with calibrations repeated for both pairs of lenses (i.e. 12 mm and 35 mm lenses). Stereoscopic camera calibration was performed in MATLAB using the ‘Stereo Camera Calibrator App’ which is very convenient and easy to use (Figure 2.10). Stereoscopic camera calibration can also be performed using other software such as OpenCV, which may perform better if non-rectilinear (i.e. fisheye) lenses are used<sup>5</sup>. The stereoscopic camera calibration parameters for each lens pair were then saved and reused for processing field data from the stereoscopic camera during point matching, 3D reconstruction, and orthorectification.

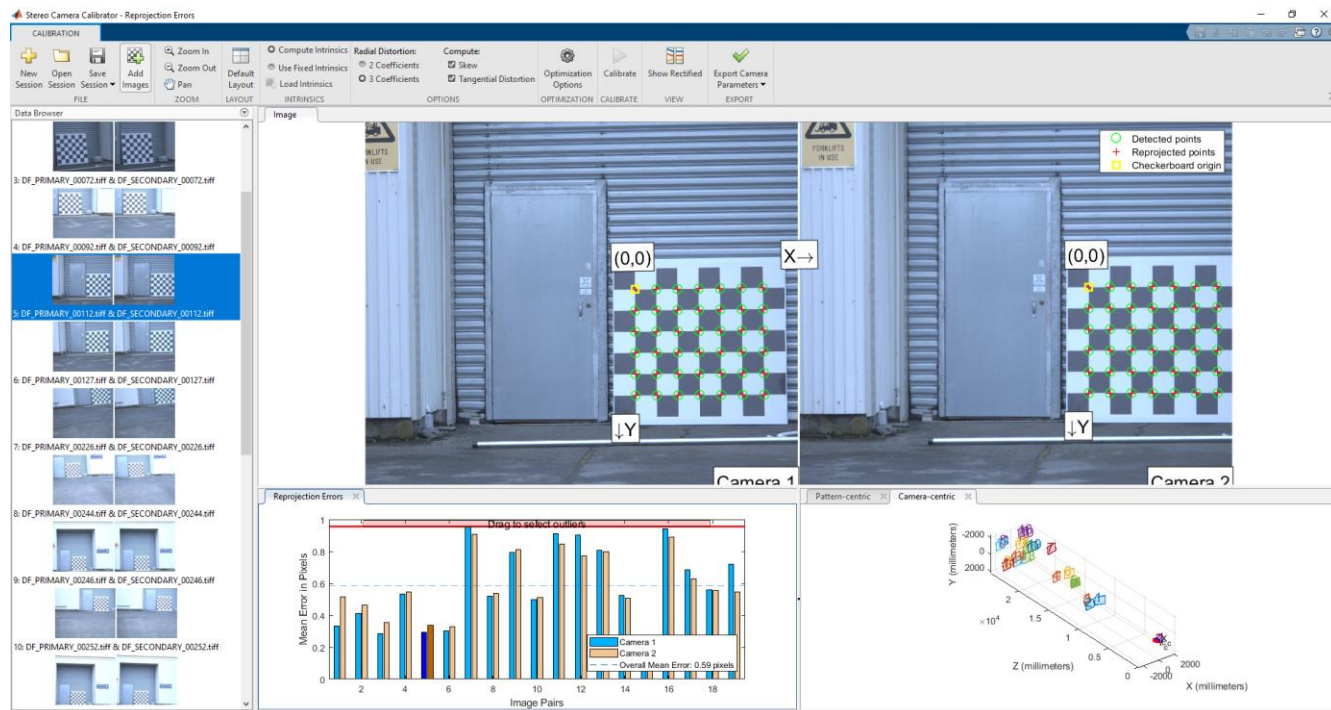


Figure 2.10: Example of stereoscopic camera calibration in MATLAB to evaluate intrinsic stereoscopic camera parameters.

### Deployment:

The stereoscopic camera has a DJI dove tail quick release allowing it to be easily attached to a DJI M600 Pro drone, a modified Aeronavics Skyjib drone, or a tripod. Before field deployment lenses are focused and locked in position, then camera acquisition parameters and settings are configured. Setup of the stereoscopic camera takes around 10 minutes in the field. After field data collection, imagery is manually checked to verify that appropriate acquisition settings were used, and that quality imagery was recorded. The stereoscopic camera has been deployed at a range of field sites around New Zealand, with deployment in nadir configuration on drones (Figure 2.11 to Figure 2.14), and oblique configuration on a tripod (Figure 2.15).

<sup>5</sup> Martin Detert, personal communication.



Figure 2.11: Stereoscopic camera deployment in the Ashley River, New Zealand.



Figure 2.12: Stereoscopic camera deployment in the Rangitata River, New Zealand.



Figure 2.13: Stereoscopic camera setup in the Tekapo Canal, New Zealand.



Figure 2.14: Stereoscopic camera deployment in the Tekapo Canal, New Zealand.



Figure 2.15: Stereoscopic camera oblique deployment on a tripod in the Rangitata River, New Zealand.

#### Recommended future upgrades:

There are multiple upgrades that would improve the performance (and practicality) of the stereoscopic camera. These are:

- Upgrade the cameras to newer models with higher resolution. For example, the Blackfly BFS-U3-244S8C-C is a 24.5 MP colour global shutter camera (vs 5.0 MP for our cameras).
  - This would provide sufficient resolution to enable the camera to also be used for aerial surveying, and to resolve smaller tracer particles.
  - There would be a frame rate penalty at higher resolution, however the image interrogation area could be reduced to run at higher frame rate (when not surveying), or the camera could be run in mono, or other ‘tricks’ (e.g. compression or buffering) could be used.
- Include a second USB 3.1 hub (for the second camera) directly connected to a PCIe slot on the Intel NUC motherboard to double the bandwidth of data collection, and thus double the achievable frame rate.
- Investigate other cameras with a larger internal memory ‘buffer’ enabling longer ‘burst mode’ data recording, before slower data transfer to the SSD through the USB3.1 hub (or hubs).
- Mechanically redesign the camera to be smaller form factor (and smaller stereoscopic baseline) enabling it to fit within standard gimbals (such as the DJI Ronin MX), providing better image stabilisation and nadir orientation (when needed).
- Write code (e.g. MATLAB stand-alone runtime app) for better visualisation (live stream) of camera images during setup (through remote desktop connection), and also automatic assessment of camera focus (e.g. quantification of blur through 2D spatial autocorrelation) to speed up camera lens focusing (and make it less subjective/manual).

While the current version of the stereoscopic camera is fit for purpose and provides a significant ‘step in the right direction’ in the field of stereoscopic surface velocimetry and remote sensing, these upgrades would provide useful improvements.

### 2.1.3 Hyperspectral camera

Hyperspectral cameras (scanners) record aerial imagery in hundreds of narrow spectral bands. This is vastly different from the three broad spectral bands of RGB cameras (which usually have an overlapping spectral response), or the limited number of spectral bands (usually between 4 and 10) offered by multispectral cameras. However, hyperspectral cameras have a very different architecture from RGB or multispectral cameras. Hyperspectral cameras typically record a single line of pixels and must be moved through space to create a 2D image. This type of imaging system is known as a push broom scanner and contrasts with RGB and multispectral cameras which collect a 2D image for every frame. The advantage of the hyperspectral camera system is high spectral sensitivity, providing data well suited for automatic classification of objects based on differences in reflectance at different wavelengths of light.

There are also disadvantages of hyperspectral cameras such as increased cost (e.g. \$50-100k NZD), complexity, and the inability to capture images of moving objects (which can be achieved easily with RGB and multispectral cameras). RGB and multispectral cameras are well suited for recording overlapping 2D images along flight paths, with these images able to be processed with structure from motion software (e.g. Agisoft Metashape) to generate georeferenced orthomosaics and Digital Elevation Models (DEMs). In contrast, hyperspectral cameras need high resolution Inertial Measurement Units (IMUs) to resolve their orientation, and high-resolution GPS to determine their origin (ideally Real-Time Kinematic (RTK) or Post-Processed Kinematic (PPK) GPS).

Post processing hyperspectral imagery to generate georeferenced orthomosaics (i.e. georeferenced hypercubes) is also non-trivial. For surveys of terrain that is not flat (e.g. with hills or trees) geocorrection of imagery involves projections onto a Digital Surface Model (DSM). For this reason, it is often complementary to simultaneously fly a high resolution RGB camera and use Structure from Motion (SfM) software (e.g. Agisoft Metashape or Pix4D) to generate a DSM. It is also more challenging to remove sunglint and surface reflections from hyperspectral aerial imagery than RGB or multispectral imagery, although it is possible if overlapping flight lines are used. Flight line planning should account for the sun direction, and North-South flight lines are generally preferred to East-West flight lines (at solar noon). This is because the ‘scan line’ is orthogonal to the flight direction, so East-West flight lines will have a North-South scan line, which will likely pick up sunglint at one end of the scan line (around solar noon and over water).

When selecting a lightweight hyperspectral camera system suitable for drone operations, two of the leading systems are the Headwall Nano-Hyperspec and Resonon Pika L Airborne System (Figure 2.16). The specifications of the Headwall Nano-Hyperspec and Resonon Pika L cameras are similar (Table 2-1). The Resonon Pika L provides a slight advantage for aerial applications with 900 spatial bands rather than the 640 provided by the Headwall Nano-Hyperspec. This results in wider images and fewer flight lines. The Nano-Hyperspec is able to record scan lines at a higher maximum frame rate of 350 FPS, compared to 249 FPS for the Pika L. However, this difference is likely only advantageous in very bright conditions and for high velocity surveys (i.e. from a manned aircraft). For deployments from a drone frame rates close to 100 FPS are more common and provide sufficient exposure time (i.e. incoming light to the sensor) to minimise the gain required and thus decrease signal noise.

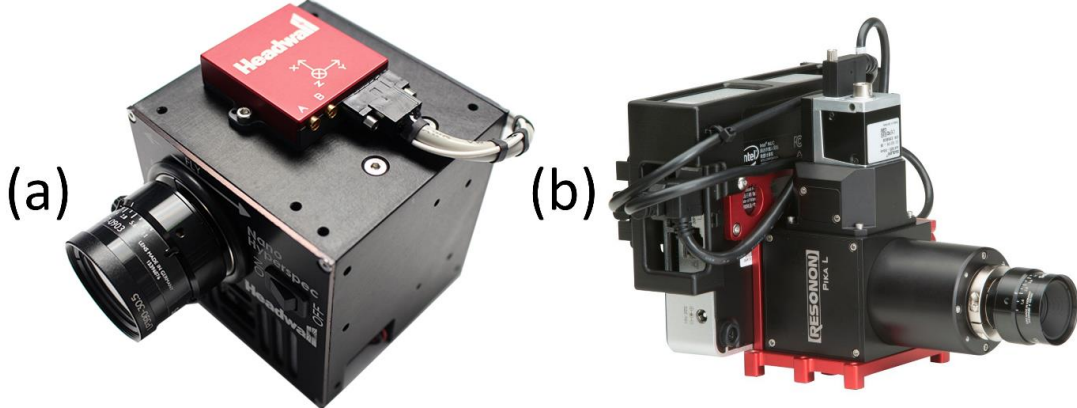


Figure 2.16: (a) Headwall Nano-Hyperspec, (b) Resonon Pika L Airborne System.

Table 2-1: Hyperspectral camera specifications (as of April 2022).

	<b>Headwall Nano-Hyperspec</b>	<b>Resonon Pika L</b>
Spectral Range (nm)	400–1000	400–1000
Spectral Channels	270	281
Spectral Resolution (nm)	2.2	2.1
Spatial Bands (i.e. Pixel Swath)	640	900
Max frame rate (FPS)	350	249
Bit Depth	12	12

Many auxiliary systems are also required to generate georectified reflectance hypercubes:

- A high resolution IMU and GPS system (e.g. the SBG Systems Ellipse3N).
- A calibration tarpaulin with a flat spectral reflectance curve and large size (e.g.  $2.4 \times 2.4$  m).
  - It is recommended to get a tarpaulin that has two different reflectance values (e.g. 12% and 24%). A tarpaulin with a single high reflectance value (e.g. 36%) can saturate the sensor when deployed on a dark background.
  - The tarpaulin supplier should provide the measured reflectance curve for the tarpaulin (as well as the approximate average reflectance) for use in conversions to reflectance.
- Georectification software (e.g. the Resonon Georectification Plugin).
- Software for postprocessing/analysis of hyperspectral imagery (e.g. Resonon Spectronon Pro).
- Ideally also a downwelling irradiance sensor to collect data on ambient lighting conditions and how they change during the deployment (e.g. due to time of day and variable cloud cover). This data can be used in conjunction with calibration tarpaulins for improved conversions to reflectance. A suitable downwelling irradiance sensor is the Ocean Optics Flame Spectrometer.

Anyone looking to purchase a hyperspectral imaging system should be aware that all systems are expensive and time consuming to commission, they are not ‘turn-key’ solutions. Significant time should be allocated to installation, set up, and training before field operation of any hyperspectral imaging system. Although we have not had experience with Headwall products and service to compare, we have found that the training and ongoing customer support from Resonon are excellent.

### Initial hyperspectral camera system setup (what not to do):

We originally setup our hyperspectral camera system rigidly attached to a DJI M600 drone, with an Ellipse 2D IMU/GNSS receiver, two GPS antennas (with large spatial separation), and a downwelling irradiance sensor (Figure 2.17). The logic behind this setup was to provide:

- Maximum spatial separation between the dual GNSS antennas to obtain highly accurate heading/yaw data.
- Reduced weight by not using a gimbal (the weight of a DJI Ronin MX gimbal is ~2.5 kg).
  - Theoretically a gimbal should not be needed, since imagery is georectified using the GPS/IMU and projected onto an underlying Digital Surface Model (DSM).
- To provide consistent lever arms between the GPS antennas, IMU, and camera (so that the camera and IMU do not move independently of the aircraft and GPS antennas).
- To have the downwelling irradiance sensor mounted on the drone near the camera for irradiance at the measurement location.

However, this setup resulted in multiple unforeseen problems:

- High frequency vibration of the entire camera system caused problematic ‘wobble’ and ‘blur’ in the recorded imagery. This vibration was higher frequency than what could be reliably picked up by the IMU and removed during georectification.
  - MATLAB code was written that could remove the lateral component of this vibration, however any front to back vibration cannot be removed and results in skipping forward and back of measurement lines.
- The orientation of the downwelling irradiance sensor changed relative to the sky/sun as the drone flew zig-zag lines over the study sites (i.e. different orientation in one flight direction vs the return flight direction), resulting in stripy hyperspectral imagery after processing to reflectance.

There were also significant problems with Electro Magnetic Interference (EMI) with the highly sensitive Ellipse 2D in dual antenna configuration resulting in GPS signals dropping out and measurements ceasing (see section below).



Figure 2.17: Initial configuration of the Resonon Pika L hyperspectral camera on a DJI M600 drone, with rigid mounting, dual antenna booms, and downwelling irradiance sensor (what not to do!).

### Electromagnetic interference (EMI) and GPS:

GNSS signal frequencies (including GPS, GLONASS, Galileo, and BeiDou)<sup>6</sup> generally fall within two bands between ~1175-1280 MHz and ~1560-1610 MHz. These signal frequencies overlap with the data transfer spectrum and EMI noise characteristics of USB3 transmission protocols (Intel, 2012). The first GPS signal frequency band (i.e. ~1175-1280 MHz) also corresponds to a harmonic of a peak in USB3 noise from external disk drives between 2.4 and 2.5 GHz (Intel, 2012). The EMI due to USB3 data transmission caused significant problems with the highly sensitive Ellipse 2D IMU and GNSS receiver from SBG Systems. The EMI caused GPS signals to drop out and recording of hyperspectral camera data to cease. To address this problem all USB3 plugs were shielded with copper tape. This helped the problem, however whenever the SSD drive was plugged into the Intel NUC computer the GPS signal dropped out immediately. This problem was remedied by placing the SSD inside a metal enclosure with an internal SATA plug, then shielding the entire SSD enclosure with copper tape. The SBG Ellipse 2D that we used is very sensitive to EMI, and apparently the Ellipse 2N or 3N model is not as bad. We have heard that new versions of the Ellipse D (3<sup>rd</sup> Generation) have better noise rejection, however in our experience the extra money to get an Ellipse D over an Ellipse N is simply not worth it.

### Recommended hyperspectral camera setup and operation:

The hyperspectral camera should be mounted on a gimbal (such as the DJI Ronin MX) and properly balanced (Figure 2.18). A single antenna GNSS receiver and IMU is recommended (e.g. the SBG Systems Ellipse 3N). All USB connections and particularly the external Solid-State Drive (SSD) should be shielded with copper tape, and the SSD ideally placed inside a metal enclosure. The downwelling irradiance sensor should be run independently from the hyperspectral camera and mounted on a tripod on the ground logging to a laptop. This ensures that the angle of the fiberoptic cable inlet relative to the sky is consistent. It also improves the balance of the gimbal and reduces the risk of damaging the fiberoptic cable when performing gimbal calibrations. The system clock on the laptop and hyperspectral camera flight computer should be synchronised (usually in UTC time zone). The downwelling spectra can then be matched to the hyperspectral data cubes during post processing using python scripts provided by Resonon Ltd.

---

<sup>6</sup> <https://novatel.com/support/known-solutions/gnss-frequencies-and-signals>

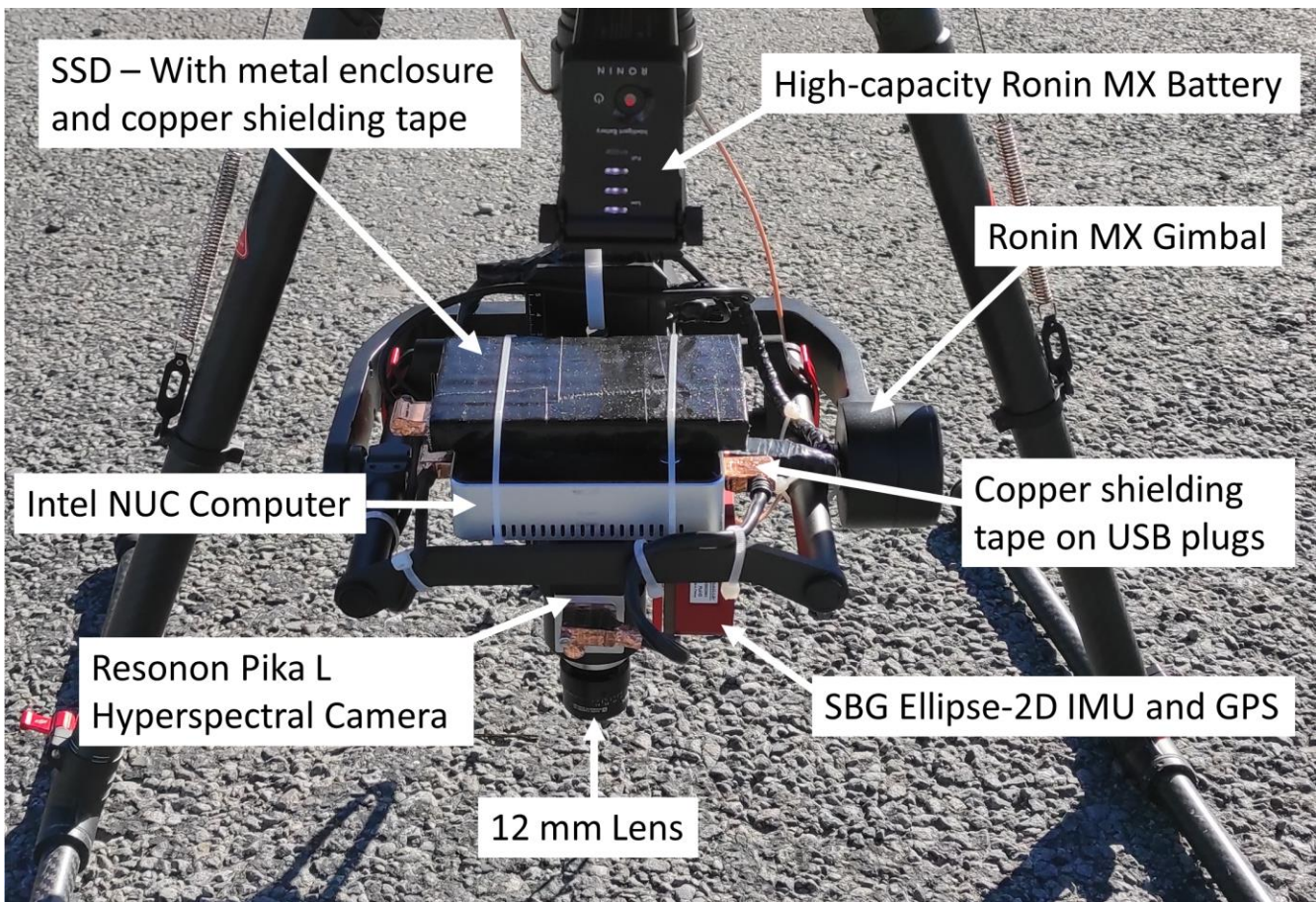


Figure 2.18: Recommended Resonon Pika L Hyperspectral Camera deployment configuration on a DJI Ronin MX Gimbal, with full shielding of the SSD and all USB3 plugs.

The calibration tarpaulin should be placed within the survey area, ideally on top of flat terrain that has similar reflectance to avoid saturation of the recorded pixels of the tarpaulin. The tarpaulin should ideally be stretched flat (i.e. between waratahs/posts with ratchet straps) and may even benefit from being ironed flat prior to deployment if it is wrinkly or creased. The user manual should be read in detail and protocols followed to set up the GNSS receiver and IMU (i.e. calibration, lever arms, etc.).

Before a flight, the area to be surveyed should be defined in Google Earth as a polygon and exported as a .kml file. This file is then uploaded to the hyperspectral camera flight computer in the Resonon Ground Station software. The Resonon Airborne Calculator can be used to determine the flight line spacing, altitude, flight speed and frame rate required to achieve square pixels with the desired dimensions and overlap. These parameters are then written to the hyperspectral camera flight computer using the Resonon Ground Station software.

Automated drone flights are planned and set up in software such as DJI Ground Station Pro to match the parameters specified by the Resonon Airborne Calculator. Flight lines should extend past the boundaries of the polygon defined in Google Earth, as a hyperspectral data cube will cease recording when the hyperspectral camera GPS location is outside of this polygon, and a new one will commence when it re-enters the polygon.

The drone and camera orientation must be aligned with the flight path (i.e. the drone rotates at the ends of each flight line to maintain ‘forward’ facing flight). This is because the hyperspectral camera is a push

broom scanner and the scan line must pass over the terrain to be imaged. The gimbal needs to be operated in a mode where it stays ‘locked’ to fly forward relative to the orientation of the mount (so it essentially becomes a 2-axis gimbal). For the DJI Ronin MX there is a switch on the gimbal RC unit to change modes. It is also possible to change gimbal response curves via Bluetooth connection in DJI Assistant for Ronin MX, to adjust how quickly the gimble returns to its defined orientation after an external rotation.

More detailed information on hyperspectral camera settings and setup can be found in the manufacturer’s user manual. It is also worthwhile to attend a training course run by the camera system manufacturer. The hyperspectral camera system setup that we recommend is shown in Figure 2.19.



Figure 2.19: Resonon Pika L hyperspectral camera during deployments in the Avon-Heathcote Estuary in New Zealand.

#### 2.1.4 Underwater cameras

Underwater cameras were used in conjunction with underwater ground control points (Section 2.4.3) to create underwater georeferenced orthomosaics and high resolution digital elevation models of river bathymetry (Section 4.7.4). Consumer grade underwater cameras such as the EKEN H9R or GoPro HERO9 (Figure 2.20) can be deployed on a long pole for manual surveying with a ring light for improved illumination of the bed (Figure 2.21). Ideally underwater cameras should be selected that have rectilinear (rather than fisheye) lenses. Overall these small cameras are effective for underwater mapping, with the main limitation being the area that can be covered, which is dependent on water depth (field of view) and the required image overlap (i.e. 80% front and 60% side) for processing with structure from motion software (e.g. Agisoft Metashape or Pix4D). The use of a ‘glass bottom boat’ where the camera is

elevated above the water surface (i.e. water-glass interface) would significantly improve the field of view for underwater imagery and shallow water bathymetric mapping (see below).



Figure 2.20: EKEN H9R (left) and GoPro HERO9 (right) underwater cameras.



Figure 2.21: Left: EKEN H9R camera and LED ring light on a survey pole to collect underwater imagery for high resolution bathymetric mapping. Right: LED ring light and EKEN H9R camera.

#### Glass bottom underwater imagery boat:

A prototype glass bottom underwater imagery boat was constructed by using an ADCP boat hull (e.g. suitable for deployment of a River Pro), then developing a waterproof glass bottom cylinder to house a Sony A5100 camera. The waterproof glass bottom camera cylinder was then fit through the centre hole ‘moon pool’ of the ADCP boat hull. While the prototype was successful as a proof of concept, there are some significant upgrades needed to construct a practical and rugged boat suitable for field deployments:

- Lighting is needed on the underside of the boat, for adequate illumination of the bed, and removal of boat shadows.
- A custom-built boat is recommended (rather than using an existing ADCP boat hull), to enable a much larger underwater viewing window. This would allow the camera to be mounted higher up, thus improving the field of view of the riverbed.
- A system that can be rapidly constructed/de-constructed is needed, with easy access to the camera for adjusting settings, and inspecting imagery.
- Risks around scratching the glass (or acrylic/polycarbonate) underwater viewing window on rocks need to be addressed. The use of thin films as protective coatings (similar to cell phone screen protectors) may address this issue.

- The incorporation of an IMU and RTK GPS at the camera origin may circumvent the need for underwater GCPs.
- It is also possible to setup RTK GPS units (such as the Trimble R10) to provide an output trigger once they have moved a certain displacement (similar to what we use with a Tritech Depth Sounder see Section 2.5.3). This would allow collection of underwater imagery with a minimum pre-defined overlap (based on boat displacement and FOV at the surface).

Overall significant development is needed to produce a functional and fit for purpose underwater imaging boat for bathymetric mapping. For the proof of concept contained within this user guide, underwater cameras on survey poles proved to be sufficient. Future work on an underwater imaging boat is recommended however, as the extremely high resolution orthomosaics, DEMs, and 3D models that can be obtained from georeferenced underwater imagery, would provide ideal inputs for applications such as underwater sediment sizing, or hydraulic modelling. Underwater imagery provides a higher resolution (but smaller spatial coverage) alternative to larger scale measurements with techniques such as through water imagery corrected for surface refraction (Section 4.7.7). It could also provide useful high-resolution reference data for validation of other techniques for remote sensing river bathymetry.

## 2.2 Drones

Multirotor aircraft are convenient for surface velocimetry, surveying, and many other river remote sensing missions. They are known by a wide range of names and acronyms, such as: Unmanned Aerial Vehicles (UAVs), Unmanned Aerial Systems (UAS), Uncrewed Aerial Vehicles (UAVs), Remotely Piloted Aircraft Systems (RPAS), or simply ‘drones’. They can take off (and land) vertically and can carry a wide range of payloads, from simple RGB cameras, to tracer particle distribution systems, or Ground Penetrating Radar (GPR). Multirotor aircraft can be flown manually, or easily programmed to fly repeatable paths. They are relatively inexpensive to purchase (generally between \$4K and \$20K NZD) and are very inexpensive to operate compared to flights with manned aircraft/helicopters. Selecting an appropriate multirotor aircraft depends on the required payload and flight time. For most RGB applications a small drone such as the DJI Phantom 4 Pro (Section 2.2.1) or the DJI Matrice 210 (Section 2.2.2) is sufficient. The use of small drones is advantageous for maximising battery life, minimising equipment complexity, and maximising operator safety. However, for more complex (and heavy) payloads, larger drones such as the DJI Matrice 600 Pro (Section 2.2.3) or Aeronavics Skyjib (Section 2.2.4) are needed. There have been no river remote sensing tasks encountered during the ‘drone flow’ project where fixed wing drones are recommended, and their many downsides far outweigh any benefits from increased flight time/coverage vs battery life. For very large surveys with multirotor aircraft, the simplest solution is to get more batteries, chargers, and a generator. We operate our Phantom 4 Pro with 8 sets of batteries, and our DJI M600 with 6 sets of batteries, then use a generator to charge depleted battery sets after each flight. With this approach, both drones can fly continuously. For very large-scale surveys (e.g. catchment scale) manned helicopters or aircraft are recommended (or satellite data for lower resolution applications).

### 2.2.1 DJI Phantom 4 Pro

During the ‘drone flow’ project a DJI Phantom 4 Pro drone (Figure 2.22) was used regularly to perform aerial surveying and surface velocimetry. This drone is very easy to use and has a high-quality integrated camera/gimbal module. For most aerial surveying and surface velocimetry work, this is the recommended drone to purchase. The camera and lens also provide consistently high-quality imagery (crisp), that is (in our experience) slightly better than that from the DJI X5S camera (surprisingly). The high-quality imagery also makes it well suited for aerial surveys of grain size distributions. The main downsides of

this drone are: (1) the small size and white colour can make it hard to distinguish against white clouds during large surveys, limiting the maximum separation between the drone and pilot while still maintaining ‘visual line of sight’; (2) the lack of any water proofing and rain resistance; (3) susceptibility to wind due to its small size and weight (care should be taken on landing, and flight paths should be planned to return downwind). However, these downsides are minimal compared to its convenience. The DJI Phantom 4 Pro is now also available with Real Time Kinematic (RTK) or Post Processed Kinematic (PPK) GPS. This may enable accurate orthomosaics and Digital Elevation Models (DEMs) to be generated without the use of Ground Control Points (GCPs) (Tomaštík *et al.*, 2019; Štroner *et al.*, 2020). This would be highly beneficial for surveying wide river sites where it is not possible to deploy GCPs within the river, and/or where dense riparian vegetation makes deployment of GCPs on riverbanks problematic. The inclusion of RTK/PPK GPS is also beneficial for accurately georeferencing surface velocimetry videos or estimating channel width. Channel width can be estimated by hovering the drone over each channel/bank edge, then taking a nadir image with the channel/bank edge in the centre of the frame, then extracting the GPS coordinates from the image EXIF data. This is particularly useful for flood gauging, enabling convenient scaling of nadir surface velocimetry imagery/videos when channel width cannot be surveyed in, or measured with other techniques. For very wide rivers or large floods, RTK GPS also enables the locations of static objects/features to be recorded (from hovering over these objects/features and capturing a nadir image with them in the centre of the image), which then enables these objects/features to be used as GCPs for orthorectification of oblique imagery (see Section 3.5). While this is not ideal compared to deployment of standard GCPs and surveying with RTK GPS, it provides a convenient alternative for short notice deployments (such as emergency flood gauging) or when deployment and surveying of standard GCPs is not practical or safe.



Figure 2.22: DJI Phantom 4 Pro drone with integrated RGB camera/gimbal module.

### 2.2.2 DJI Matrice 210

During the ‘drone flow’ project a DJI Matrice 210 drone (Figure 2.23: left) was used regularly to perform aerial surveying and surface velocimetry. This drone is easy to use, quick to setup, can carry a payload of ~1.3 kg, has flight times of ~30 minutes, and is IP43 rated enabling it to be flown in light rain. We

primarily flew it with a DJI X5S integrated RGB camera and gimbal. The DJI X5S camera/gimbal is not IP43 rated like the M210 drone, so a simple rain shield was developed for missions in light rain (Figure 2.23: right). The M210 we used does not have RTK GPS, however M210 drones with RTK GPS are now available, and are recommended for more accurately georeferenced aerial imagery.



Figure 2.23: DJI Matrice 210 (left), with a simple rain shield for the X5S camera and gimbal (right).

### 2.2.3 DJI Matrice 600 Pro

Two DJI Matrice 600 Pro drones were used throughout the ‘drone flow’ project for carrying heavy payloads (up to 5 kg). These drones are easy to setup and use, and also easy to customize. They can be flown manually, or can fly automated flight paths using software such as DJI Ground Station Pro, or Map Pilot. We deployed these drones primarily to carry: (1) the stereoscopic camera; (2) the tracer particle distribution system; (3) the hyperspectral camera system; (4) the terrestrial LiDAR system; (5) the aerial Ground Penetrating Radar (GPR) system. They can also be deployed to carry other payloads such as multispectral, or thermal infrared cameras (if required). When the stereoscopic camera system and tracer particle system were used together, both drones were flown simultaneously by two pilots. As discussed in Sections 2.1.2 and 2.3.4, a channel expansion kit is used for the M600 RC unit (Figure 2.6), enabling convenient triggering of PWM outputs (such as recording imagery from the stereoscopic camera, or dropping tracer particles from the tracer particle distribution system). The attachment rails and dove tail quick release on the M600 also make it convenient for swapping payloads in the field.



Figure 2.24: DJI Matrice 600 Pro drone used for most heavy lift payloads (up to 5 kg) during the ‘drone flow’ project.

#### 2.2.4 Aeronavics Skyjib

The largest drone deployed during the ‘drone flow’ project was a Skyjib multirotor aircraft (Figure 2.25), developed by our collaborators Aeronavics. This drone can carry a payload of up to 7 kg, with a max takeoff weight of 24.9 kg. It can fly for 45 minutes with a 3 kg payload, or 25 minutes with a 7 kg payload. It can also fly in an average wind speed of 40 kmph, and was developed with enhanced water proofing to enable it to fly in heavy rain. This drone is our dedicated heavy lift aircraft, or for aerial flood gauging in challenging conditions (i.e. during or after storms where it is still rainy and windy). Aircraft flight planning is performed using the software Mission Planner. This drone is setup with a DJI quick release mount (from Small Rig Ltd), making it compatible with our wide range of payloads (Figure 2.26). It also has a down looking First Person View (FPV) camera for positioning the drone during surface velocimetry, or surveying missions. While not quite as simple to use as a DJI M600, it is more rugged and customisable, and also has longer flight endurance on a single set of batteries. This drone can be used to fly the same payloads as the M600, but in more challenging weather conditions, or when longer distance flights are needed.



Figure 2.25: Aeronavics Skyjib with the Sony A5100 RGB camera and X-Cam A22-2H gimbal in the Rangitata River, New Zealand.



Figure 2.26: Aeronavics Skyjib with the stereoscopic camera system in the Rangitata River, New Zealand.

## 2.3 Tracer particles

Tracers are needed for surface velocimetry measurements. It is important to select tracers that are a suitable size for detection by the camera (dependent on camera resolution, altitude, and field of view), and suitable buoyancy to minimise surface wind effects (Weitbrecht *et al.*, 2002). Tracers can be naturally occurring objects (e.g. leaves, sticks, foam, and other debris), they can be inherent features of the flow (e.g. advected eddies and other turbulent features), they can be natural thermal differences in water temperature (e.g. Puleo *et al.*, 2012; Legleiter *et al.*, 2017; Kinzel & Legleiter, 2019; Schweitzer & Cowen, 2021), or they can be artificially added tracer particles (sometimes known as seeding). During floods there is often sufficient natural debris and features present for surface velocimetry measurements, however outside of these conditions it is common for channels to have insufficient natural tracers. In these cases it is usually necessary to add artificial tracer particles (Detert *et al.*, 2017; Detert *et al.*, 2019a).

### 2.3.1 Tracer particle selection

#### Field tests of tracer particles:

Field tests were conducted to select an optimal tracer particle for the ‘drone flow’ project and one that could be carried by an aerial tracer particle distribution system. The following candidate tracer particles were tested: wood shavings, wood chips, rice bubbles (breakfast cereal), popcorn, and cheerios (breakfast cereal). Tracer particles were deployed in both plain, and coloured variants (coloured bright pink with biodegradable/edible colouring). They were deployed from a bridge in the Halswell River (Figure 2.27), then imaged with a DJI Phantom 4 Pro drone at three altitudes of 20, 40, and 60 m providing pixel resolution (i.e. ground sample distance) of 6, 12, and 18 mm. The selection criteria for the optimal tracer particles were: light weight, small volume, easily visible (i.e. large surface area and distinctive colour), biodegradable, environmentally neutral, and low cost. All of the tracer particles were easily visible at low altitudes, however rice bubbles were less visible at higher altitudes due to their smaller particle size. Wood chips were much heavier and bulkier than wood shavings (i.e. 3D volume vs predominantly 2D for wood shavings). Popcorn had high buoyancy and a 3D shape that extended above the water surface making it more susceptible to wind loading. All of the ‘edible tracers’ (i.e. rice bubbles, popcorn, and cheerios) were not environmentally neutral as they can be eaten by wildlife (i.e. fish and birds), with fish being observed to eat rice bubbles during a previous deployment. The edible tracer particles were also expensive, making them a poor choice for large scale deployment. As such, the clear winner was wood shavings, which are environmentally neutral (essentially the same as leaves and sticks that are already in rivers) and are made from non-treated wood. Tests of both plain and coloured wood shavings were successful, with coloured wood shavings being more easily distinguishable (and separable) from environmental noise such as sunglint (see Sections 2.3.2 and 2.3.3), whereas plain wood chips were brighter and more easily distinguishable against darker river water without sunglint (Figure 2.28:b). Wood shavings are also very cheap and were sourced from Kiwi Wood Shavings Ltd (Figure 2.28:a).

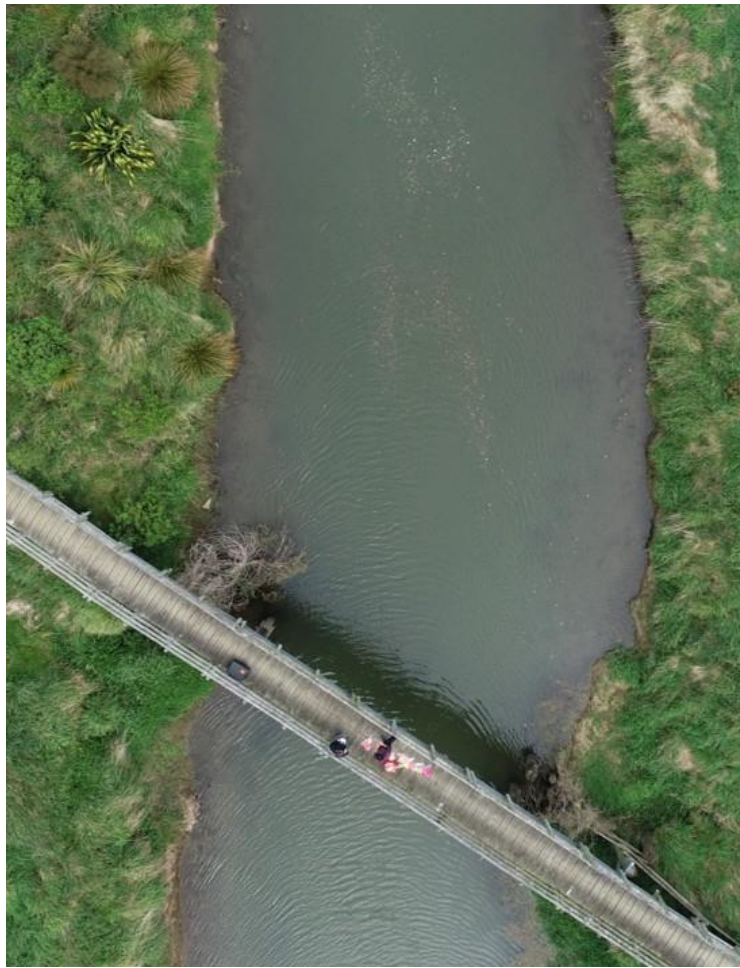


Figure 2.27: Field tests of tracer particles in the Halswell River, New Zealand. Plain wood shavings are visible at the top of the image, while coloured wood shavings (light pink) are visible in the centre of the image.

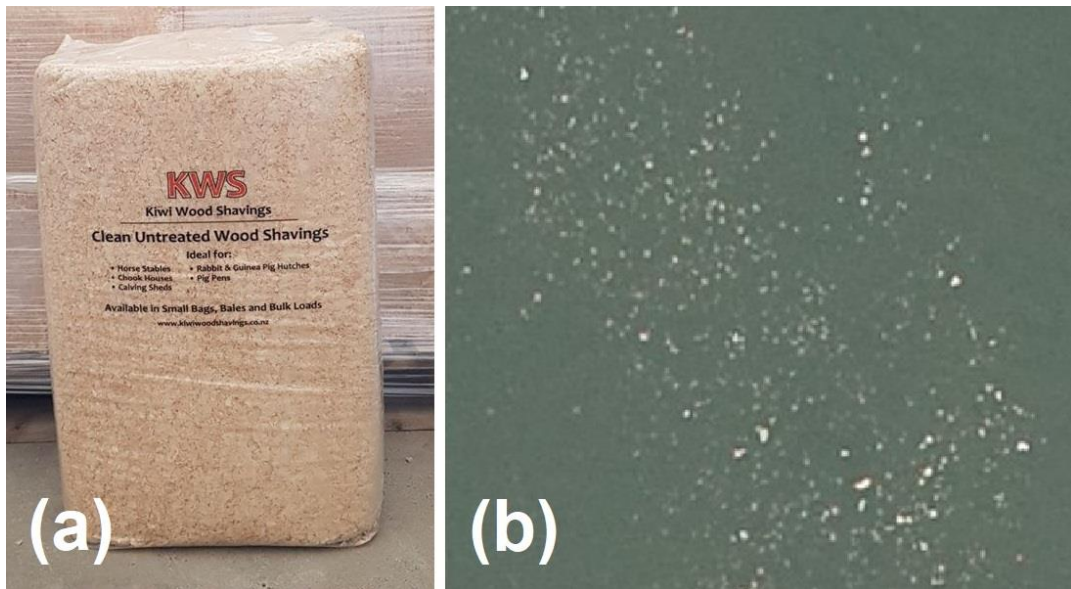


Figure 2.28: (a) Large bag of wood shavings from 'Kiwi Wood Shavings Ltd', (b) plain wood shavings are easily distinguishable against a background of darker river water.

### Pop starch:

Lab tests were also performed to investigate the use of pop starch (e.g. compostable packaging), however it took a long time to dissolve and had too large a volume for a field tracer particle distribution system (i.e. 3D pop starch particles vs 2D wood shavings). Its large volume and buoyancy also make it stick out of the water more, making it more susceptible to wind loading. The large size of pop starch particles makes it suitable for large scale surface velocimetry studies using LSPIV (where particles are visible at higher altitudes and lower ground sample distance), however the large volume of tracers required necessitates deployment from an upstream bridge or boat (Detert *et al.*, 2017; Detert *et al.*, 2019a), precluding its practical use for an aerial tracer particle distribution system carried by a drone.

### Expanding tracer particles:

An ideal tracer particle could be carried in a small volume, then would expand to a larger volume upon deployment. For example, shaving foam or whipped cream from a can, however neither of these substances are ‘environmentally neutral’ and suitable for deployments in rivers. If a suitable substance can be pressurised with dissolved compressed gas (e.g. CO<sub>2</sub> or N<sub>2</sub>O), it could be used in the same way as shaving foam (or whipped cream). Deployment of such a system could also be controlled using an electronic valve and likely a rotary dispersal nozzle for wider coverage. A range of natural foams were tested in the laboratory at the start of the ‘drone flow’ project, including Agar foam, Guar Gum foam, Soy Lecithin foam and Xanthan Gum foam. However, we were not able to produce large quantities of any of these foams, nor were they sufficiently stable for deployment.

Beyond compressed foams, there are many alternative ways to create ‘expanding tracer particles’, e.g.:

- Compressed dry tracer particles that absorb water and expand.
- Compressed dry tracers that are transported under high pressure, then expand at lower pressure when they are released (likely ‘pop starch’ would show these characteristics when compressed under high pressure).
- Dry tracer particles with tiny bubbles of compressed gas trapped within a foam forming binder (e.g. possibly some form of long chain protein), that then expand as the tracer dissolves when in contact with water.
  - This is the same process from which ‘Pop rocks’ candies are made, where tiny bubbles of high-pressure CO<sub>2</sub> are dissolved within the hot liquid candy, then become trapped within the solid candy when it is cooled under high pressure.
- Dry tracer particles that create gas through a chemical reaction when dissolved in water, which then expand within the foam forming binder. Once the right ‘mixture’ was found, these could be pressed into small ‘granules’ or ‘pellets’ that then dissolve upon contact with water and release gas to form foam. There are many substances (or mixtures) that release gas upon contact with water, however two simple examples are:
  - Sodium carbonate dissolving in water Na<sub>2</sub>CO<sub>3</sub> + H<sub>2</sub>O = 2NaOH + CO<sub>2</sub> (although this creates a very basic solution if not adequately diluted and may be unsuitable for rivers).
  - Sodium bicarbonate and citric acid 3NaHCO<sub>3</sub> + C<sub>6</sub>H<sub>8</sub>O<sub>7</sub> = Na<sub>3</sub>C<sub>6</sub>H<sub>5</sub>O<sub>7</sub> + 3CO<sub>2</sub> + 3H<sub>2</sub>O, producing trisodium citrate, carbon dioxide gas, and water.

Exploration of expanding tracer particles and foams in the ‘drone flow’ project was abandoned after a small amount of testing as it was beyond the scope of the project and expertise of the project team. For simplicity ‘wood shavings’ were used as tracer particles in the project. However, the idea of using expanding tracer particles and foams remains valid and would be worth exploring in the future (particularly for a chemical engineering MSc or PhD project). It is also recommended to perform detailed investigation of the use of raindrop splash points (and surface texture) as tracers.

### 2.3.2 Dying tracer particles

The pink coloured natural food dye used in tracer particle tests (Section 2.3.1) was not suitable to upscale to larger deployments, due to high cost, lack of distinctive colour, and poor adherence to wood shavings. As such, other sources of natural dye were explored. An excellent solution was found with ‘Sierra Red’ mulch dye from EnviroColor Ltd (Figure 2.29). This dye is ‘Non-toxic and safe for the environment, people and pets’, making it well suited for colouring tracer particles that are deployed in river environments. Batches of coloured wood shavings were prepared by spreading the wood shavings out on large tarpaulins, mixing up the ‘Sierra Red’ mulch dye in a backpack sprayer by diluting it with water, then spraying it onto the wood shavings (Figure 2.30). After coating the wood shavings, they were mixed with a rake, then another 1-2 coatings of dye were applied to reach the lower layers of wood shavings that were missed on the first pass. The wood shavings were then left to dry for 2-5 days (depending on weather conditions and temperature) before being bagged up ready for field deployments. While the process of producing coloured wood shavings is somewhat labour intensive, they can be produced in large batches on multiple tarpaulins, then only used for deployments where sunglint, dappled sunlight and other sources of environmental noise are interfering with detection of tracer particles and creating errors in calculated surface velocities. Examples of field deployments of coloured tracer particles and environmental noise are shown in Figure 2.31. Basic techniques for separating coloured tracer particles from environmental noise in the HSV colour space are discussed in Section 2.3.2.



Figure 2.29: ‘Sierra Red’ mulch dye from EnviroColor Ltd, which is applied to faded bark chips (or wood shavings in our case) using a backpack sprayer after being diluted with water.



Figure 2.30: Preparing batches of coloured wood shavings by dyeing them with ‘Sierra Red’ mulch dye.



Figure 2.31: Left: Deployment of coloured tracer particles in the Waingawa River, New Zealand. Right: Zoomed example of coloured tracer particles in the Ashley River, New Zealand, where environmental noise due to sunglint and reflections off surface waves, as well as dappled lighting on the riverbed make it very challenging to resolve plain tracer particles (i.e. brightness is not suitable for separation).

### 2.3.3 Thresholding tracer particles to reduce environmental noise

Aerial imagery for surface velocimetry can contain many sources of environmental noise, for example: sunglint, reflections off small surface waves, and dappled sunlight on shallow riverbeds (with clear water). This environmental noise manifests as bright pixels, from which tracer particles can be hard to separate (particularly if their defining characteristic is brightness rather than colour). This environmental noise can be very problematic for processing surface velocimetry imagery (particularly with LSPIV) and can result in spurious velocity vectors. STIV is somewhat less susceptible to this noise if only long displacement trajectories of tracers are considered, however it can still create problems. During the ‘drone flow’ project simple techniques were developed to circumvent this environmental ‘brightness’ noise by using coloured tracer particles, recording RGB aerial imagery, and thresholding aerial imagery in the Hue Saturation Value (HSV) colour space where brightness (value) is separated from colour (hue). Thresholding was performed easily in MATLAB using either the ‘Color Thresholder App’ (Figure 2.32), or code. Orthorectified and thresholded aerial imagery can then be processed in MATLAB or using other software (such as Fudaa-LSPIV) to obtain surface velocities. During the ‘drone flow’ project only red and plain tracer particles were used, however future work to explore other distinctive colours and background combinations is also recommended (e.g. black tracer particles against bright/turbid river water, or for deployments with persistent sunglint).

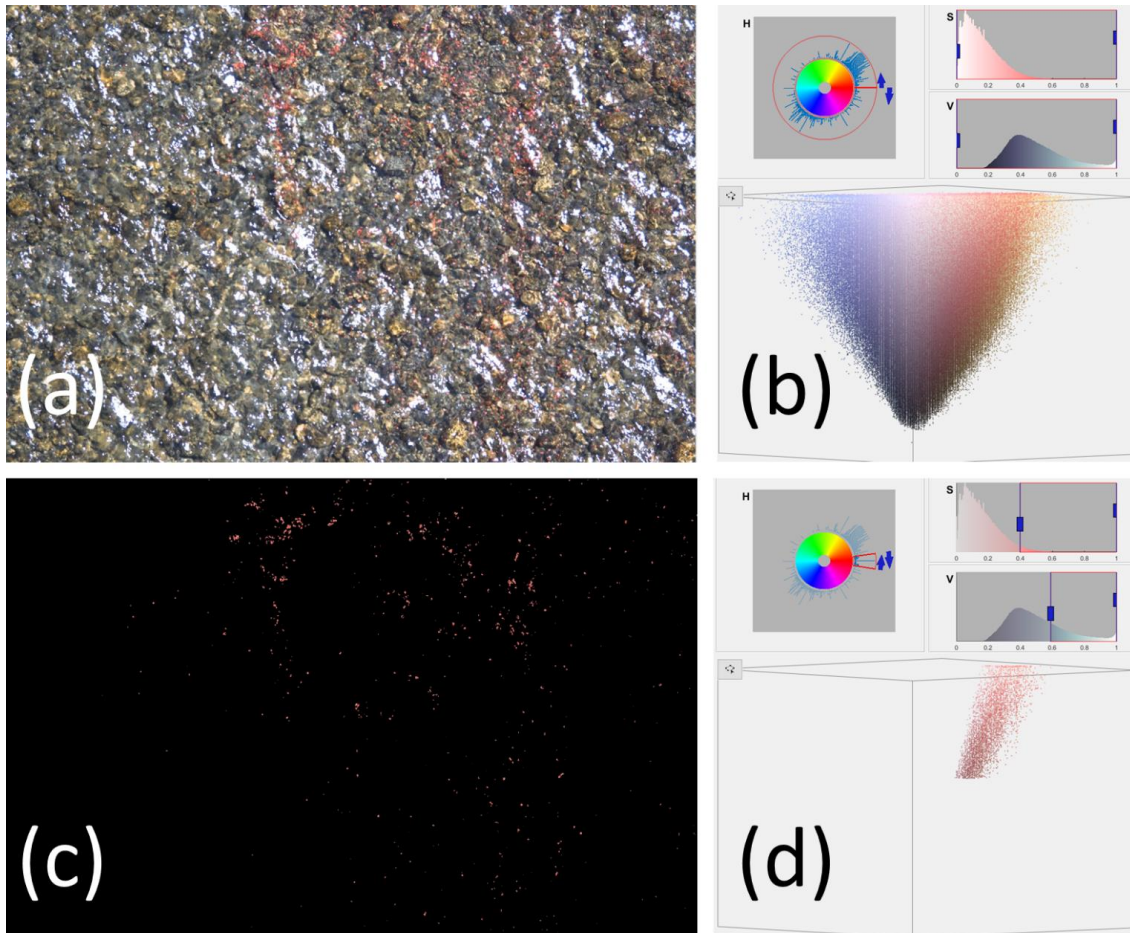


Figure 2.32: (a) Coloured tracer particles and surface sunglint (Ashley River, New Zealand); (b) visualisation of all the image data in the HSV colour space; (c) thresholded image to only resolve the tracer particles; (d) visualisation of the thresholded image data in the HSV colour space.

### 2.3.4 Tracer particle distribution system

To distribute tracer particles from the air a novel tracer particle distribution system was developed. It was designed to be carried by a DJI M600 or an Aeronavics Skyjib drone. The aerial tracer particle distribution system enables surface velocity measurements where they are not possible due to insufficient natural tracers, or where there is not a suitable upstream bank/bridge to release them. This enables measurements in much larger rivers than are possible with bank released tracer particles. An aerial tracer particle distribution system can also achieve wider simultaneous spatial coverage (than manually released tracer particles) since they can be released from altitude and disperse with rotor wash (and atmospheric wind/turbulence) as they descend to the river surface. An aerial tracer particle distribution system can also be flown in a ‘crescent’ shape upstream from the imaging drone, providing more time for slower moving near bank tracer particles to reach the measurement cross section than those in the centre of the channel, enabling all tracer particles to reach the measurement cross section at a similar time.

The tracer particle distribution system was designed to carry biodegradable wood shavings (Section 2.3.1) and was designed with a hexagonal shape to fit between the landing legs of a DJI M600 drone. The first prototype was designed in Autodesk Inventor and fabricated out of steel for rapid testing<sup>7</sup>. This prototype had two counter-rotating screw augers situated in channels along the bottom of the ‘hopper’ to push the tracer particles out (Figure 2.33).



Figure 2.33: Steel prototype of the first tracer particle distribution system design (with two counter rotating screw augers) during benchtop testing (a), and outdoor testing under a DJI M600 drone (b).

Two screw augers in the prototype were found to not provide sufficient span across the bottom of the hopper, with wood shaving becoming stuck with an air cavity around the augers (known as bridging). The final design (Figure 2.34) has three aluminium screw augers, with two rotating in the same direction and another counter rotating (Figure 2.34 b,d). A golf ball was added to the hopper to bounce around and break up any residual bridging of wood shavings near the exit of the hopper. The walls of the hopper were fabricated from fiberglass, while the bottom channels of the hopper (housing the screw augers) and the bearing plates were 3D printed in sections using a Markforged X7 3D printer out of Onyx material, with continuous carbon fibre reinforcement (see Section 2.5.6 and Appendix D).

<sup>7</sup> Credit to Geoff Todd at Todd Augers and Equipment Ltd for fabrication of the initial prototype, and Brendon Smith at NIWA for mechanical design.

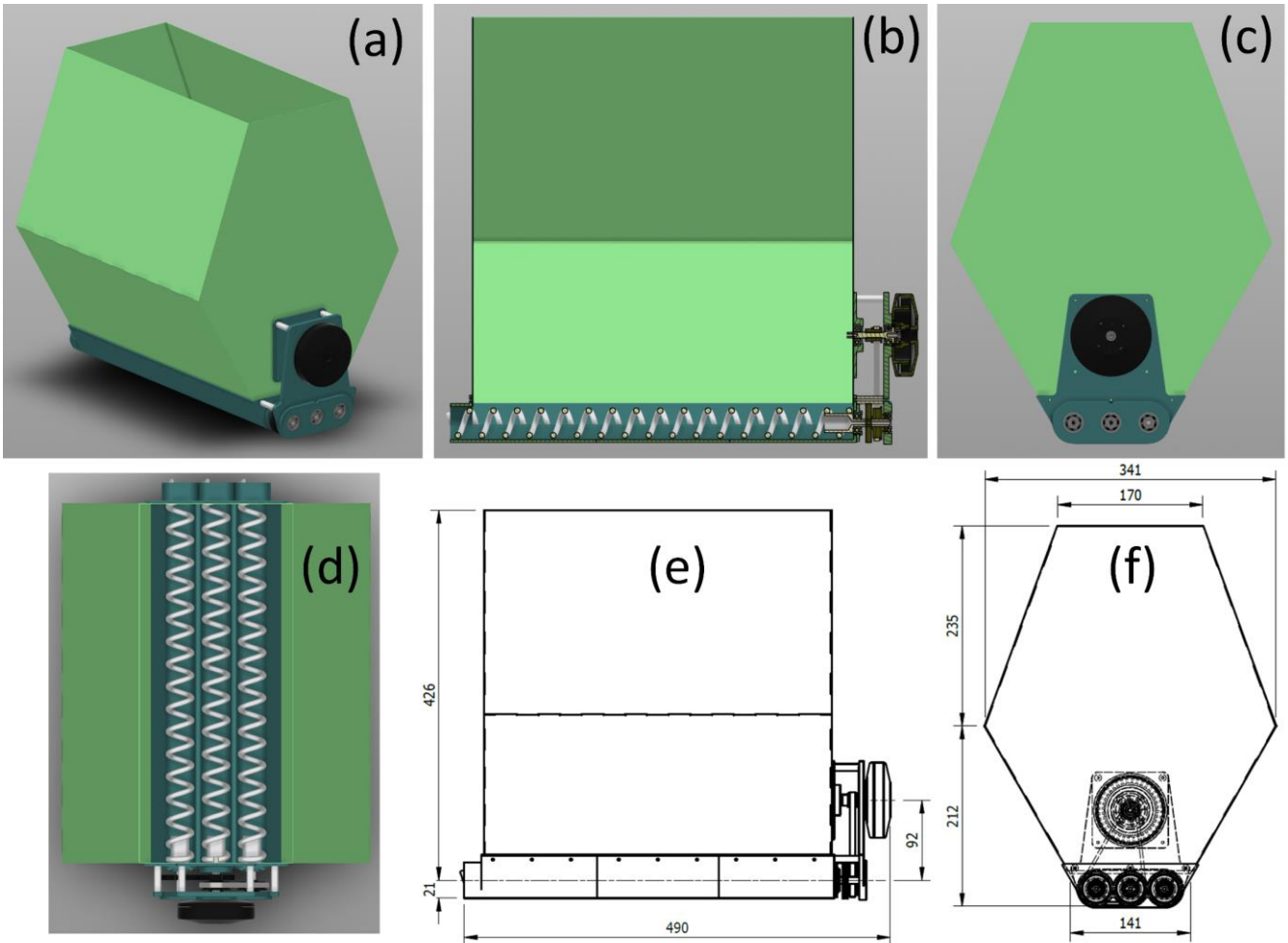


Figure 2.34: The final tracer particle distribution system design (featuring three screw augers): (a) oblique view, (b) section view, (c) front view, (d) top view, (e) side dimensions, (f) front dimensions.

The weight of the system is 2.5 kg without tracer particles and 5.5 kg fully loaded with tracer particles (Figure 2.35a), with an internal volume of ~41 L. A U8 Pro KV170 drone motor from T-MOTOR is used to drive the screw augers through a reduction gearbox (Figure 2.35b). Power is provided directly from the DJI M600 drone, with a UAS 55+ Electronic Speed Controller (ESC) from KDE Direct used to control the tracer particle distribution system motor. A Pulse Wave Modulation (PWM) cable is connected from the speed controller to the A3 flight controller on the M600 drone and a rotary switch on the Remote Control (RC) unit channel expansion kit (Figure 2.36) has been configured to control the speed of the motor (and thus auger rotation rates). This enables initialisation and control of the tracer particle release rate by the drone pilot during flight. The PWM output from the A3 flight controller and the RC unit rotary switch are configured using the software ‘DJI Assistant for Matrice’, which is similar to the stereoscopic camera triggering (see Section 2.1.2). The system is housed in a large size DJI Matrice 600 Case (GPC-DJI-M600) from Go Professional Cases, and can be transported to the field fully assembled for rapid deployment (Figure 2.35c).

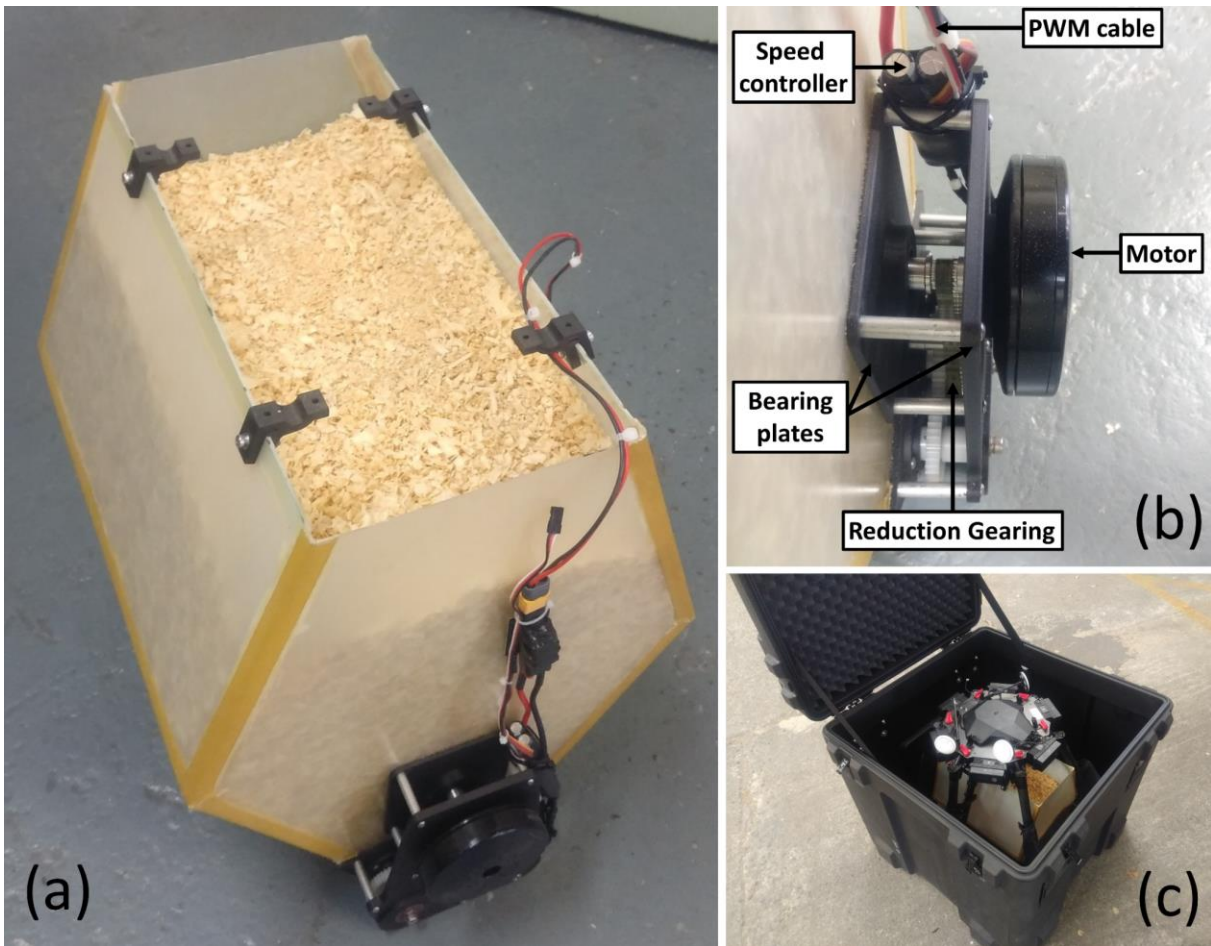


Figure 2.35: (a) Final construction of the tracer particle distribution system and loading with wood shavings, (b) motor, gearbox, speed controller and bearing assembly, (c) the full system ready for field deployment.



Figure 2.36: The RC unit for the DJI M600 drone has a channel expansion kit, with a rotary switch used to control the feed rate of the tracer particle distribution system, through a PWM output from the DJI A3 flight controller to the speed controller on the tracer particle distribution system.

At the maximum feed rate the full hopper of tracer particles is emptied in approximately 5 minutes (Figure 2.37). Maximum flight times on the DJI M600 drone with a fully laden system and DJI TB47S batteries are around 15 minutes. Depending on the required distribution of tracer particles, the feed rate is usually set so that the full hopper is emptied within 10 minutes, allowing 5 minutes of battery life for takeoff, getting to/from the distribution location, and landing. Tracer particles are reloaded into the distribution system from large polythene bags (Figure 2.38), or are added via a PVC chute. Reloading the system with tracer particles takes approximately 5 minutes. One load of tracer particles is sufficient for one surface velocity measurement, providing sufficient tracer particle density for LSPIV in small rivers/channels, or STIV in larger rivers/channels. The tracer particle distribution system can be used with plain/coloured wood shavings, or a combination of both (Figure 2.38).



Figure 2.37: Tracer particle distribution system during laboratory testing of feed rates.



Figure 2.38: NIWA field technician Hamish Sutton loads the tracer particle distribution system in the Rangitata River, New Zealand, before a surface velocimetry mission.

#### Field deployments:

The height at which the system is flown depends on the desired density of tracer particles on the water surface, which is a function of channel width, surface velocity, and the processing method that will be used (i.e. LSPIV, PTV, or STIV). During flight, the tracer particles are well dispersed by the rotor wash, however, if the drone is flown at too high an altitude it can be hard to aim the descending cloud of tracer particles (particularly if there is any wind) and tracer particles may land outside of the channel. For small channels (i.e. less than 20 m wide) the system is typically hovered statically, and the entire channel is covered simultaneously. For larger channels, the system is typically flown from one bank to another distributing tracer particles across the water surface. Ideally the drone is flown upstream in a crescent shape, since tracer particles from the centre of the channel will move faster than those near the banks, enabling them to reach the measurement cross section at similar times. The tracer particle distribution system is typically flown 50 to 100 m upstream of the field of view of the drone that is used for surface velocimetry. A 10 minute distribution of tracer particles typically results in 3-4 minutes of imagery that can be used for surface velocimetry, where full coverage of tracer particles at the measurement cross section is achieved. For larger channels (i.e. wider than 20 m) and flowing relatively swiftly (i.e. speeds greater than 1 m/s) it is not usually possible to achieve sufficient tracer particle densities for LSPIV, and in these cases STIV or PTV should be used to obtain surface velocities. Examples of field deployments of the tracer particle distribution system are shown in (Figure 2.39 to Figure 2.41).



Figure 2.39: Tracer particle distribution system in the Rangitata River, New Zealand.



Figure 2.40: The descending cloud of tracer particles, with individual wood shavings being visible.



Figure 2.41: Deployment of the tracer particle distribution system in the Tekapo Canal, New Zealand.

#### Future improvements:

- The system has occasionally jammed during field deployments, requiring it to be landed and the blockage cleared by manually turning the motor (and thus augers) in reverse. An upgrade is currently in progress to fix this issue, by replacing the speed controller with one that can reverse (enabling a blockage to be cleared midflight), and also to slightly enlarge the exit holes of the hopper (to prevent blockages from occurring in the first place).
- It would also be useful to develop a procedure for screening tracer particles (i.e. wood shavings) to remove small particles and dust, that take up weight but are not sufficiently large to be useful as tracers.
- Likewise a better procedure (or piece of equipment) for colouring the tracer particles, then drying them would also be useful.

Overall the tracer particle distribution system is well designed and fit for purpose. For further significant upgrades of aerial tracer particle dispersal, it is recommended to explore different tracer particles that can expand, allowing larger volumes of tracer particles to be carried by a drone (see Section 2.3.1 – Expanding tracer particles).

## 2.4 Surveying equipment

### 2.4.1 RTK GPS

Accurate surveying with Real-Time Kinematic (RTK) Global Positioning System (GPS) equipment is essential for most river remote sensing work, such as aerial surveying and surface velocimetry. RTK GPS equipment is used for surveying in Ground Control Points (GCPs), measuring channel widths, measuring waters edge locations, measuring shallow water bathymetry, and many more applications.

There is a wide range of RTK GPS surveying equipment available, however at NIWA (Christchurch office) we typically use a Trimble R10 base station (Figure 2.42a) and two Trimble R10 Rovers (Figure 2.42b). Most large organisations who undertake river remote sensing should already have their own RTK GPS equipment, however for those that do not, the equipment can be rented.



Figure 2.42: (a) Trimble R10 RTK GPS base station, (b) 2x Trimble R10 Rovers.

#### 2.4.2        **Ground Control Points (GCPs) – Terrestrial**

To georeference aerial imagery it is important to use GCPs. GCPs can be made from weatherproof canvas and should have a clearly defined centre (Figure 2.43). Temporary GCPs can be held down with rocks, surveyed with RTK GPS, and collected after flights. Sites where repeated monitoring occurs may benefit from the installation of more permanent GCPs that only need to be surveyed once.

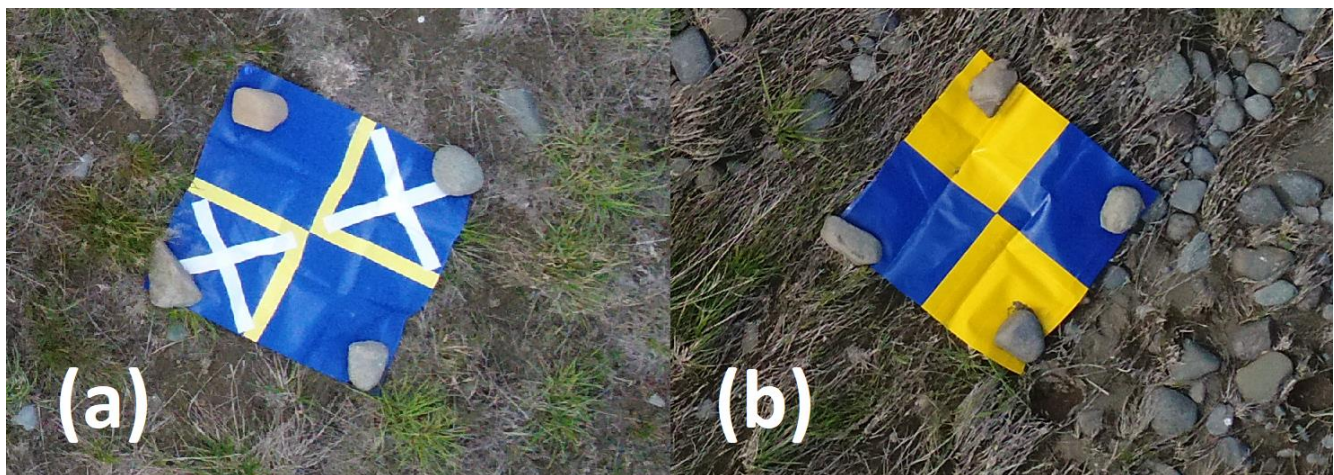


Figure 2.43: Ground control points that are easily visible in aerial imagery and have a clear centre to survey (Biggs, 2020).

To assist with making GCPs, the ‘drone flow’ software toolbox (Appendix A) contains code to generate numbered GCP images in three formats:

1. ‘makeGroundControlPointsNumOnly.m’ (Figure 2.44:left)
2. ‘makeGroundControlPointsBlueYellowCanvas.m’ (Figure 2.44:centre)
3. ‘makeGroundControlPointsBlueYellow.m’ (Figure 2.44:right)

The uniquely numbered images can be printed on canvas (i.e. Figure 2.44:centre), or on paper and laminated. If they are printed on paper (i.e. A3 size), it is suggested to cut (or drill) holes in the corners (Figure 2.44:right). These holes will then be filled when laminated, then smaller holes can be cut/drilled through the centre of the larger holes (i.e. through the sealed laminate). This enables tent pegs to be placed through the corners to secure them, but retains the waterproofing provided by lamination. To see GCP numbers easily Figure 2.44:left can be used, however it is not generally recommended for aerial surveying as it is harder to see (not coloured) and does not have an easily visible centre for surveying.

For anyone seeking GCP images to print (without needing MATLAB to generate them), we have provided 100x sequentially numbered Blue/Yellow GCPs through the GitHub repository <https://github.com/HamishBiggs/DroneFlow>. ‘GCPsBlueYellowCanvas.zip’ contains images without cut holes (Figure 2.44:centre) and ‘GCPsBlueYellowA3.zip’ contains images with cut holes (Figure 2.44:right).



Figure 2.44: Plain GCP with large numbers (left); coloured GCP with numbers and a well-defined centre for surveying, suitable for canvas (centre) or paper with corners holes cut out before lamination (right).

### 2.4.3 Ground Control Points (GCPs) – Underwater

For surveys of wide and very shallow rivers, it may also be necessary to deploy GCPs within the wetted channel. White painted rocks work well as underwater GCPs. However, they do take time to paint and can be unsightly if left at a river site following a survey. For reusable underwater GCPs we recommend stainless steel plates (150 × 150 mm) with circular holes to let water through (Biggs *et al.*, 2022b). These sit nicely on the riverbed and can be easily stacked for transport to and from the field site. We tested a range of colours (Figure 2.45a) and found that white was generally the brightest and best (Figure 2.45b). It is important to paint the underwater GCPs, rather than leaving them as polished stainless steel. If left unpainted they act as a mirror and reflect the light and colour of objects around them (rather than diffuse white light) making them harder to see. Painting the GCPs is easy, with a base coat of grey metal etching primer applied first, then a topcoat of white paint. Once deployed, they can be surveyed with RTK GPS the same way as GCPs deployed on land by surveying the middle of the central hole (Figure 2.45b).

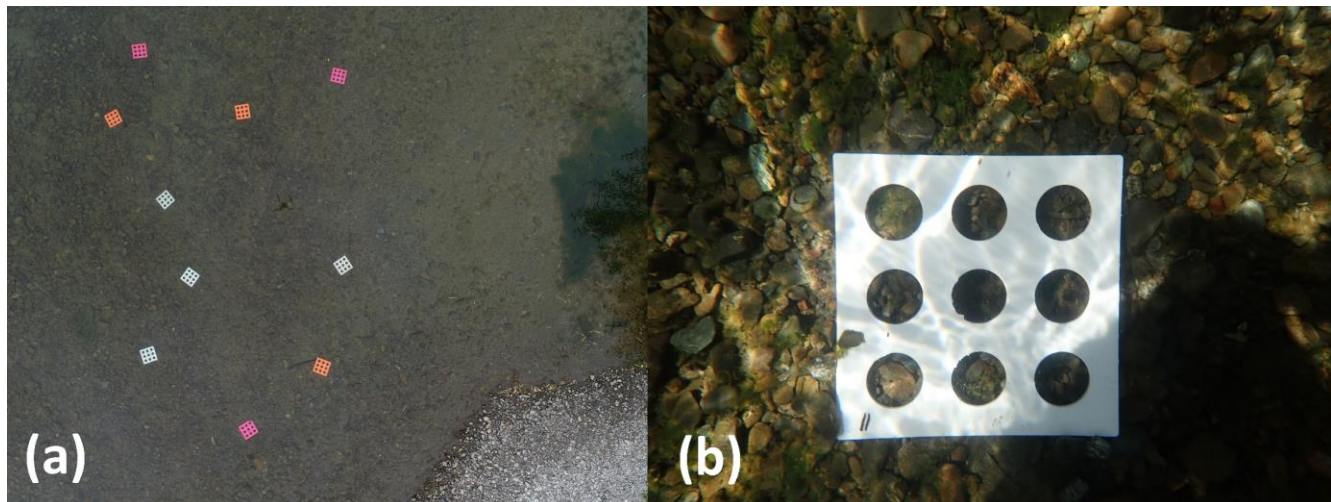


Figure 2.45: (a) Tests to select underwater Ground Control Point (GCP) colour. (b) Underwater GCP deployed in the Hutt River.

For generation of Digital Surface Models (DSMs) and Digital Elevation Models (DEMs) from underwater imagery (see Sections 2.1.4 and 4.7.4) it can be necessary to deploy more GCPs, and to use smaller ones so that they do not obscure the view of the riverbed. We found that stainless steel square washers (size M20 50 x 50 x 3 mm) work well (Figure 2.46). They are cheap, relatively heavy, and have a central hole to allow water to flow through them, reducing the likelihood of them being moved by river flow and turbulence. For most deployments 3 mm thickness is sufficient, however if water is swifter then 6 mm thick washers are recommended for increased weight. Similar to the larger underwater GCP plates for aerial imagery (Figure 2.45) the stainless steel washers also have a well-defined centre for surveying with RTK GPS. If these washers are going to be used regularly and are expected to have a long operational life, then the purchase of stainless steel washers is recommended, if not then galvanized washers are a cheaper alternative. We did not paint the washers white as we did for the metal plates, however this step is also recommended for the washers if they are going to be used repeatedly, as this will avoid bright reflections (Figure 2.46) and make them more easily visible. It is also recommended to number the white painted washers using a black paint pen.



Figure 2.46: Using 25 mm stainless steel square washers as underwater GCPs.

#### 2.4.1        Ground Control Points (GCPs) – Thermal infrared

Thermal infrared GCPs should be distinctive compared to the background environment. This can either be achieved making GCPs from black body radiators with a different temperature than the background environment (e.g. a block of ice on a hot day, or a bucket of boiling water), or they can be made of a material that has a different emissivity (i.e. GCPs that are not black body radiators). Polished metal, such as aluminium baking trays provide a cheap and convenient way to produce thermal infrared GCPs. An arrow can be cut into them to define a precise centre, and they can be distributed around river sites with rocks to weigh them down (Figure 2.47). In thermal infrared imagery they will show up as extremely cold areas, due to the very low emissivity of their polished metal surface (~0.039-0.057), compared to water that is close to a black body (~0.95-0.963) and most natural rocks are grey/black bodies<sup>8</sup>.



Figure 2.47: Aluminium GCPs for thermal infrared remote sensing and mapping.

<sup>8</sup> [https://www.engineeringtoolbox.com/emissivity-coefficients-d\\_447.html](https://www.engineeringtoolbox.com/emissivity-coefficients-d_447.html)

## 2.5 Other equipment

### 2.5.1 Acoustic Doppler Current Profiler (ADCP)

During the ‘drone flow’ project the most commonly deployed ADCP was the Teledyne River Pro to provide reference discharge and to measure reference bathymetry (see Sections 4.7.1 and 4.7.3). This ADCP was predominantly deployed from taglines with a traveler and stabilisation drogue (Figure 2.48), however it was also deployed from a cableway in the Hurunui River during a flood. The Teledyne River Pro can be deployed on a range of boat hulls suitable for different measurement conditions. We also developed an aluminium stabilisation frame for the River Pro, to hold it orthogonal to the measurement cross section for coupled measurements of velocity profiles and wind (Figure 2.49). Processing of moving boat ADCP data for discharge is usually performed in QRev, with bathymetry extracted and processed using MATLAB code developed during the ‘drone flow’ project (see Section 4.7.1 and Appendix A). Alternatively, discharge can be evaluated using section methods with static ADCP positions in the software SxS Pro. The use of SxS Pro is recommended during floods with mobile bed conditions. Cross section bathymetry can also be easily exported from SxS Pro (see Section 4.7.2). ADCP boat hulls were also used to deploy narrow beam depth sounders for highly accurate reference bathymetry measurements (see Sections 2.5.3 and 4.7.3).



Figure 2.48: (a) Teledyne River Pro ADCP deployed in the Tekapo Canal in New Zealand, with a drogue for stabilisation and a flying fox traveller for consistent lateral velocity.



Figure 2.49: Aluminium stabilisation frame for River Pro ADCP to maintain orientation orthogonal to the cross section (left). Deployment of the ADCP and stabilisation frame in a hydro-power canal in New Zealand for wind and velocity profile measurements (right).

### 2.5.2        ADCP benthic lander

An ADCP benthic lander was developed to perform long duration measurements of velocity profiles and the effect of surface wind. This lander was designed in Autodesk Inventor and was primarily fabricated from stainless steel (Figure 2.50). The benthic lander was fabricated from stainless steel to have a long deployment life and to provide sufficient weight to hold it stably to the bed of the channel. The mass of the fully assembled lander was 60 kg, allowing it to be carried by two team members. The weight of the fully assembled lander was 35 kg when underwater (i.e. mass minus buoyancy), with 35 kg being deemed suitable to stably hold it to the bed of relatively slowly flowing channels. An Ultra High Molecular Weight Polyethylene (UHMWPE) skid plate was attached to the bottom of the lander (Figure 2.50) so that it could be deployed in hydro-power canals (notably the Tekapo Canal in New Zealand) without damaging the canal lining. Holes were cut in the base plate to allow water to pass through the plate during deployment and recovery. The holes also helped to hold it in place on the channel bed and to reduce the risk of water getting under the plate and lifting it. The ADCP benthic lander consisted of a Nortek Signature ADCP, battery, and a backup Nortek Aquadopp ADCP (Figure 2.51). The ADCP benthic lander was deployed from an inflatable boat (Figure 2.52) and tethered to both banks with chain. CAD files for the benthic lander are available through the GitHub repository (Appendix D).

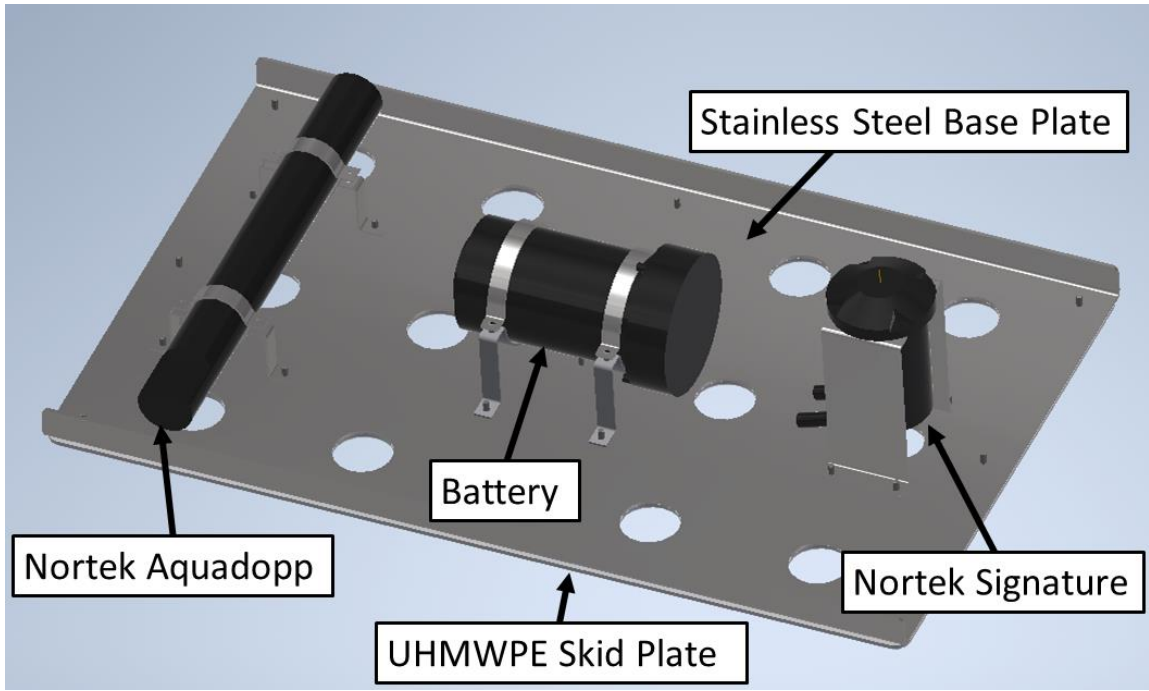


Figure 2.50: Design of the stainless-steel base plate and mounting brackets in Autodesk Inventor.

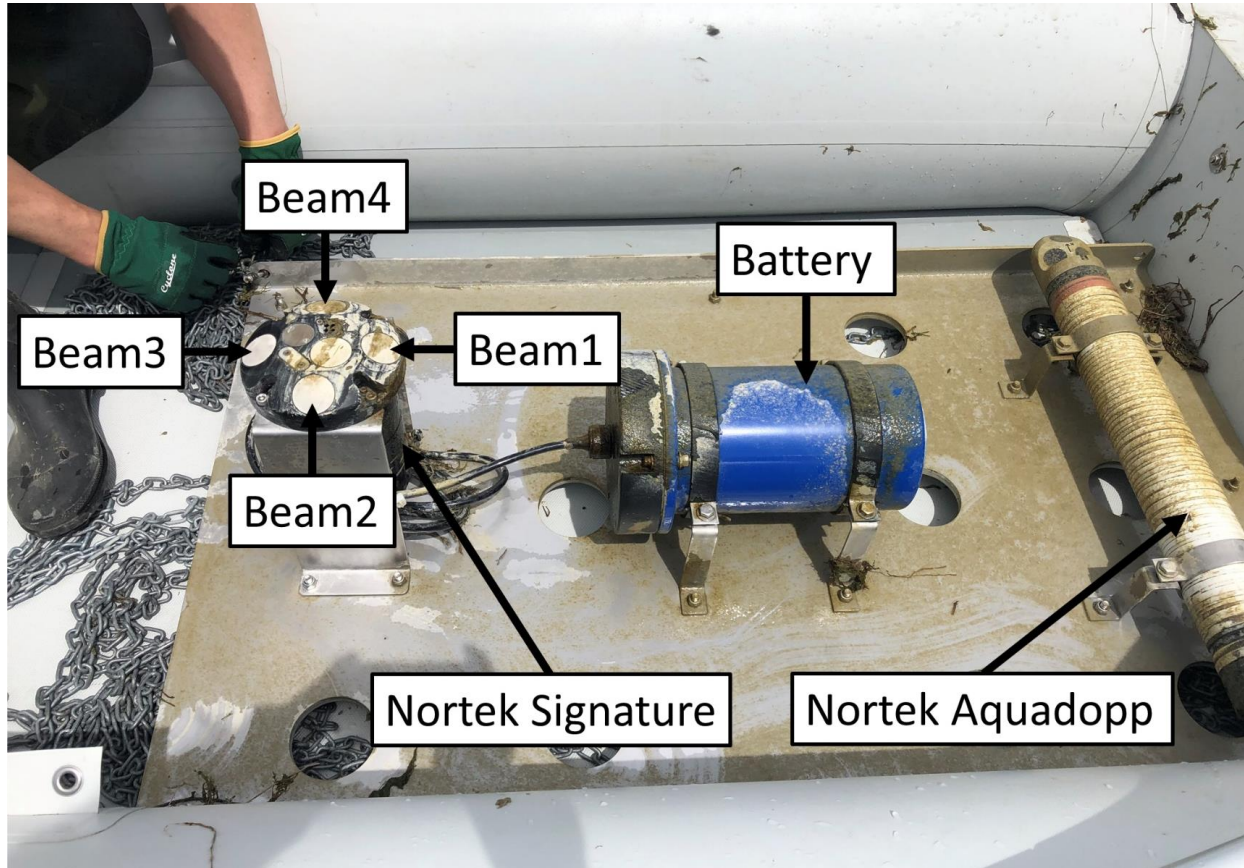


Figure 2.51: Up looking ADCP benthic lander following a 35 day deployment in the Tekapo hydro-canal. The ADCP benthic lander consists of a stainless-steel baseplate, Nortek Signature ADCP, battery, and Nortek Aquadopp ADCP.



Figure 2.52: Deployment of ADCP benthic lander in the Tekapo Canal from an inflatable boat.

### 2.5.3 Depth sounder

To provide reference bathymetry data a Tritech PA500 depth sounder was used. This depth sounder was connected to a Trimble R10 RTK GPS Rover and configured to acquire a new depth measurement if it moved a certain distance from its previous location (usually configured to 10 cm). The PA500 operates at 500 kHz, with a narrow 6° conical beam. It can operate in depth ranges of 0.3 to 50 m, or 0.1 to 10 m, with the latter used for shallow river applications. The use of RTK GPS enabled precisely georeferenced depth and water surface elevation measurements. The PA500 transducer draft (i.e. offset to water surface) was 8.5 cm, and with a blanking distance of 10cm, the shallowest that could be measured was 18.5 cm. This was not usually problematic, with shallow parts of cross sections near the channel banks measured manually with RTK GPS Rovers and survey staffs.



Figure 2.53: Tritech PA500 depth sounder connected to Trimble R10 RTK GPS Rover and mounted on an ADCP boat hull.

#### 2.5.4 Ground Penetrating Radar (GPR)

Remote sensing of river bathymetry during floods is a significant challenge due to high turbidity and deep water, which prevents the use of methods such as: bathymetric lidar, bathymetry from through water imagery corrected for surface refraction, or bathymetry from colour (saturated signal). However, remote sensing of river bathymetry during floods is arguably one of the most important applications, since these are the conditions where instream measurements often pose a health and safety risk to field staff, or are simply not possible when conditions are too extreme. It is also important to collect bathymetry (i.e. cross sections) at the same time as surface velocities during floods, because there can be significant geomorphic change after the surface velocities were measured. For example, capturing surface velocities at a flood peak, then significant deposition and morphological change occurs on the falling limb, resulting in serious discrepancies between the actual cross section when surface velocities were measured, and the cross section surveyed after the flood. There are other methods to remote sense bathymetry in deep, turbid, turbulent water (i.e. turbulence metrics or surface waves (Section 4.7.9)), however, neither of these are particularly practical for field hydrologists, as they require high densities of tracer particles, complicated analysis, and often specialised equipment. To address this knowledge gap, the ‘drone flow’ project tested the use of aerial Ground Penetrating Radar (GPR) to remotely sense river bathymetry.

The idea to use ground penetrating radar to extract bathymetry is not new (e.g. Annan & Davis, 1977; Beres & Haeni, 1991). Nor is the idea to estimate discharge from bathymetric cross sections using GPR and surface velocity measurements. For example, proof of concepts for this method were demonstrated by Spicer *et al.*, (1997) and Costa *et al.*, (2000), with GPR even deployed from a helicopter by Melcher *et al.*, (2002). Further progress with GPR suspended from cableways and bridges, combined with doppler radar for surface velocities was made by Costa *et al.*, (2006) and Hong *et al.*, (2017). However, there

have been three significant developments since this pioneering work. These are: (1) light weight GPR antennas and data collection electronics, (2) heavy lift drones capable of carrying the GPR antennas and measurement electronics, (3) the development of routine (and accurate) methods for evaluating surface velocities from the air, such as LSPIV and STIV using aerial imagery. This now means that cross sections and surface velocities can be evaluated at locations without a cableway or bridge (Costa *et al.*, 2000), or without requiring expensive helicopter deployments (Melcher *et al.*, 2002). Progress has already been made by the USGS (Lane *et al.*, 2020) however, this is a rapidly developing area of research.

The aerial GPR system used was the MALÅ GeoDrone80. It has a weight of 3.23 kg (including batteries) with a centre frequency of 80 MHz. It has two antennas (one for transmit and one for receive), a central acquisition and processing unit, and a GNSS antenna cable. It can be easily mounted on a DJI M600 drone (Figure 2.54), with an addition GNSS antenna added to the top of the drone. The GPR system can be flown manually, or with automatic flight paths. However, automatic flight paths are somewhat risky due to the very low recommended flight altitude of the GPR unit (~ 2-5 m). Any deviations in measured altitude from barometric pressure by the drone could result in a crash if not observed and corrected for manually. Likewise, automatic flight paths that have not been properly surveyed prior to deployment are a high risk, since they can easily intersect with riparian vegetation, banks, and other obstructions. Even the use of a high-resolution DSM for flight planning is not usually suitable, since most drones are incapable of sufficiently accurate 3D spatial positioning from GPS and barometric pressure data (unless the drone uses RTK GPS). As such, we flew the MALÅ GeoDrone80 manually during all field tests, paying close attention to reported altitude, observed altitude, and proximity to obstacles.



Figure 2.54: MALÅ GeoDrone80 mounted on a DJI M600 drone and deployed in the Rangitata River, New Zealand for cross sections of bathymetry.

### Field deployments:

We deployed the MALÅ GeoDrone80 to measure cross sections of bathymetry in the Rangitata River, Waimakariri River during a flood (Figure 2.55), and a Hydro Canal in New Zealand. Cross sections are initiated with the GeoDrone80 handheld unit, then stored locally on the GPR antenna during the measurement and downloaded to the handheld unit after the cross section is completed. Due to poor Wi-Fi range and interference, the GPR cross sections needed to be commenced at takeoff, then downloaded when the GPR antenna returned, with measurements split into cross section passes during post processing in the software GPR Slice. The very low recommended flight altitude (~ 2-5 m) makes it challenging and risky to deploy the aerial GPR system at sites with riparian vegetation (i.e. some braided rivers), or to obtain cross sections up to the far bank of the river, where collision with overhanging riparian vegetation could occur. It is very hard to judge horizontal distance/displacement from ground level, and we highly recommend hovering a second drone over the far bank with its camera pointing nadir, and the far bank in the centre of the transmitted imagery (Figure 2.56). This enables feedback from the second drone pilot to the first drone pilot, enabling the GPR unit to be flown within a safe distance of the far bank and overhanging riparian vegetation. However, for this method to work reliably it should be noted that the camera on the second drone must be pointing nadir (vertical) and the centre of the image must be on the edge of the bank (or the point where the GPR unit should stop flying) otherwise parallax errors can occur due to the height of the GPR unit and the height of obstacles/vegetation, creating discrepancies between their actual, and projected locations. Alternatively, forward facing and downward facing FPV cameras could be used, or other means of obstacle detection and avoidance. By manually flying the GPR unit and using precautions such as a second spotter drone, we were able to successfully deploy the GPR unit without incident.



Figure 2.55: MALÅ GeoDrone80 mounted on a DJI M600 drone and deployed in the Waimakariri River, New Zealand for cross sections of bathymetry during a flood.



Figure 2.56: Using nadir FPV aerial imagery from a DJI M210 drone flown by a second pilot to fine tune proximity to the far bank of the river (river width and distance from the pilots is ~300 m).

Data from the MALÅ GeoDrone80 was processed in the software GPR slice to extract raw bathymetry data, then post processed in MATLAB (see Section 4.7.5). GPR data from the MALÅ GeoDrone80 was quite noisy, particularly near the riverbanks with through air returns from terrestrial objects<sup>9</sup>. GPR signals travel ~10 times faster in air than in water (Annan, 2003; Baker *et al.*, 2007), thus reflections from terrestrial objects that are relatively far away will be picked up. In our case a consistent signal from the downstream bridge was easily identified near the bottom of the radargrams. These reflections become more problematic in narrower channels, and when the drone approaches channel banks (particularly when they are covered in solid structures and vegetation), making it harder to distinguish near bank river bathymetry.

Recommended future work:

- A direct comparison between the MALÅ GeoDrone 80 and other antennas such as the RadarTeam Cobra SE-70 or SE-150 is recommended to investigate ‘ringing’ and other noise in the data. The Cobra SE-70 and SE-150 are semi-shielded airborne/air-coupled antennas (rather than dipoles that should be ground coupled) and may produce cleaner radargrams<sup>10</sup>.
- Investigation of GPR antenna gain patterns and directionality.
- Incorporation of RTK (or PPK) GPS for origin, and a high resolution IMU for orientation, for improved real-world location reconstruction.
- Incorporation of a range finder for low altitude terrain following.
- Incorporation of FPV cameras, or other means of obstacle detection and avoidance for low altitude flights.
- Investigation of methods for removing reflections from terrestrial objects using modeled reflections from DEMs (or DSMs) and antenna gain patterns, for noise reduction and improved directionality.

<sup>9</sup> [https://gpg.geosci.xyz/content/GPR/GPR\\_fundamental\\_principles.html](https://gpg.geosci.xyz/content/GPR/GPR_fundamental_principles.html)

<sup>10</sup> <https://jbuas.co.uk/ugcs-drone-gpr/>

## 2.5.5 Wind measurements

One of the key outputs from the ‘drone flow’ project was a detailed investigation of conversions from surface velocity to depth average velocity (Biggs, *et al.*, 2021). However, these relationships are significantly complicated by surface wind effects (Section 4.8). In New Zealand strong winds at measurement sites are common and the extent to which this affects surface velocities remains to be determined. During the ‘drone flow’ project a range of detailed field studies were conducted to investigate the effects of surface wind and practical ways to account for it. These studies were conducted in conjunction with the NIWA eFlows project FWWA2103 and Envirolink Advice project C01X2008 2115-TSDC176, with data analysis ongoing at the time of writing this user guide.

For basic characterisation of wind velocities (during surface velocimetry measurements) a handheld anemometer such as the ProTech QM1646 can be used (Figure 2.57: Left). When these basic anemometers are deployed, complementary information about wind direction relative to the channel must be included, since they have no directional reference (Biggs *et al.*, 2021). The use of simple anemometers enables Quality Control (QC) information to be added about the approximate wind conditions at the study site, however they do not enable the collection of accurate data for scientific analysis.

For improved wind measurements a 2D climate station such as the Vaisala WXT536 can be used (Figure 2.57: Right). The WXT536 can be mounted on the channel bank for long duration characterisation of wind conditions at the site (for example at a fixed camera gauging station), or it can be mounted on an ADCP for measurement of wind velocities near the water’s surface (Figure 2.58). The WXT536 is also able to record temperature, pressure, and relative humidity, enabling calculation of air density. When deployed on a river bank the WXT536 needs to be manually aligned with North (i.e. true North). When it was deployed on an ADCP (Figure 2.58) the ADCP compass data was used for orientation (with synchronisation of the ADCP and WXT536 clocks before deployment). We used a sampling frequency of 1 Hz for wind data from the WXT536, but a lower frequency for temperature, pressure, and relative humidity.

For high precision measurements of wind velocity profiles and turbulence, we also deployed a wind tower (Figure 2.59) consisting of 3x Campbell Scientific CSAT3B sonic anemometers (in conjunction with our partner Crown Research Institute ‘Scion’). This wind tower was deployed for 28 days (Figure 2.60), with the CSAT3B sonic anemometers logging at 50 Hz, in a range of wind conditions. This data was collected to estimate wind shear stress on the water surface, and its effect on velocity profiles. Although such precise equipment as a wind tower consisting of CSAT3B sonic anemometers is beyond the scope of routine monitoring, it is very useful for investigating the physics underpinning the effect of wind on surface velocities (and thus ‘alpha’).



Figure 2.57: Left: Basic handheld anemometer (ProTech QM1646) for characterising wind conditions during surface velocity measurements; Right: Vaisala WXT536 climate station for 2D measurements of wind velocities, with complementary measurements of temperature, pressure, and relative humidity.



Figure 2.58: NIWA field technicians Alec Dempster and Hamish Sutton deploy a River Pro ADCP and Vaisala WXT536 in a hydropower canal in New Zealand for measurements of the effect of wind on velocity profiles and surface velocities.

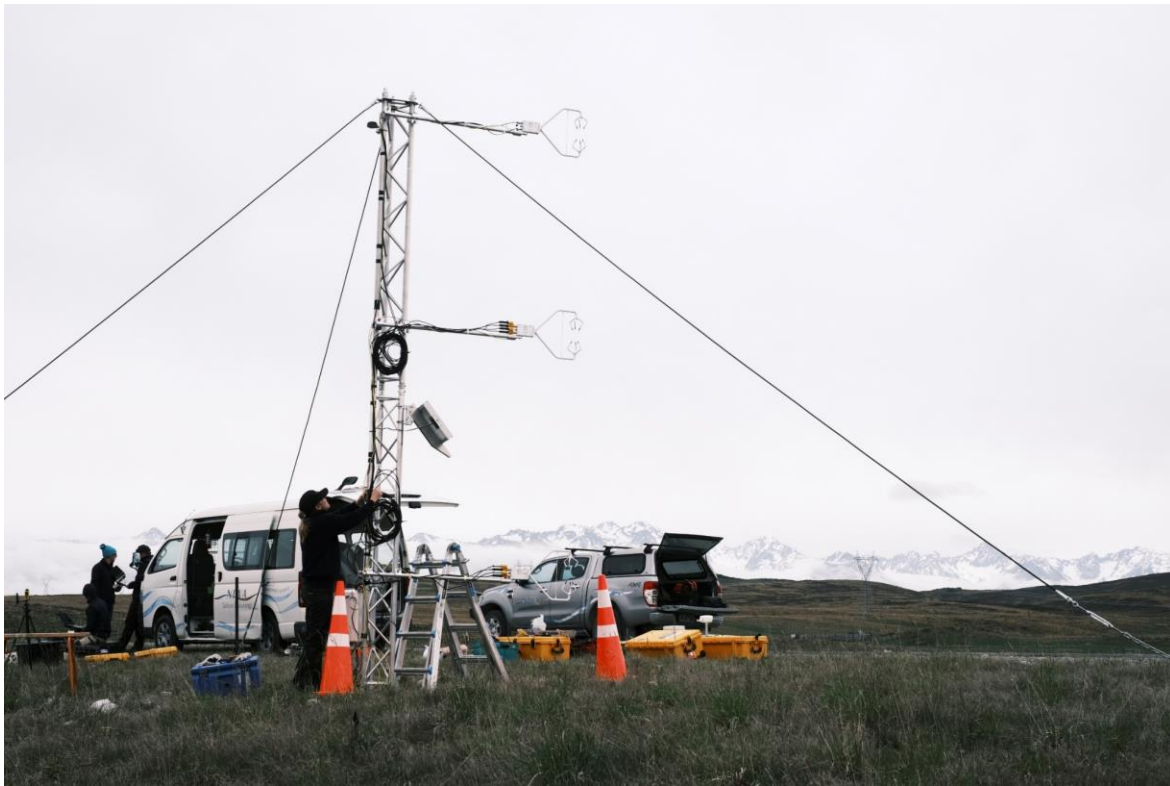


Figure 2.59: Wind tower deployed at the Tekapo Canal for long duration measurements of wind velocity profiles and turbulence, using 3x CSAT3B sonic anemometers.

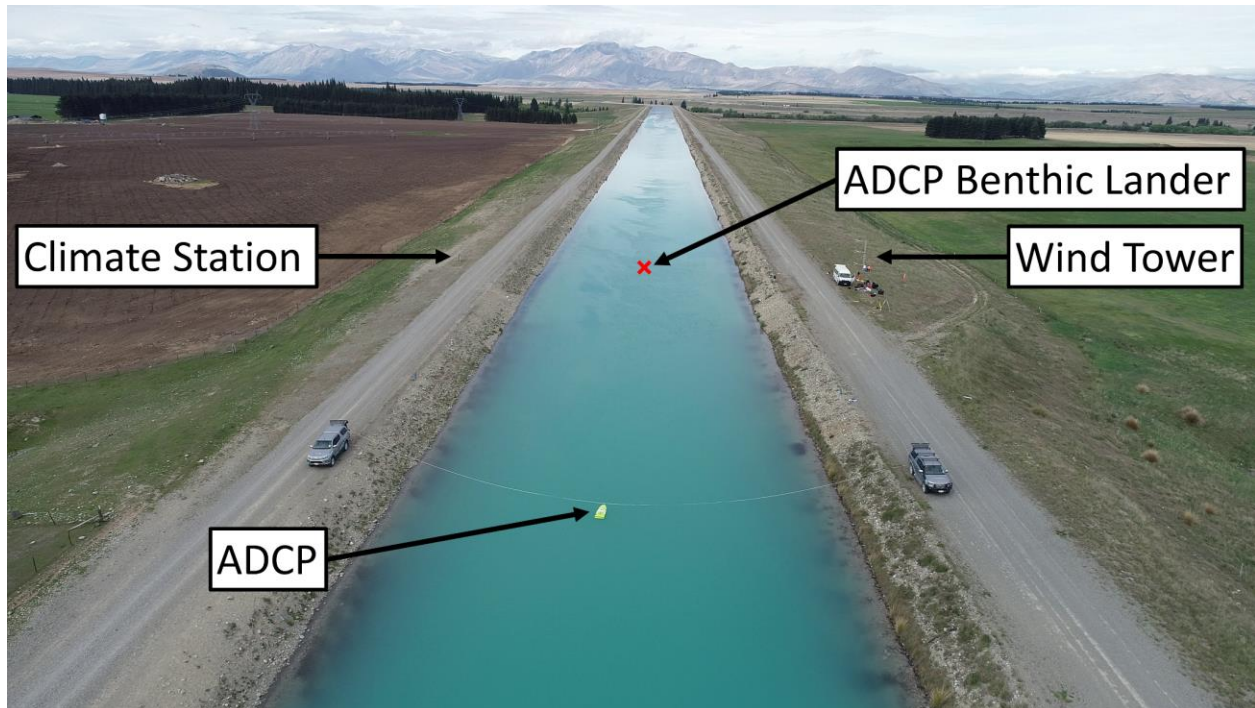


Figure 2.60: Deployment of the Wind Tower (3x CSAT3B) and Climate Station (WXT536) for long term measurements of wind velocity profiles and turbulence in the Tekapo Canal. The WXT536 provided the complementary data required to calculate air density from temperature, pressure, and relative humidity.

## 2.5.6 Mark Forged X7 3D printer

During the ‘drone flow’ project, a large number of custom parts were designed in Autodesk Inventor and Solidworks (e.g. tracer particle distribution system components, stereoscopic camera components, and numerous mounting brackets). Most parts were 3D printed on a Mark Forged X7 3D printer (Figure 2.61), with continuous carbon fibre deposition where required (e.g. for parts requiring high stiffness). Overall, the quality of parts from this machine were excellent, as was the ease of use of the print software/interface. NIWA acquired an ex-demo machine (they are not cheap new) since we were sending a high volume of parts externally for printing. Having the machine in house dramatically shortened turnaround times between design and fabrication, which was particularly advantageous for rapid prototyping and design iteration (if required). Whether an in house (or external) machine is used, we would highly recommend this 3D printer to others. The dimensional accuracy, structural integrity (stiffness) and overall quality of the output parts dramatically outperformed that from hobbyist machines when printing the same parts. It also enabled rapid prototyping of components that were then sent externally for more expensive and time-consuming fabrication from aluminium (or similar).

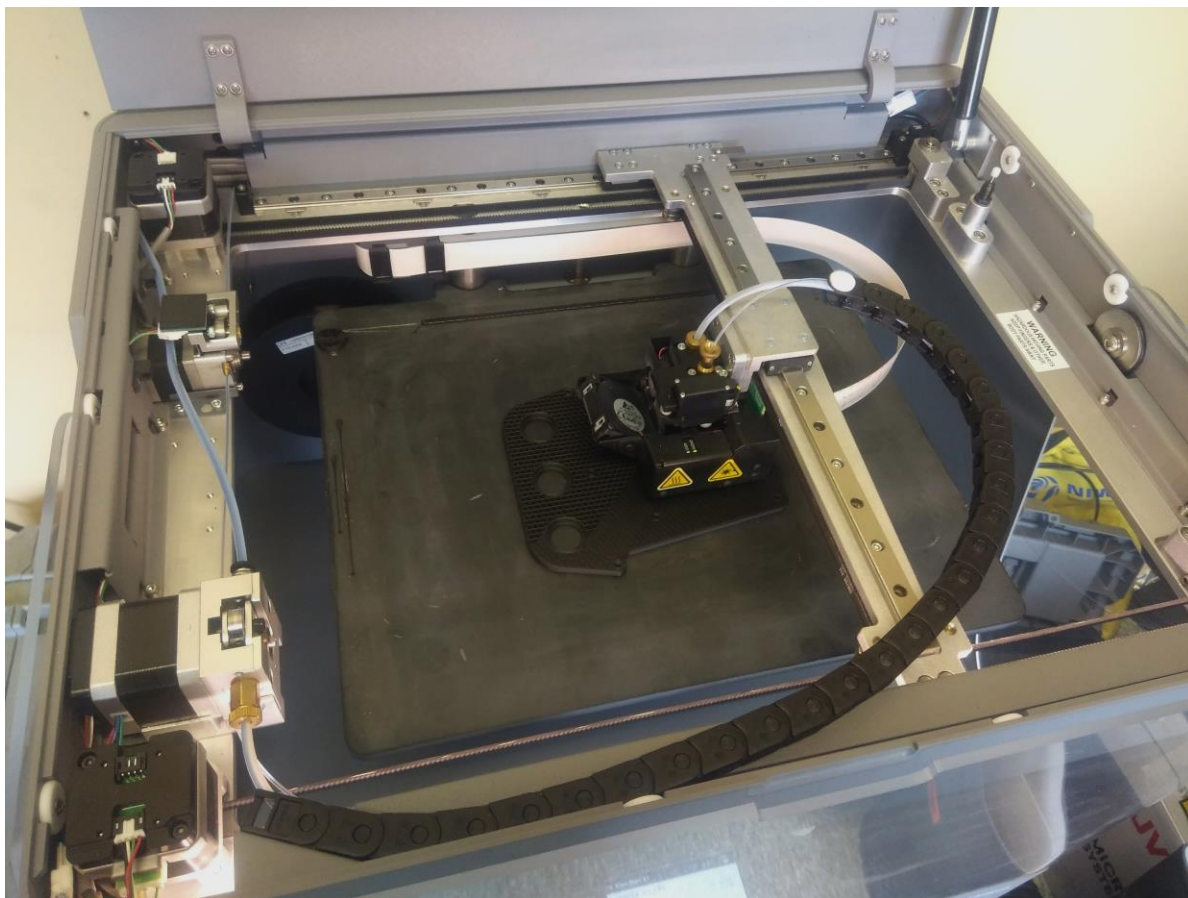


Figure 2.61: Mark Forged X7 3D printer producing an end plate for the tracer particle distribution system.

## 2.5.7 Miscellaneous

### Thermal infrared cameras:

Thermal infrared cameras have a wide range of applications in riverine remote sensing (e.g. Faux *et al.*, 2001; Handcock *et al.*, 2012; Dugdale, 2016). Examples are their use for surface velocimetry (Puleo *et al.*, 2012; Legleiter *et al.*, 2017; Kinzel & Legleiter, 2019; Schweitzer & Cowen, 2021) and investigation

of spatial and temporal thermal heterogeneity (Wawrzyniak *et al.*, 2013). Inclusion of a thermal infrared band may also improve the accuracy of river environmental classification, such as those obtained using Convolutional Neural Networks (CNN) (Carboneau *et al.*, 2020). The ‘drone flow’ project was interested in thermal infrared remote sensing for two main purposes: (1) automatic delineation of river boundaries for classification of river wetted area (and mask creation); (2) thermal infrared for LSPIV with temperature differences as tracers.

For this purpose, multiple consumer grade thermal infrared cameras were borrowed and tested. These were the DJI XT2 and FLIR T1010. However, severe hardware faults in the XT2 resulted in it being swapped for a DJI XTR. Both DJI cameras performed very poorly and did not produce thermal imagery suitable for scientific use. The XTR was suitable for qualitative identification of relatively hot or cold regions (such as an upwelling region), however the temperature measurements were not stable, nor was the temperature sensitivity suitable for LSPIV. The FLIR T1010 performed better, but was not designed for drone-based operations. After multiple modifications we were able to deploy it on our DJI M600 drone and obtained reasonable imagery of the water surface (suitable for qualitative identification of upwelling zones), however it was unsuitable for LSPIV, or large scale mapping (due to the weight, field of view, and limited control of image acquisition).

Following this testing, thermal infrared remote sensing was ceased as initial results were not promising and it was largely beyond the scope of the project. Relevant findings were:

- Invest in a research grade cooled thermal infrared camera with high thermal sensitivity (e.g. Kinzel & Legleiter, 2019). Ideally cooled photon detector infrared cameras (such as the FLIR SC8340 or SC8303) should be used to capture ‘instantaneous’ thermal distributions (Legleiter *et al.*, 2017; Schweitzer & Cowen, 2021), rather than microbolometer cameras.
- Perform deployments at dawn, before the sun unevenly warms the landscape, or there are thermal infrared reflections.
- To look for groundwater inputs, perform deployments when ground water is warmer than surface water (e.g. winter in New Zealand), so that it will rise to the surface due to lower density. This is particularly relevant at dawn when surface water has cooled overnight.
- Raw thermal imagery data for DJI cameras can be extracted from the EXIF information attached to the radiometric jpg image. This can be performed using the function 'getExifData.m' in the ‘drone flow’ toolbox (Appendix A).
- Aluminium baking trays are effective as thermal GCPs (Section 2.4.1).
- Temperature probes are effective for ground truth temperature measurements, with measurement locations surveyed with RTK GPS. Again, care must be taken that surface and subsurface temperatures match (i.e. at dawn).
- The wide range of emissivity of materials found in river environments (i.e. different rock types)<sup>11</sup> are likely to create issues for remote sensing of absolute temperature. However, this may also provide opportunities for improving automatic classifications of rock lithology in braided rivers. For example, if dry rocks across a riverbed are at the same ‘absolute temperature’ (i.e. at dawn) but thermal infrared orthomosaics are showing them at different ‘apparent temperatures’ then this indicates differences in emissivity. When combined with other sources of remote sensing data (e.g. RGB or multispectral orthomosaics), then this thermal infrared data (and associated differences) may provide a useful additional imagery band to improve the accuracy of automatic classifications.

<sup>11</sup> [https://www.engineeringtoolbox.com/emissivity-coefficients-d\\_447.html](https://www.engineeringtoolbox.com/emissivity-coefficients-d_447.html)

## **3 Mission planning**

### **3.1 Site selection**

Site selection for surface velocimetry and aerial surveying is an important aspect of mission planning. Selected sites need to be practical for drone operations, with consideration given to airspace restrictions, land ownership/administration and overflying members of the public (see Section 3.2). Sites should have safe takeoff and landing zones, and care should be taken with overhead powerlines, bridges, and dense riparian vegetation. Sites should have open spaces to place ground control points (for aerial surveys) and the drone operator must be able to keep the aircraft within visual line of sight during the flight. Finding suitable monitoring sites is usually straightforward for braided gravel bed rivers but can become problematic for rivers in densely populated areas. Extreme caution must be exercised when performing flights during large floods to find safe locations from which the pilot can observe the drone, as undercut channel banks may collapse without warning.

### **3.2 CAA regulations**

The Civil Aviation Authority (CAA) are the governing body for aircraft and drone regulations in New Zealand. Drones must be operated by competent pilots who have been well trained (ideally to CAA level 102) and are familiar with CAA regulations <https://www.caa.govt.nz/rules/rule-part/show/101>. Examples of important restrictions for ‘drone flow’ operations are:

- Not to fly higher than 120 metres above ground level.
- Not to fly within restricted airspace.
- Not to fly above people without their consent (such as members of the public).
- Not to fly over land without the consent of the property owner or administrator.
- To keep the aircraft within visual line of sight at all times.

Information on airspace restrictions can be found on <https://www.airshare.co.nz/maps> and it is prudent to log all flights on the airshare website. It is recommended that organisations undertaking aerial surveying and surface velocimetry implement an internal mission planning system, where flight plans are reviewed and approved by a nominated chief pilot (particularly for new deployment sites). This provides an extra layer of oversight that safe operating practices will be followed, and flights comply with CAA regulations.

### **3.3 Deployment conditions**

Weather conditions, lighting and river clarity can be critical for the success of aerial monitoring and surface velocimetry missions (depending on the objective of the deployment). For bathymetry from through-water imagery corrected for surface refraction it is important for the riverbed to be well illuminated, but to minimise reflections off the water surface. In our experience the optimal deployment conditions for collecting through water imagery in New Zealand is to perform flights close to solar noon, with no cloud cover and minimal wind (Biggs, 2020). Reflections of the sun off the water surface (sunglint) is dependent on the angle of the sun, angle of the water surface and field of view of the camera. Sunglint due to specular reflection is more problematic at latitudes closer to the equator where the sun is directly overhead. By recording aerial imagery with sufficient overlap and processing it with structure from motion software (e.g. Agisoft Metashape), sunglint and other transient phenomena that are not fixed in space are usually filtered out. For aerial surveys to generate georeferenced orthomosaics and terrestrial DEMs imagery overlap of 80% front and 60% side are recommended. For bathymetry from through water imagery corrected for surface refraction it is prudent to record imagery above the channel with

even higher overlap (e.g. ideally 90% front and 90% side overlap). If problems with sunglint still occur, then survey time of day, camera angle and flight direction should be adjusted (Overstreet and Legleiter, 2017), however, this can provide a trade-off with illumination of the bed. In our experience, reflections of low altitude clouds pose a more serious problem than sunglint to the visibility of the riverbed in through-water aerial imagery. This is because clouds provide a diffuse source of sunlight, where light rays from all angles are reflected off the water surface back to the camera (Biggs, 2020).

Turbidity is an important factor for multiple bathymetry estimation techniques. If water is too turbid then the riverbed will not be visible for through water imagery corrected for surface refraction (which is usually only suitable for shallow water bathymetry). Likewise, if water is too turbid then bathymetry from colour will also fail in deeper regions due to signal saturation. Bathymetric LiDAR will also fail if water is too turbid, since the maximum resolved depth is ~1-2 secchi depths (Section 4.7.8).

Wind is another critical factor for deployment conditions, both from a practical perspective for drone flights (e.g. aerial surveying), and due to the effect of wind on the water's surface (e.g. surface waves and modified surface velocities). The effects of wind on the water surface are complicated, as the surface waves generated can also cause problems with refraction at the air water interface (i.e. for bathymetry from through-water imagery corrected for surface refraction). They can also cause specular reflections off the waves themselves, causing problems for surface velocimetry due to moving ‘brightness’ noise in the imagery. The use of coloured tracer particles and thresholding techniques can help to mitigate this problem (see Sections 2.3.2 and 2.3.3).

### 3.4 Ground control points and surveying

GCPs (if used) should be placed at locations where they are easily visible in aerial imagery (i.e. away from trees and bushes). At least 10 GCPs should be used (Agisoft, 2022), however the number of GCPs required depends on the size of the reach, with larger reaches requiring more GCPs. For surveys requiring highly accurate orthomosaics, more than 15 GCPs should be used, and spread throughout the reach, ideally with a stratified random distribution (Martínez-Carricando *et al.*, 2018). GCPs must be placed before flights commence and should be secured with rocks to avoid movement by wind gusts. GCPs can be surveyed at any time during the deployment, but it is prudent to survey them as soon as possible following flights to ensure they are not accidentally moved by a member of the public or the wind. For repeated surveys (or surface velocimetry measurements) at a site, fixed GCPs in the form of coloured wooden pegs (or similar) can be installed and only need to be surveyed once.

### 3.5 Flight planning

Flight planning for each mission will depend on the deployment location and data required (see individual methods in Section 4). General tips are:

- For aerial surveys in windy conditions, start flying upwind and zigzag downwind. This enables a safe return to home if wind speeds increase, or batteries get low.
- Return to home when the battery is below 35–40% and land with at least 30% remaining. This is important for LiPo battery life and equipment safety.
- Use a spotter to keep a look out for aircraft and members of public etc. Members of the field team may also carry walkie talkie radios if they are scattered around the study site.
- Members of the field team should leave the river when the drone is overhead, so they do not obscure aerial imagery.

- For large surveys, bring generators for battery charging and pick landing sites along the study reach for battery swapping.
- Bring a rolled-up carpet (or similar) for landing on rough/uneven terrain.
- Launching (and particularly landing) in windy conditions can be risky for drones tipping over and breaking propellers. This is particularly true when they are at partial throttle, as the spinning blades create more wind resistance, but there is less weight force holding them down. Try to select launch/landing sites shielded from the wind (e.g. behind a stand of trees, or a vehicle).
- Plan flight paths so that the drone is always within visual line of sight. Always ensure flights are within CAA regulations (Section 3.2), log flight plans, check Notices to Airmen (NOTAMs).
- Always check aerial imagery on a computer before leaving a study site (i.e. imagery not blurry, full site coverage, minimal sunglint in surface velocimetry videos etc) and transfer it to the computer hard drive as a back-up.

## 4 ‘Drone flow’ measurement methods

### 4.1 Surface velocities (nadir from a drone)

Nadir (i.e. downlooking) aerial imagery is very convenient for resolving surface velocities. This imagery usually only needs stabilisation and scaling (when a rectilinear lens is used). If a non-rectilinear lens is used, then lens distortion will also need to be corrected. For surface velocimetry it is recommended to record videos with at least 5 minutes of tracer motion. These videos can then be cropped to a shorter duration (i.e. 1 minute) where there is good tracer coverage. Altitude should be selected to provide suitable resolution to resolve tracers (which will depend on the size of tracers used). The ‘Camera and flight parameter calculator’ (Appendix E) can be modified to include the resolution and field of view of the camera/video to calculate the video footprint and pixel resolution (i.e. ground sample distance)<sup>12</sup>. For channels without sufficient natural tracers such as foam, debris, or surface features, then it may be necessary to add artificial tracer particles. These can be added from an upstream bridge or boat (Detert *et al.*, 2017; Detert *et al.*, 2019a), or distributed with an aerial tracer particle distribution system (Figure 4.1), see Section 2.3.4. Tracer particles can also be dyed and thresholding techniques applied to reduce environmental noise (Biggs *et al.*, 2022a), see Sections 2.3.2 and 2.3.3. Nadir aerial imagery for surface velocities should have fixed reference points visible in the imagery that don’t move. This is usually achieved by the aerial imagery having some overlap with channel banks, or a downstream bridge.



Figure 4.1: Aerial tracer particle distribution system in the Rangitata River, New Zealand.

It is recommended to select measurement sites where the flow is well developed (ideally with logarithmic velocity profiles) and is not highly three dimensional. For example, measurement sites should generally be upstream from bridges, rather than downstream, to avoid wakes from bridge piers which cause complex three dimensional flow and turbulence, reducing the accuracy of relationships between surface velocities and depth averaged velocities (i.e. alpha), see Section 4.8. Scour and deposition downstream from bridges can also make cross sections more spatially heterogeneous, enhancing errors in discharge calculations if there is any misalignment between the georeferenced locations of surface velocities and cross sections. Likewise, channels with other sources of complex instream flow resistance such as aquatic vegetation (Biggs *et al.*, 2019) should generally be avoided, or the higher uncertainty indicated with Quality Control (QC) codes.

<sup>12</sup> Please note that a video may have a different field of view than a full frame image from a camera and should be added to the calculator separately.

Once suitable nadir aerial imagery is recorded, it needs to be stabilised, scaled, and processed to resolve surface velocities. There are multiple different software packages and processing algorithms available for this purpose (see Section 1.2). The selection of an appropriate algorithm will depend on the purpose of the data and the density of tracer particles available. Large Scale Particle Image Velocimetry (LSPIV) requires a high density of tracer particles, but produces 2D velocity distributions (both instantaneous and time averaged), which can be used for resolving surface turbulence. Whereas, Space Time Image Velocimetry (STIV) is suitable for a low density of tracer particles, but only produces a 1D time averaged velocity that is orthogonal to a cross stream search line. For routine discharge gauging applications STIV is usually the most convenient (Figure 4.2), and least influenced by environmental noise. The most commonly used software packages for data processing are: Fudaa-LSPIV, Hydro-STIV, RIVeR, and RIVeR-STIV. For detailed information on data processing please consult the appropriate user manual (e.g. Jodeau *et al.*, 2020; Hydro Technology Institute, 2022), publications (e.g. Patalano *et al.*, 2017), and tutorials<sup>13</sup> for the software being used.



Figure 4.2: Surface velocities in the Hurunui River from STIV, processed with Hydro-STIV.

In most cases it is possible (and advantageous) to capture the full channel width in each video frame, with a nadir (i.e. down looking) camera angle. However, there are cases where this is not possible, such as in wide channels, or during floods. In these cases oblique aerial imagery (Section 4.3), or sections of nadir imagery should be used (Section 4.4). There can also be situations where full channel width nadir surface velocimetry measurements are not the best option due to sunglint. This is more likely if cross sections happen to be North-South oriented and surface velocity measurements are occurring at solar noon. If this is the case, then oblique aerial imagery from the side of the channel where the sun is behind the camera may be superior (Section 4.3), or multiple overlapping nadir surface velocimetry sections can be used (Section 4.4).

<sup>13</sup> <https://riverdischarge.blogspot.com/p/tutorials.html>

## 4.2 Surface velocities (oblique from riverbanks)

Oblique imagery is mainly used from riverbanks for fixed camera flow measurement stations (Le Coz *et al.*, 2010), or obtaining hydrological data from citizens (particularly after flood events) (Le Coz *et al.*, 2016). Oblique imagery should be collected with the sun coming from behind the camera to minimise sunglint<sup>14</sup>. Oblique imagery is also stabilised and processed using software such as Hydro-STIV, Fudaa-LSPIV, RIVeR, RIVeR-STIV, or MATLAB, however oblique imagery needs to be orthorectified using ground control points. GCPs are typically placed on both sides of the channel (Section 2.4.2) and surveyed with RTK GPS (Section 2.4.1). For a full 3D orthorectification (i.e. perspective projection in Hydro-STIV) six or more GCPs are needed, as well as the water level. For a 2D orthorectification (i.e. homography transformation in Hydro-STIV) four or more GCPs are needed, which are situated at the water's edge (i.e. water level). It is recommended to use more GCPs than are strictly needed to improve orthorectification accuracy, and to enable assessment of orthorectification accuracy (if needed). After orthorectification surface velocities are calculated as they were in Section 4.1.

For high resolution orthorectified imagery, it is recommended to use a high camera angle relative to the water surface (e.g. from a high riverbank, or a camera mast/tower) (Figure 4.3). It is also possible to collect oblique imagery from drones, rather than nadir imagery. This can be useful for very wide rivers (i.e. floods), or to position the drone so that the sun is coming from behind it to reduce surface reflections. More information on collection of oblique imagery from drones and strategies for using drones to survey in GCPs during large floods is found in Section 4.3. Alternatively, sections of nadir drone imagery can be used for wide rivers (see Section 4.4).

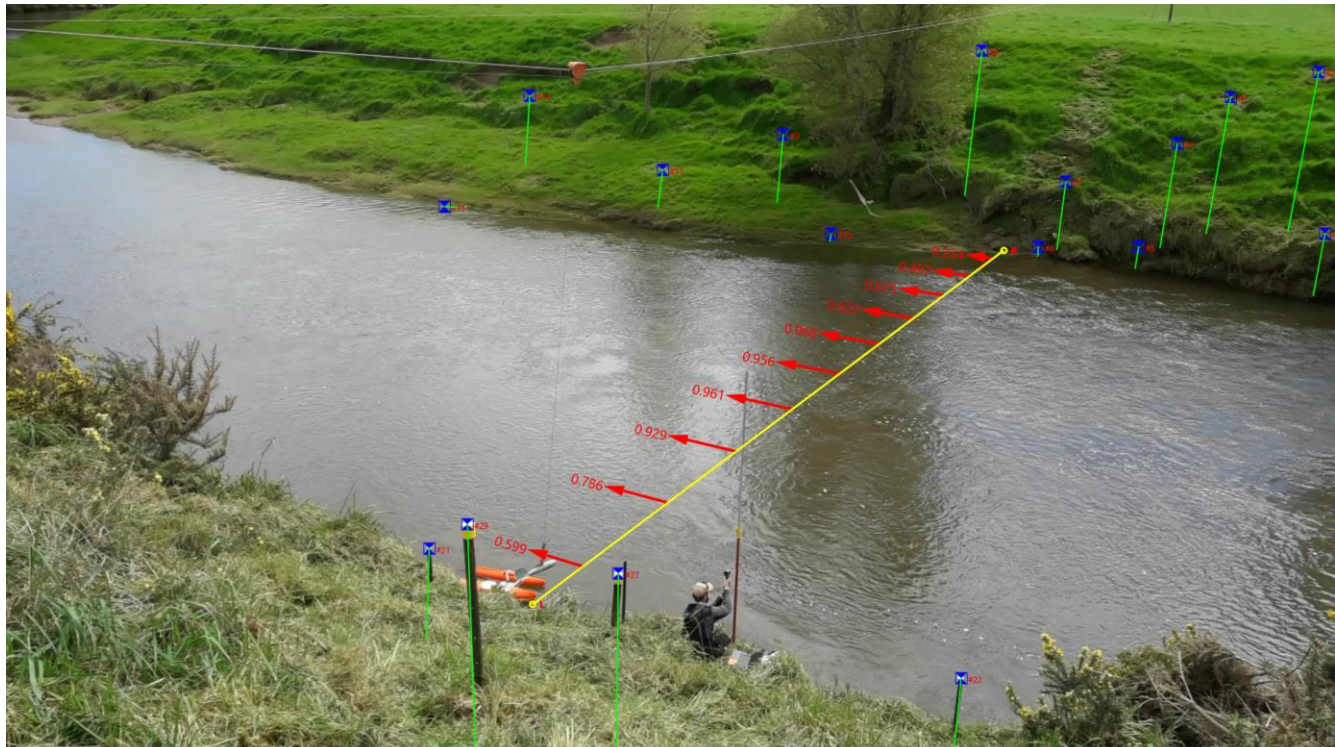


Figure 4.3: Surface velocities and GCPs in the Makarewa River at a fixed camera gauging site developed by Michael McDonald from Environment Southland during collaboration on the ‘drone flow’ project.

<sup>14</sup> This is an important consideration when planning fixed camera flow measurement stations.

### Future recommendations:

The development and deployment of stereoscopic camera stations for recording oblique imagery from riverbanks for surface velocimetry is recommended. These could be calibrated mobile systems (Section 2.1.2), or fixed camera stations (Ran *et al.*, 2016; Li *et al.*, 2019). Stereoscopic imagery enables water surface geometry/elevation to be evaluated and imagery to be orthorectified without needing GCPs. For shallow dry channels subject to flash floods (i.e. mountain streams) cross sections can even be remotely surveyed from the stereoscopic imagery and reconstructed points. Doing this before and after floods could improve the accuracy of flow measurements during the flood, by providing better estimates of the cross section (i.e. mean cross section during the flood). If these systems are coupled with measurements of water level (i.e. stage), then they could also be automatically triggered at a range of water levels for constructing a complete rating curve. Water level measurements could be obtained in many ways, but the primary candidates are by using a pressure transducer, or from the stereoscopic camera system itself (if it can be configured to automatically detect, triangulate, and reconstruct water level). With the increasing availability and decreasing cost of high bandwidth telemetry (i.e. internet from space), these systems could be deployed in remote locations, with videos telemetered to management agencies for processing. These videos could then be used to develop rating curves for a site, then real time water level (i.e. stage) measurements and the developed rating curve used for downstream flood warnings in the future. This is likely preferable to real time automated processing of surface velocimetry and cross section data in situ, which is challenging and lacks quality control assessment. Once rating curves are established for sites, these systems could be moved around to establish rating curves at other sites. Overall there is vast potential in this area for future research and development.

### **4.3 Surface velocities (oblique from drones)**

Oblique aerial imagery from drones can capture wider channels than bank based oblique imagery due to higher viewing angles. This aerial imagery will also need to be stabilised and orthorectified with GCPs (see Section 4.2), then processed for surface velocities (see Section 4.1). If logistical constraints prevent the deployment and surveying of GCPs (for example during large floods), then terrestrial features (e.g. trees, bushes, boulders etc) can be used as surrogate GCPs. These surrogate GCPs should be selected as visually distinctive objects on each bank of the channel that are near the water level (for orthorectification). Their approximate GPS coordinates can then be obtained by flying the drone to each of them, then hovering the drone above them, and recording an aerial image of the feature/GCP, with the camera pointing nadir, and the feature/GCP in the centre of the image<sup>15</sup>. For integrated camera gimbal modules (i.e. DJI Phantom 4 Pro) this will generate an image with GPS coordinates stored in the EXIF information of the image file. The GPS coordinates can then be extracted from the EXIF information of the image file and used for 2D orthorectification in Fudaa-LSPIV (homography transformation in Hydro-STIV)<sup>16</sup>. It is also possible (although much riskier) to land beside, or hover close to GCPs (and also the water's surface), then use the altitude data from the EXIF information to generate 3D GCP locations. This would provide sufficient information for 3D orthorectification in Fudaa-LSPIV (perspective projection in Hydro-STIV), however the author does not recommend this due to the high risk of crashing drones. The approach of extracting GPS coordinates from images for surrogate GCPs is lower accuracy than using standard GCPs and surveying them with RTK GPS, however for very wide rivers (such as braided rivers during floods) the relative significance of these errors decreases. Likewise, if a drone with RTK GPS can be used (for example the DJI Phantom 4 Pro RTK) then the accuracy of the locations of these surrogate GCPs increases, as does the accuracy of the orthorectified imagery. This technique can also be used for extracting the width of channels (particularly during floods) for scaling nadir imagery

<sup>15</sup> Credit for this technique to Mark Randall.

<sup>16</sup> It is important that GCPs are at (or very near) water level for 2D transformations.

(again drones with RTK GPS are recommended). MATLAB code (i.e. 'getExifData.m') for extracting EXIF information (e.g. GPS coordinates and altitude) from aerial images is provided in the software toolbox that accompanies this user guide (Appendix A). Some of the EXIF information attached to images is also available by right clicking an image in Windows 'File Explorer', going to 'Properties', then 'Details', however this is usually a small selection of all the available information attached to an image. In general, oblique aerial imagery will usually generate less accurate surface velocities than nadir imagery (particularly at lower inclination viewing angles nearing horizontal). This is due to multiple factors related to the uneven resolution of the orthorectified imagery, where imagery at the far bank of the river has a coarser resolution than that at the near bank. This can create problems with tracer detection, and enhancement of any residual camera vibrations/wobble following stabilisation. In many cases it is better to use nadir aerial imagery, but process surface velocities in sections if the channel is too wide (see below).

#### 4.4 Surface velocities from multiple sections for wide rivers and flood gauging

There are many situations where it is not possible (or optimal) to capture the full channel width in one frame of aerial imagery. Examples are, wide channels, floods, sunglint, or when higher pixel resolution is required to detect tracer particles (necessitating lower flight altitudes). In cases such as these, it may be necessary to divide the channel up into sections and perform multiple surface velocimetry measurements, then combine these measurements together. However, it should be noted that data collection and processing can be significantly more laborious than capturing the full channel width in one frame. To use multiple sections, there will ideally be fixed reference points visible in the imagery. A convenient location to perform these measurements is upstream from a bridge, as the bridge (i.e. bridge piers at water level) can provide convenient reference marks for dividing the imagery (Figure 4.4). The width of the sections can then be manually surveyed, extracted from georeferenced orthomosaics of the site, extracted from google earth (for larger scale sites), or obtained by hovering the drone over reference points and taking nadir photos to obtain GPS coordinates (as described in Section 4.3). Measurements should always occur upstream from bridges (where possible) as flow downstream from bridge piers is highly three dimensional, making it much harder to estimate alpha coefficients. Bathymetry downstream from bridges is also more heterogeneous. In braided gravel bed rivers, it is usually possible to divide the full channel width into sections, with one surface velocimetry section for each braid. For very wide rivers without any fixed reference points, the footprint of image sections (and thus overlapping points for stitching surface velocities) can also be calculated from camera origin, height above the water surface, and field of view, however this is more complicated and usually less accurate (image stabilisation is challenging). For measurements without fixed reference points the use of drones with RTK GPS and fast response (very stable) gimbals is recommended.

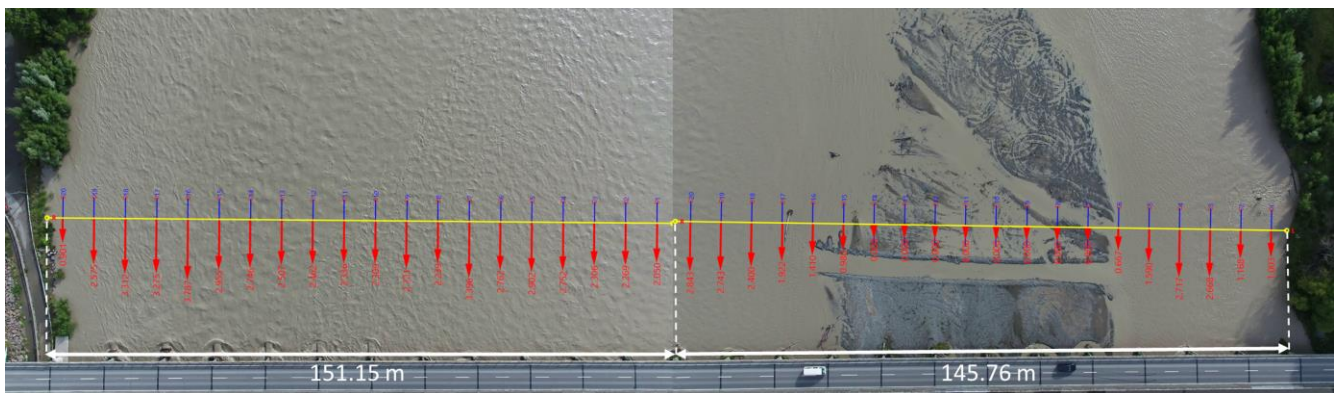


Figure 4.4: Wider channels can be divided into sections for nadir surface velocimetry measurements. Flood flow measurements in the Waimakariri River, New Zealand @  $813.7 \text{ m}^3/\text{s}$ .

## 4.5 Aerial surveys of rivers (terrestrial regions)

Aerial surveying of rivers is an important part of ‘drone flow’ measurements to generate georeferenced orthomosaics, Digital Surface Models (DSMs), and Digital Elevation Models (DEMs). These have many applications, such as physical habitat mapping, quantifying geomorphic change, and estimating grain size distributions. When combined with methods for bathymetry estimation, terrestrial regions can also be merged with wetted regions to create DEMs that are suitable inputs for hydraulic modelling. Georeferenced orthomosaics and DSMs are typically generated using overlapping aerial imagery and Structure from Motion (SfM) photogrammetry techniques (e.g. Westoby *et al.*, 2012; Fonstad *et al.*, 2013; James *et al.*, 2019). DSMs are similar to DEMs, except that they capture the top of visible features that may be above ground level (e.g. vegetation canopies) whereas DEMs capture the underlying terrain at ground level. In deployment applications with a clear view of the ground DSMs and DEMs are equivalent. In regions with vegetation canopies, LiDAR is typically used to generate true DEMs since it will penetrate through sparse vegetation canopies and provide returns from the ground. The following sections provide an overview of both methods.

### 4.5.1 Georeferenced orthomosaics and DSMs

To obtain imagery suitable for generating georeferenced orthomosaics (2D photo maps) and DSMs, a high degree of image overlap is required. Flight paths providing at least 80% front overlap and 60% side overlap are recommended (Agisoft, 2022). Selecting an appropriate altitude for flights is a trade-off between pixel resolution (i.e. ground sample distance) and flight time. For example, halving the aircraft height requires four times longer flights (since images now cover only  $\frac{1}{4}$  of the ground area). Automated flight paths for aerial surveys with drones are created in applications such as: ‘Mission Planner’, ‘DJI Ground Station Pro’, and ‘Map Pilot’. When performing low altitude flights, it is important to check the heights of tall trees near the study site (e.g. poplar trees). This can be achieved with a laser range finder such as a Nikon Forestry Pro (Biggs, 2020). Common sense is required for assessing potential hazards, and survey flights at altitudes of less than 50 m should generally be avoided in heterogeneous terrain (or performed with caution).

To obtain quality aerial imagery, appropriate camera settings are critical. Camera settings for aerial surveying are discussed in detail in Section 2.1.1, but it is reiterated here that a fast shutter speed must be used to avoid blurry images. For RGB cameras, the recommended settings are: shutter priority mode

with 1/1000 shutter (or faster in good lighting conditions); focus set to infinity or auto; aperture set to auto; and ISO set to auto. In poor lighting conditions, or when using cameras with narrow apertures, it may be necessary to use slower shutter speeds (indicated by ISO exceeding 400). In these situations, both shutter speed and flight speed should be reduced. It is recommended to fly slower rather than stopping and hovering at each image capture location. This is because the drone flies much more stably through clean air than when hovering, which causes orientation instabilities that result in more significant blur than those arising from translational motion. For more detailed information on image blur, please refer to Biggs, (2020).

Flight planning with integrated RGB camera-gimbal modules is relatively easy, as the camera hardware parameters are usually pre-loaded into the appropriate software (i.e. in DJI Ground Station Pro there will already be a Phantom 4 Pro camera to select). For other cameras (such as the Sony A5100 that we use for some missions), custom cameras will need to be created in the mission planning software, or the camera will need to be run in time-lapse mode (i.e. standalone), and flight parameters adjusted to provide the required image overlap, flight speed, ground sample distance etc. A camera flight parameter calculator is provided in Appendix E and through the GitHub repository to help with the creation of custom cameras and planning aerial missions with them.

Once fieldwork has been completed, the next step is aerial imagery processing to generate georeferenced orthomosaics (2D photo maps). The images from the survey should be collated and cleaned up before processing. Usually this involves copying all the images to a single folder, removing any images from outside the survey area, and sometimes renumbering the images if there are duplicate image names. Duplicate image names commonly occur for large surveys when the drone has recorded multiple folders of images (i.e. more than 1000 images). Two functions ‘mergeintoFolder.m’ and ‘fixFileNumbering.m’ are provided in the ‘drone flow’ software toolbox (Appendix A) to assist with moving and renumbering files. The imagery is now ready for processing with SfM software such as Agisoft Metashape (Figure 4.5), or Pix4D.

### To process RGB aerial imagery in Agisoft Metashape, the general steps are:

- Add photos.
- Align photos.
- Add markers (i.e. GCPs if they are used).
- Optimise camera alignment.
- Build dense point cloud.
- Build DEM.
- Build orthomosaic.
- Export DEM.
- Export orthomosaic.

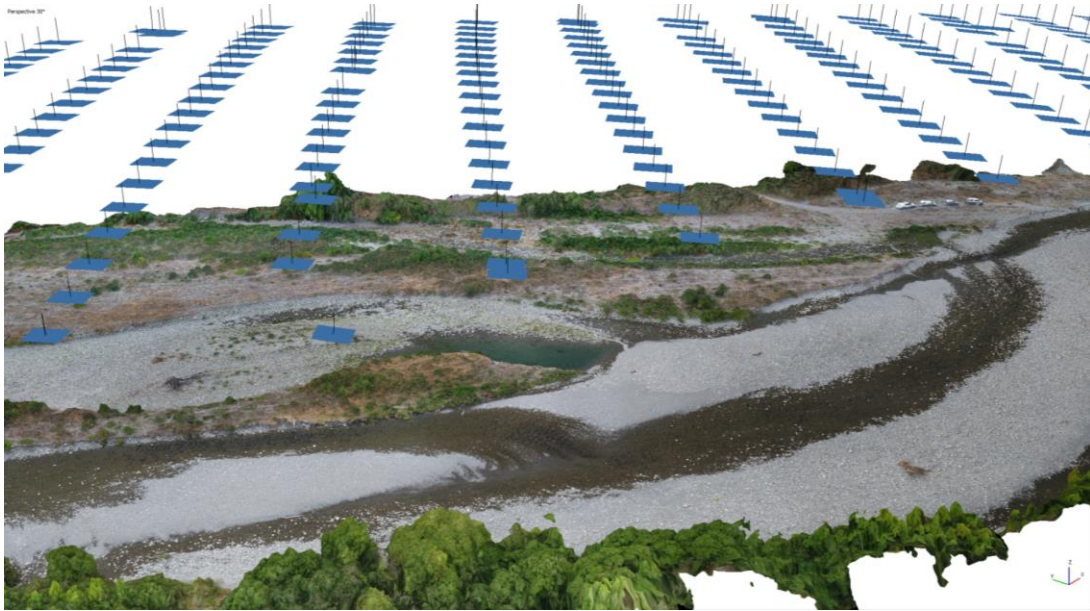


Figure 4.5: Aerial imagery processing with Agisoft Metashape (Waingawa River, New Zealand). Blue rectangles are camera locations.

#### For detailed information on generation of georeferenced orthomosaics and DSMs/DEM<sup>s</sup>, see:

- Agisoft Metashape user manual (Agisoft, 2022).
- Agisoft tutorial: <https://agisoft.freshdesk.com/support/solutions/articles/31000153696>
- Pix4D user manual (Pix4D, 2022).
- ‘Guidelines on the use of structure-from-motion photogrammetry in geomorphic research’ (James *et al.*, 2019).

#### Are ground control points necessary?

The use of GCPs surveyed with RTK GPS will generate more accurately georeferenced orthomosaics and DSMs/DEM<sup>s</sup>; however, there is a significant time penalty for GCP deployment, surveying, and data processing. Recent research indicates that GCPs may not be needed if drones are fitted with RTK GPS for precise data on camera origin (Tomaštík *et al.*, 2019; Štroner *et al.*, 2020). This was not tested by the ‘drone flow’ project, however it provides an enticing prospect (after independent verification and error quantification). This would dramatically reduce field deployment time (and complexity), as well as reducing data processing time. It would also provide significant health and safety benefits, since it would eliminate the need for team members to cross river channels to layout and survey GCPs, which can pose a serious risk in New Zealand’s swift braided rivers.

#### 4.5.2 DEMs with drone mounted LiDAR

To obtain DEMs with penetration through vegetation canopies (i.e. rivers with riparian vegetation, and forests) it can be advantageous to use LiDAR instead of SfM. There are multiple lightweight terrestrial LiDAR units now available that can be flown on drones. NIWA operate a small terrestrial LiDAR unit from LiDAR USA (Figure 4.6) that is deployed on our heavy lift drones such as the DJI M600 Pro, or Aeronavics Skyjib. Following field deployments, LiDAR data can be visualised using software such as Quick Terrain Reader (QTR) or QGIS 3, and processed using software such as LAStools, Cloud Compare, Quick Terrain Modeler, or even MATLAB. In the ‘drone flow’ project we did not need to use the terrestrial LiDAR system extensively as SfM with RGB aerial imagery was suitable for most of our surveying applications.



Figure 4.6: Lightweight terrestrial LiDAR from LiDAR USA (model Snoopy). Provides a convenient way to obtain digital elevation models of river reaches. LiDAR can penetrate through sparse vegetation canopies to resolve underlying terrain features.

#### 4.6 Underwater imagery surveys of clear rivers (wetted regions)

The same SfM methods that can be applied for aerial surveying with drones to generate terrestrial georeferenced orthomosaics and DSMs/DEM<sup>s</sup> are equally applicable to underwater imagery. The procedure is very similar to Section 4.5.1, except that underwater GCPs are now used (Section 2.4.3). They are also surveyed with RTK GPS, and imagery also requires 80% front overlap and 60% side overlap. Imagery can be recorded in time-lapse mode, or as a video with frames extracted after to achieve the required overlap. Basic underwater cameras are effective for this surveying (Section 2.1.4), and cameras with rectilinear lenses should be selected where possible. This method provides exciting opportunities for high resolution underwater surveys (Figure 4.7) and extraction of accurately georeferenced bathymetry (Section 4.7.4).

The main limitations of this method are the need for clear water, and the dependence of spatial coverage on water depth. For example, to achieve the required image overlap, the shallower the water, the closer the surveying lines need to be. Similar to aerial surveying with drones,  $\frac{1}{2}$  the water depth will result in  $\frac{1}{4}$  the image footprint. The field of view of cameras is also reduced underwater due to the higher refractive index of water compared to air. As discussed in Section 2.1.4 the use of a glass bottom boat where the camera is raised above the water surface would significantly help with this problem, as it would create a limit on the minimum image footprint. The issue of depth dependence with underwater cameras (rather than a glass bottom boat) is visible in Figure 4.7 as a hole in the georeferenced orthomosaic on top of a shallow rock where suitable image overlap was not achieved. The use of SfM software such as Agisoft Metashape has made the processing of underwater imagery very easy, since camera calibration parameters are calculated in the step ‘Optimise camera alignment’ which takes into account the reduced field of view of the camera when used underwater.

Although underwater imagery surveys are not likely to be practical for full coverage at the ‘reach scale’, they can be used at multiple locations along a river reach to provide ‘sample areas’ with very high resolution underwater orthomosaics and DEMs. These have many applications such as: benchmarking other depth estimation techniques; underwater grain size analysis (Section 4.9); estimation of periphyton cover, taxonomic composition, and biomass (Biggs *et al.*, 2022b)<sup>17</sup>; and high resolution DEMs for hydraulic modelling (focused on smaller spatial scales).

<sup>17</sup> Multispectral cameras could also be easily used underwater, particularly through a glass bottom boat.



Figure 4.7: Underwater orthomosaic from the Waingawa River, with underwater GCPs comprised of metal washers with holes in them, surveyed in with RTK GPS.

#### 4.7 Bathymetry

Measurement of bathymetry is critical for: river surveying, physical habitat mapping, inputs to hydraulic models, and discharge evaluation. There has been rapid development in the area of remote sensing of bathymetry over the past 10 years (see Section 1.2), with many promising methods available. However, there is not yet a ‘one size fits all’ approach. The application of each method is limited by a range of factors such as: suitable environmental conditions; practicality of deployment and data processing; and cost. This section provides an overview of methods that were applied during the ‘drone flow’ project and introduces other promising methods. Bathymetry estimation is a broad field, and this section is neither

exhaustive, nor highly detailed. Readers should consult Kasvi *et al.*, (2019), Legleiter & Harrison, (2019) and other literature cited within this section for more detailed information.

#### 4.7.1 ADCP – Moving boat cross sections

ADCPs (Section 2.5.1) provide a convenient way to measure bathymetry (Figure 4.8). For surface velocimetry applications, they can be used to measure stable cross sections, or used to re-survey cross sections after floods and geomorphic change. ADCPs can be deployed from bridges, cableways, and taglines (Figure 4.7), or they can be driven manually (i.e. RC boat). They can use stabilisation features, such as a rigid frames (Section 2.5.1) or drogues (Figure 4.8), or they can drift with the current and large eddies. They can use onboard standard depth sounders (Section 2.5.1), or custom narrow beam depth sounders (Sections 2.5.3 and 4.7.3). Cross section bathymetry can be extracted from static verticals using section methods (Section 4.7.2), or it can be extracted from moving boat cross sections (see below).

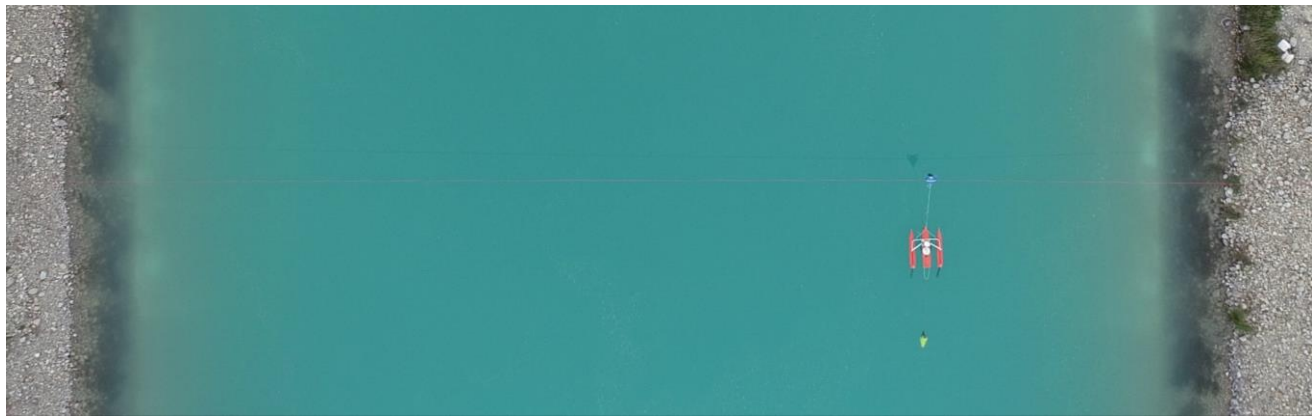


Figure 4.8: ADCP moving boat transects for cross section bathymetry (Tekapo Canal, New Zealand).

To extract accurate cross section bathymetry from moving boat ADCP data, there are a range of challenges to overcome. For example:

- There are two leading brands of ADCPs (i.e. Teledyne RDI and Sontek), both with different data acquisition softwares (i.e. WinRiver II and RiverSurveyor Live).
- Raw data export from these softwares is somewhat cumbersome and time consuming.
- ADCP paths are not straight and must be accounted for, including loops.
- There are multiple distance references available (i.e. GGA, VTG, BT), with drift in displacement estimates between the references.
- Riverbanks must be accounted for.
- Cross section direction must be accounted for.
- Preprocessing data for QA/QC is usually needed (e.g. removing bad transects).

To account for these issues, software for extracting cross sections from moving boat ADCP gaugings was developed by the ‘drone flow’ project and released in the toolbox (Appendix A). This software utilises QRev<sup>18</sup> (or QRevInt<sup>19</sup>) for ADCP data pre-processing, and then extracts relevant data from the .mat file that is saved by QRev. This means that raw data export from WinRiver II or RiverSurveyor Live is not needed.

<sup>18</sup> <https://hydroacoustics.usgs.gov/movingboat/QRev.shtml#Download>

<sup>19</sup> <https://www.genesishydratech.com/qrevint>

The software first plots the individual transect displacements with the available distance references (Figure 4.9: Left). The software then projects the displacement (solid lines) onto the transect (dashed lines) in Figure 4.9: Left. It then sorts the depth data by linear displacement and resamples it with linear interpolation (Figure 4.9: Right). This accounts for the boat path and will remove any loops in the data.

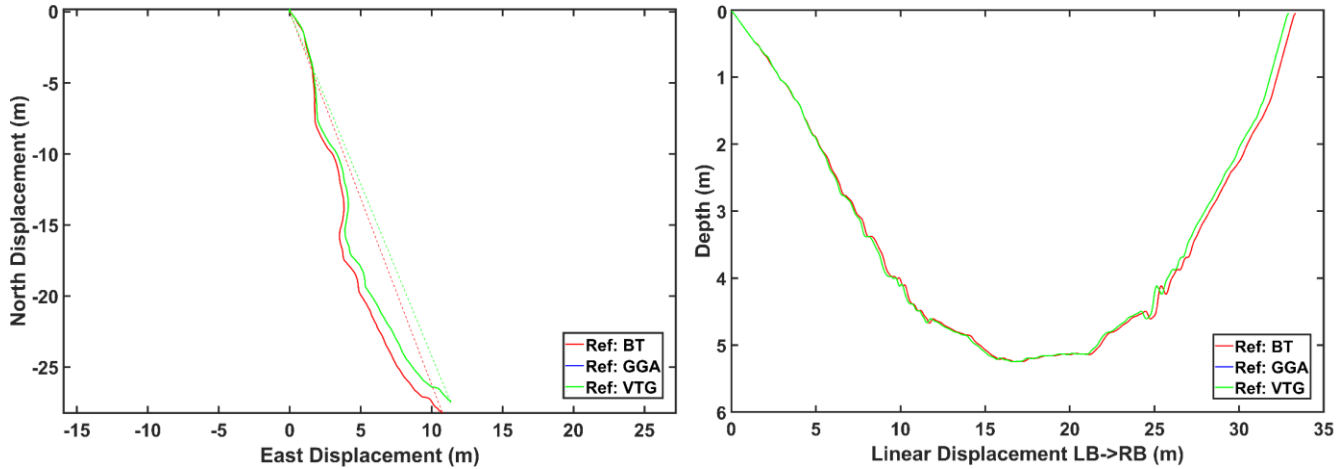


Figure 4.9: Left: ADCP displacement during a transect. Right: Cross section after vector projection of North/East displacement onto cross section unit vector, and resampling (linear interpolation) of depth.

After plotting depth vs linear displacement (Figure 4.9: Right), any differences between the distance references will become visible (i.e. drift/divergence). The next step is to select which distance reference to use, or to manually enter the cross section width. Manual cross section widths are useful if the cross section width has been measured accurately (i.e. surveyed with RTK GPS), or if the ADCP has tracked a diagonal path across the channel (creating a longer cross section than one orthogonal to the banks).

When choosing a distance reference, it is important to understand that although the established methods generally perform well, there is no ‘perfect solution’ and limitations should be understood (Wagner & Mueller, 2011; Rehmel, 2013; Fountain, 2021). For example:

- GPS – NMEA GGA (National Marine Electronics Association - Global Positioning System Fix Data) is susceptible to multipath errors (particularly near banks) and requires differential correction for acceptable accuracy.
- GPS – NMEA VTG (National Marine Electronics Association - Track made good and ground speed) is less accurate at slow boat speeds (cumulative errors). However, it does not require differential correction and is less susceptible to multipath errors.
- BT (Bottom track) doesn’t work for moving bed conditions.
- GPS – RTK (Real Time Kinematic) requires specialist equipment and setup.

Typically VTG or BT are used in New Zealand, since differential GPS corrections with SBAS (Satellite Based Augmentation System) are not yet available<sup>20</sup>. Once the distance reference has been selected, all of the available linear displacement measurements will be rescaled to this distance reference to remove cumulative drift in the measurements (Figure 4.10: Left). Next, the user can elect to use the selected distance reference transect width (Figure 4.10: Left), or they can manually enter transect width if it has

<sup>20</sup> It is currently being developed and will be known as SouthPAN (Southern Positioning Augmentation Network) <https://www.linz.govt.nz/data/geodetic-services/satellite-based-augmentation-system>

been accurately measured. Finally, all of the transects are overlain (Figure 4.10: Right), then the user can select which transects to be included in the final output (i.e. to remove any outliers), with the select transects then averaged and exported as a .csv file.

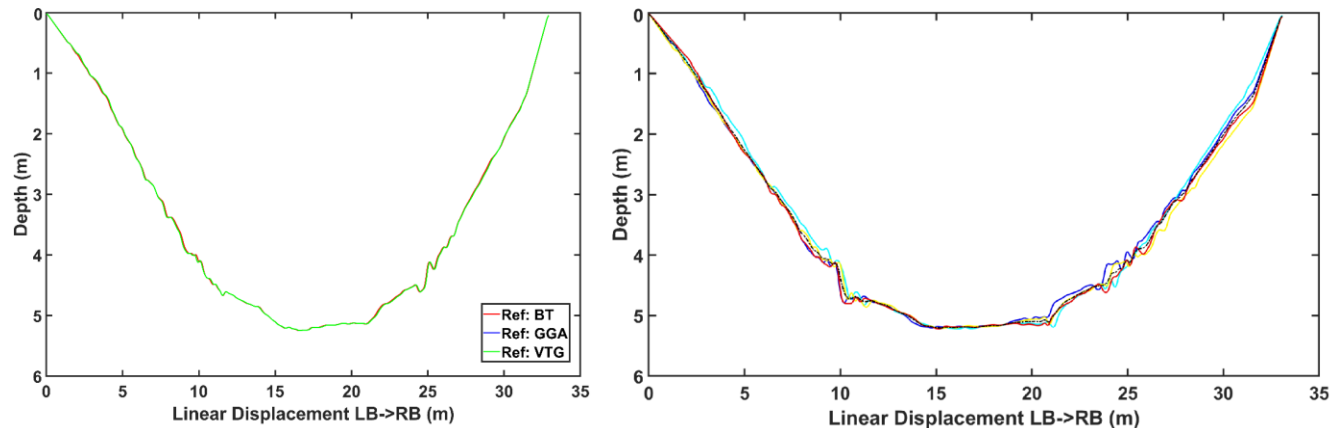


Figure 4.10: Left: Rescaling of linear displacement to account for drift in distance sources. Width can be manually measured and entered, or an ADCP distance source can be used (VTG in this case). Right: Multiple transects are overlaid, then averaged to improve the accuracy of the result (black dashed line) and exported as a .csv file. Example data from the Tekapo Canal in New Zealand.

#### **Advantages of this approach:**

- Bad transects can be filtered out (unchecked in QRev), or by comparison with other transects to remove outliers (Figure 4.10: Right).
- Channel width can be manually entered if needed, or comes from the average projected width of the selected transects for the selected distance reference.
- Multiple transects are averaged, which increases the accuracy of output data.

See Appendix C for detailed instructions how to use the released software and apply this method. The released software has been tested with QRev 4.29 and QRevInt 1.18, but should also work with most older versions too.

#### **4.7.2        ADCP – Section-by-Section (SxS Pro)**

Bathymetric cross sections can also be obtained from ADCPs by doing a section-by section gauging. For Teledyne RDI ADCPs this is performed in the software SxS Pro. With this approach the ADCP is manually positioned at regular intervals across the cross section (e.g. 20-30 verticals). The ADCP records a velocity profile and depth at each location, from which mean velocities and discharge are computed. This is a common method for ADCP flood gauging when there are mobile bed conditions. This is also a very convenient way to obtain a cross section for use with surface velocity measurements, as it is provided in the output gauging summary file. The main downside is that the ADCP displacement is manually reference to the bank, which can introduce minor errors due to any stretch or sag in tape measures/tag lines (if not accounted for), or downstream drift of the ADCP from a perpendicular cross section line. Alternative ways to measure displacement from the bank (such as with a laser range finder) can help to avoid/reduce these uncertainties.

#### 4.7.3 ADCP – Depth sounder and RTK GPS

Narrow beam depth sounders coupled with RTK GPS provide an effective way to accurately map river bathymetry and cross sections. During the ‘drone flow’ project we used a Tritech PA500 depth sounder and a Trimble R10 RTK GPS Rover (Section 2.5.3). MATLAB code for processing data is provided through the GitHub repository (Appendix A) with the script ‘CrossSectionsFromRTKGPSBathy.m’.

**To use this code, the data processing steps are:**

- Pre-process depth sounder data by adding the transducer depth.
- Pre-process near bank regions that were manually surveyed with the RTK GPS survey staff and rover, by subtracting bed elevation from water surface elevation to obtain depth.
- Create a new .csv file for all the depth and RTK GPS data, with the following columns and header {Name,Easting\_m,Northing\_m,CorrectedDepth\_m}.
- Copy the depth sounder data and manual surveying data into the .csv file.
  - The first data record should correspond to ‘Bank 1’, while the last should correspond to ‘Bank 2’. These define the cross-section unit vector and cross section extent. Depth should be approximately zero here.
  - Manually find these bank points and rearrange the order if needed, then save the .csv file.
- Run ‘CrossSectionsFromRTKGPSBathy.m’.

**The provided MATLAB script then:**

- Loads the data.
- Projects it onto the cross-section unit vector (Figure 4.11).
- Removes any data beyond the limits defined by the ‘Bank 1’ and ‘Bank 2’ locations.
- Takes user input as to which bank is the ‘True Left’.
- Interpolates and smooths the depth data (Figure 4.12).
- Exports the cross-section data as .csv files of cross stream displacement (true left bank to true right bank) with separate files provided for ‘Depth’ and ‘Elevation’.

These exported .csv files of cross-section bathymetry can then be easily used for discharge calculations and other applications.

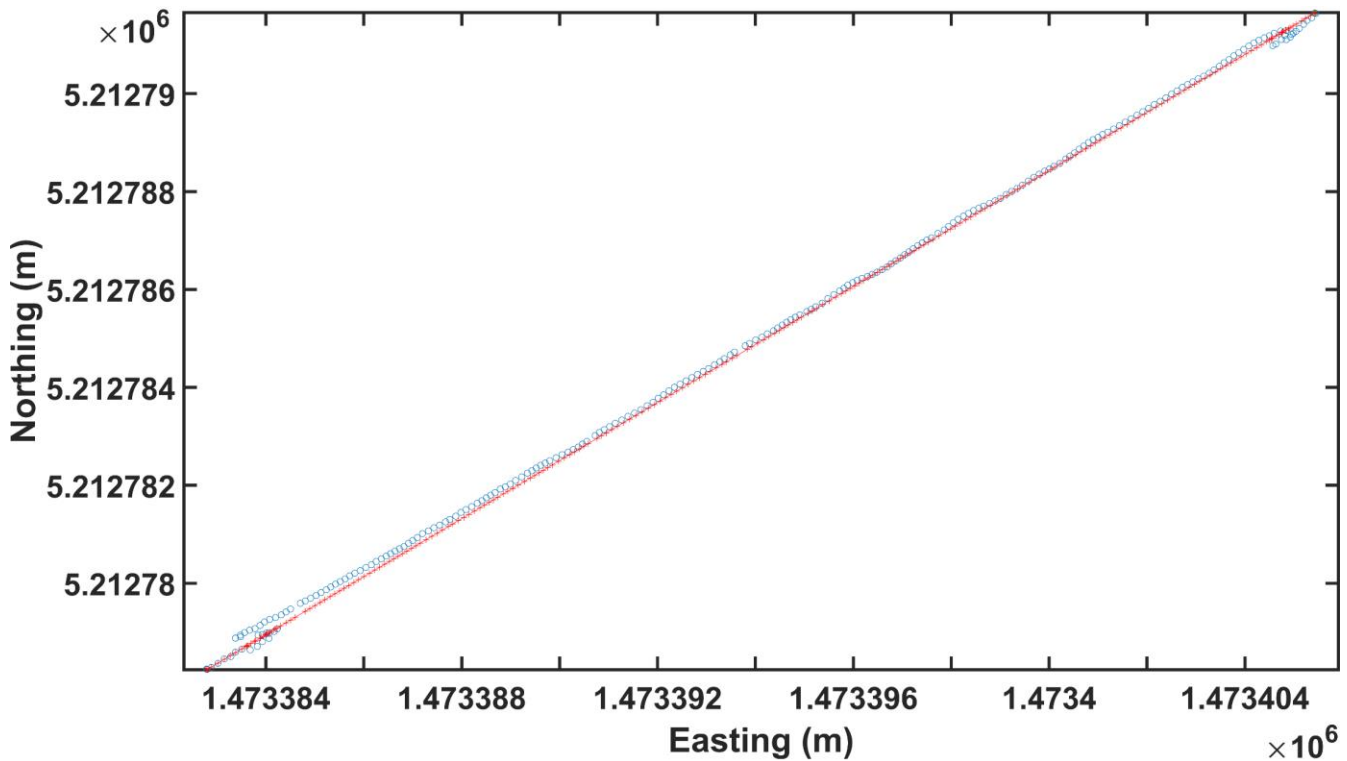


Figure 4.11: RTK GPS measurement points are projected onto the cross section unit vector.

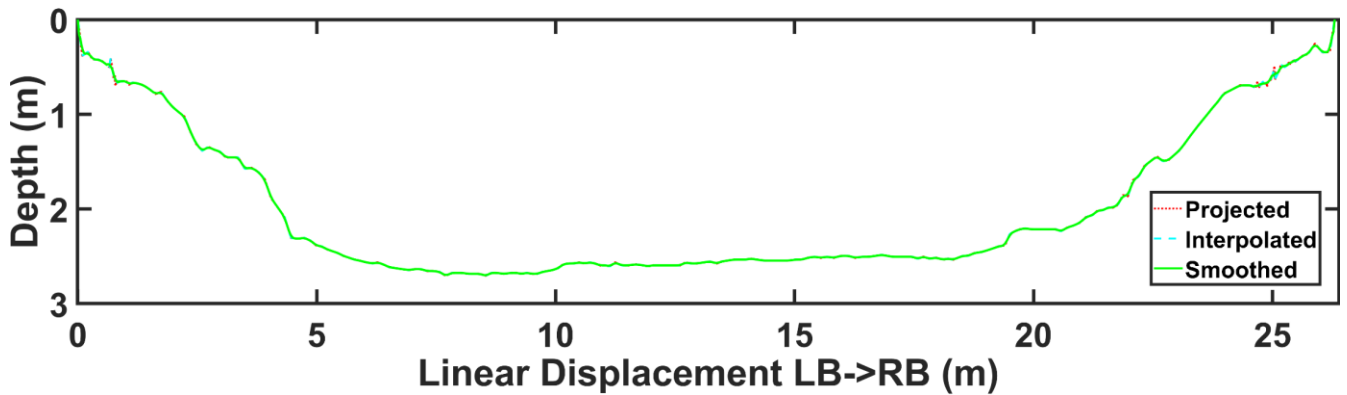


Figure 4.12: The cross section and depth measurements are linearly interpolated and smoothed with a 5 point moving average.

#### 4.7.4 Underwater imagery

Underwater imagery provides an effective way to obtain high resolution bathymetric maps. Equipment for collecting underwater imagery is discussed in Section 2.1.4, with data processing covered in Section 4.6. Underwater imagery processing with SfM using software such as Agisoft Metashape (or Pix4D) produces point clouds, georeferenced orthomosaics (Figure 4.7), 3D models (Figure 4.13), and DEMs. 3D models can include texture (Figure 4.14:Left) or be only a solid model (Figure 4.14:Right) defined by a triangular mesh.

DEM<sup>s</sup> are the most common output from processed underwater imagery and can be used for many applications (e.g. cross section bathymetry, roughness estimation, and as inputs to hydraulic models). If

underwater GCPs are used, then they also have the advantage of being accurately scaled and located in real world coordinates. This enables DEMs of underwater regions to be merged with terrestrial DEMs. For example, a drone can fly a larger survey covering dry parts of the riverbed, while wetted areas are covered by underwater imagery. This provides much higher resolution bathymetry (i.e. 2D maps) than the point samples obtained from waded RTK GPS surveys or transects obtained with an ADCP or depth sounder. While not as convenient (or providing as much spatial coverage) as bathymetry from through water imagery corrected for surface refraction (Section 4.7.7), the accuracy of DEMs from underwater imagery will be much higher as surface distortions (e.g. surface waves) are eliminated. This is advantageous for providing data to benchmark other depth estimation techniques, or for applications requiring highly accurate input DEMs. Underwater orthomosaics, DEMs and 3D models also have exciting potential for underwater grain size analysis (Section 4.9).



Figure 4.13: Tiled 3D model in the Waingawa River, derived from underwater imagery, with underwater GCPs comprised of metal washers, that were surveyed with RTK GPS.

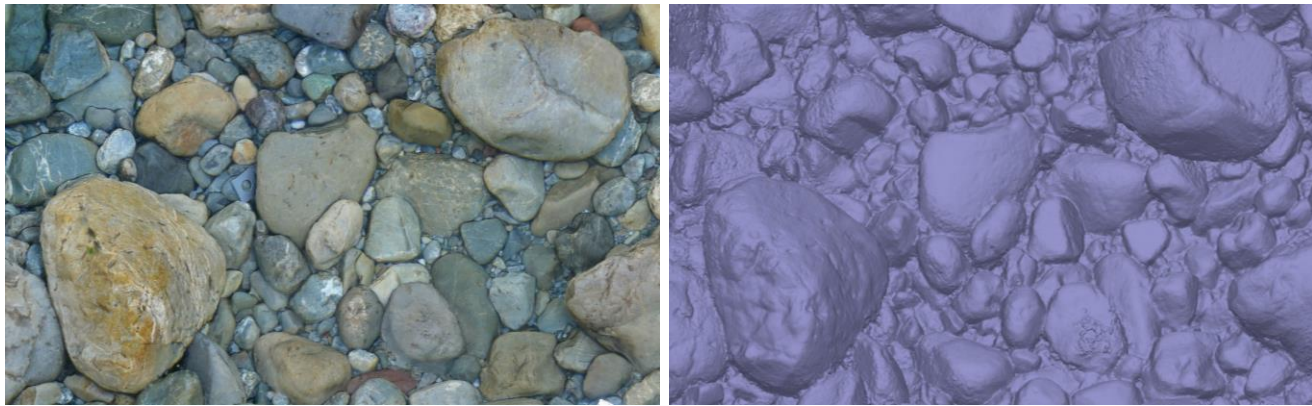


Figure 4.14: Zoomed example of a tiled 3D model (left) and a 3D solid model (right) in the Waingawa River. DEMs and 3D models from underwater imagery are a useful way to map river bathymetry.

#### 4.7.5 Ground Penetrating Radar (GPR)

Light weight aerial GPR systems provide a promising approach for resolving river bathymetry during floods (Figure 4.15). The aerial GPR system we tested was a MALÅ GeoDrone80 (Section 2.5.4). GPR data were pre-processed in the software GPR Slice<sup>21</sup>, to trim GPR data to a single transect (cross section), define the water surface elevation, define the bed elevation, and thus extract depth. This data was then exported as a text file with fields ‘Easting\_m’, ‘Northing\_m’, and ‘Depth\_m’, in the NZTM2000 coordinate system. The locations of the banks were manually added to the file as the first and last data records, with zero depth. Data were then imported into MATLAB where they were processed with the script ‘processGPRCrossSection.m’ (Appendix A).



Figure 4.15: Flood gauging in the Waimakariri River in New Zealand, with aerial GPR used for cross section bathymetry.

---

<sup>21</sup> Data processing in GPR Slice was performed by ‘drone flow’ team member John-Mark Woolley. Different GPR propagation velocities need to be applied for through air and through water transmissions. User best judgement was applied to define reflections off the riverbed.

The script ‘processGPRCrossSection.m’ defines a cross section between the first and last data records (i.e. the riverbanks), creates a cross section unit vector, then projects the GPR data onto this cross section (Figure 4.16). This is important to account for the drone flight path (Figure 4.17) and to make depth a function of cross stream displacement. Depth data are then linearly interpolated at regularly spaced points to generate the cross section (Figure 4.18).

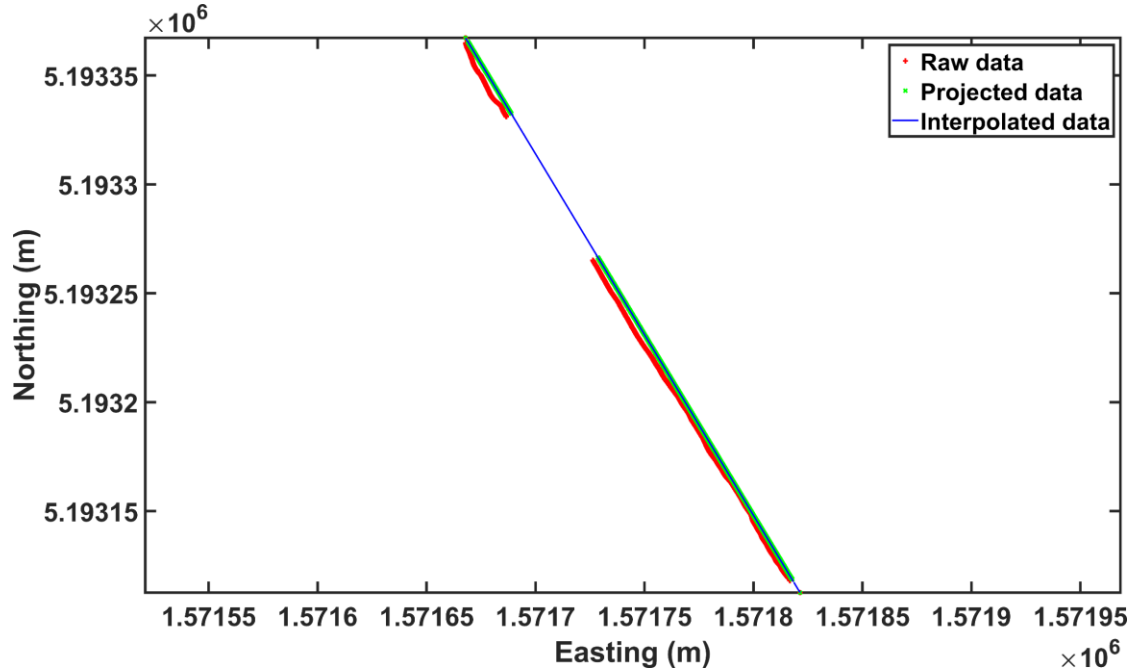


Figure 4.16: GPS locations of measured GPR data, which are then projected onto the cross section and linearly interpolated.

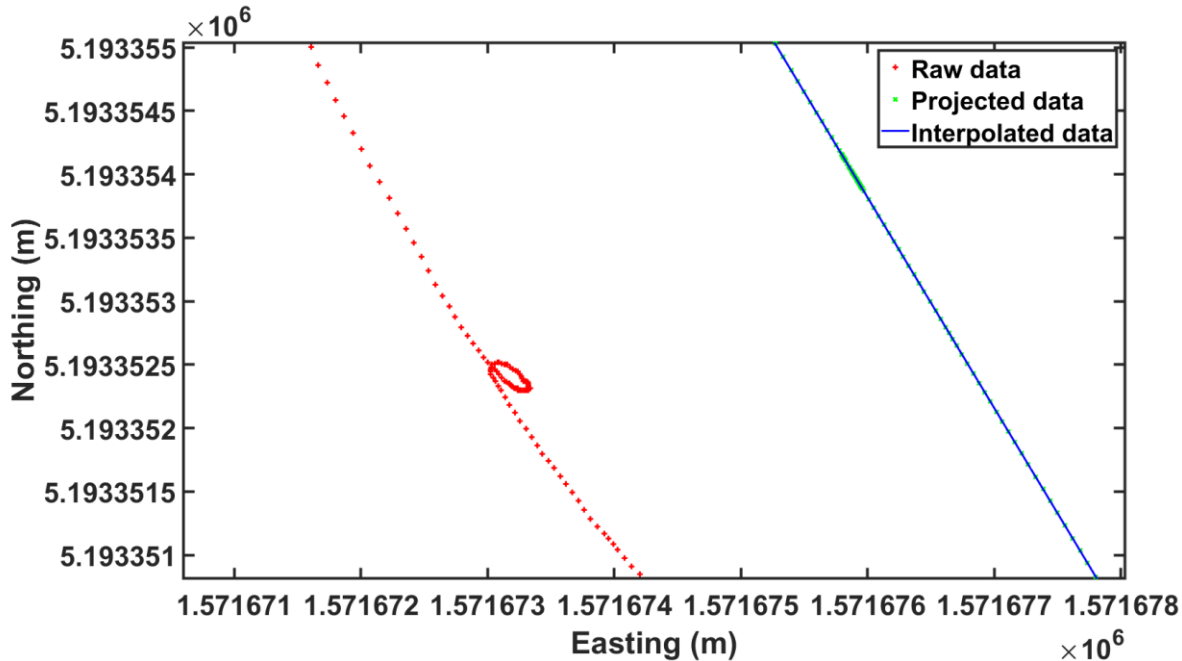


Figure 4.17: Projection of data onto the cross section is important to account for the drone flight path (not perfectly straight) and to remove any small loops. Data are then sorted by cross stream displacement and linearly interpolated.

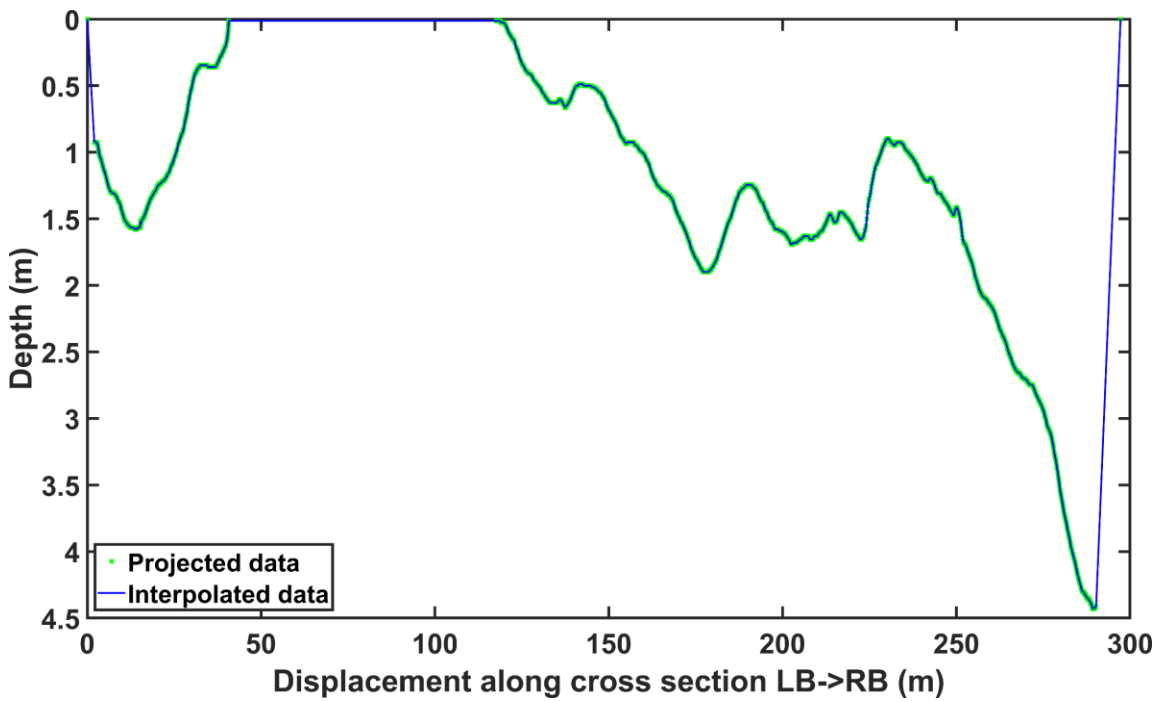


Figure 4.18: Cross section from aerial GPR in the Waimakariri River, New Zealand.

For the Waimakariri River example, surface velocities were calculated with STIV using the software Hydro-STIV in two sections (see Section 4.4). Part of the cross section in the Waimakariri River was a dry gravel bar/island that is visible in Figure 4.4 and Figure 4.18. Surface velocities and bathymetry can then be plotted together for the cross section (Figure 4.19) and show a plausible (approximately inverse) relationship, where higher surface velocities were found in deeper parts of the cross section, particularly near the true right bank where the channel was deeply scoured near the reinforced rock bank, and the Environment Canterbury (ECAN) gauging station.

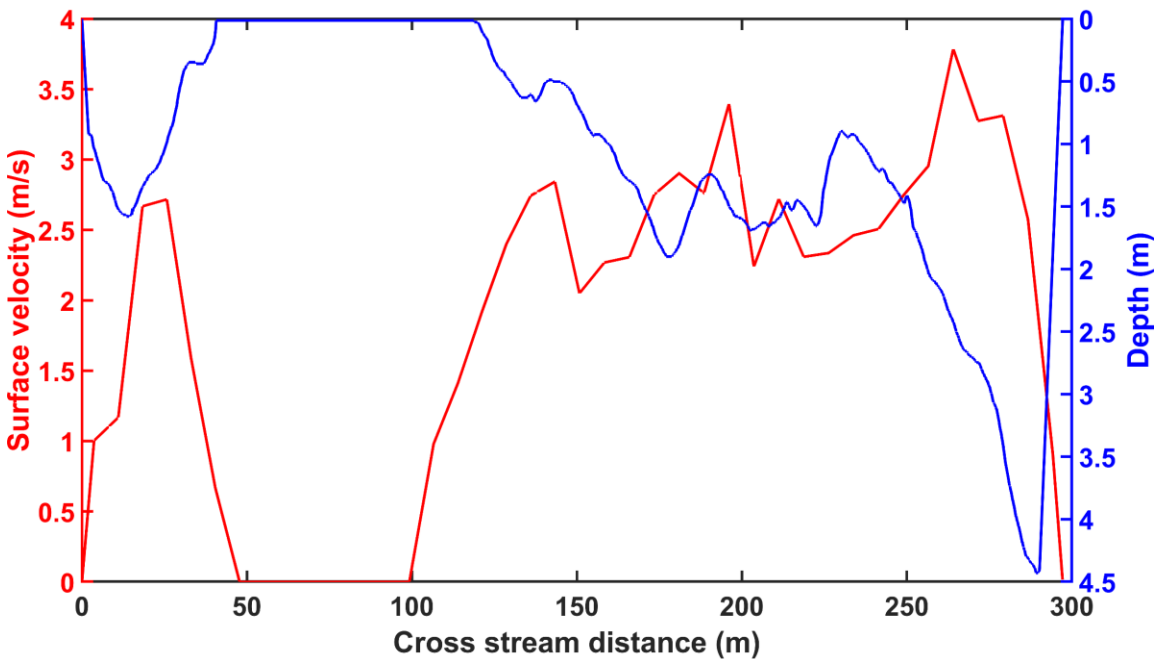


Figure 4.19: Comparison of surface velocities from STIV, depth from GPR, and cross stream distance (from the true left to the true right bank) in the Waimakariri River, New Zealand.

Bathymetry from GPR can then be combined with surface velocities and alpha to obtain discharge using the MATLAB script 'dischargeFromSurfaceVelocitiesAndCrossSection.m' (Appendix A). We did not have any additional information beyond depth from which to estimate alpha, so we used the value of 0.90 which is appropriate for deep channels (Section 4.8). The calculated discharge for this value of alpha was 749.675 m<sup>3</sup>/s which compares to a rated discharge at the site from ECAN of 813.695 m<sup>3</sup>/s.

Calculated discharge from surface velocities and bathymetry from GPR was quite close to rated discharge, which was promising. However, a thorough accuracy assessment was not possible as we did not have accurate reference bathymetry and discharge to compare against. Our GPR and surface velocimetry deployment occurred at short notice to capture the flood, and we did not have time to organise a jet boat ADCP gauging. However, ECAN do maintain a good rating at this site, so our underestimate of discharge is likely real, and not an artefact. There are multiple ways that this discharge could have been 'lost' but the most obvious candidate is from lack of bathymetry data near channel banks (Figure 4.19). This occurred when the channel bottom could not be reliably separated from other GPR reflections (i.e. through air reflections off banks, trees, and structures). More advanced data processing (or better antenna hardware) may improve near bank performance (see recommendations below). The assumed alpha value for the site of 0.90 may also have been too low (particularly if velocity dip at the surface was significant).

Overall the use of GPR for bathymetry for flood gauging is promising and further work is recommended.

#### Recommendations for future work:

- As discussed in Section 2.5.4 there are other antennas and systems available (such as the RadarTeam Cobra SE-70 or SE-150), and a direct comparison would be worthwhile. Particularly to see if they have better directionality.
- Data processing directly in MATLAB rather than GPR slice would also be useful. Code is needed to unpack .RD7 files and read them directly into MATLAB, which could be achieved by a MATLAB implementation of the code provided by <sup>22</sup>.
- Development of GPR processing algorithms that model through air reflections off terrestrial objects (based on projections of the antenna gain patterns onto an underlying DEM of terrestrial regions from aerial surveying). For example, these aerial antennas are not well coupled with the ground like traditional dragged GPR antennas. Therefore 3D modelling of antenna gain patterns and 3D ray tracing may be more beneficial than for traditional antennas (Annan, 2003).
- Development of GPR processing algorithms that include through water attenuation and use it to match expected signal strength with expected depth to filter out erroneous signals.
- More detailed field measurements with reference bathymetry, reference discharge, and better information for estimating alpha (i.e. site characteristics or velocity profiles).

#### **4.7.6 Water colour and spectral attenuation**

For relatively clear and shallow water, bathymetry can also be estimated from spectral information (e.g. Polcyn *et al.*, 1970; Lyzenga, 1978). These methods generally cover two key physical processes: (1) Scattering of light throughout the water column, which changes the detected 'colour' of the water as a function of depth; (2) Attenuation/absorption of red to near-infrared wavelengths as a function of depth. Methods involving process (1) primarily focus on light in the visible part of the spectrum that is not

<sup>22</sup> <https://wwwguidelinegeoc.cdn.triggerfish.cloud/uploads/2021/03/MALA-formats-rd3-and-rd7.pdf>

significantly attenuated by depth (i.e. blue to green/yellow wavelengths), whereas process (2) focuses on the red to near-infrared parts of the spectrum, generally limiting its use to multispectral, or hyperspectral cameras (Section 2.1.3). Braided rivers in New Zealand provide a good example of how ‘colour’ changes with depth due to scattering from fine sediment throughout the water column (Figure 4.20). Bathymetry estimation from water colour and spectral attenuation has been an active area of research for a long time and has seen widespread application globally, covering diverse environments from oceans to rivers. These methods are useful for relatively clear and shallow water (Legleiter & Fosness, 2019), but are limited by turbidity, where the signal becomes saturated beyond a certain depth, making them unsuitable for bathymetry estimation during floods. There can also be issues with heterogenous bed cover (e.g. sediment lithology, spatial distributions of different sediment size fractions, and periphyton cover) which can complicate classifications if they have different reflectance characteristics (Winterbottom & Gilvear, 1997).



Figure 4.20: Braided gravel bed rivers such as the Rakaia River in New Zealand are suitable for estimation of bathymetry from colour during periods of relatively low flows. At higher flows turbidity increases and signals saturate, limiting the maximum detectable depth. (Image from Dave Allen)

Bathymetry from colour and spectral attenuation has been applied using a wide range of measurement sensors, and processing algorithms. There is no ‘one size fits all’ approach for this type of remote sensing, as different environments have different measurement challenges, and suit different equipment and processing methods. There are also tradeoffs between cost, complexity, resolution, and accuracy, for the selection of different measurement equipment and data processing methods. As such, an overview of relevant literature is provided below which aims to point readers in the right direction for a deeper investigation of the subject. References are classified by ‘Sensor type’ and ‘Imagery processing method’,

with an additional list of ‘Other resources’ that may be useful. Finally, this section finishes with the authors opinion on ‘Practical implementation of bathymetry from water colour and spectral attenuation’.

#### Sensor type:

- RGB (Westaway *et al.*, 2003; Hicks *et al.*, 2006; Mandlburger *et al.*, 2021<sup>23</sup>).
- Multispectral (Polcyn *et al.*, 1970; Lyzenga, 1978; Winterbottom & Gilvear, 1997; Lyzenga *et al.*, 2006; Legleiter & Harrison, 2019; Rossi *et al.*, 2020; Legleiter, 2021).
- Hyperspectral (Lesser & Mobley, 2007; Legleiter *et al.*, 2009; Jay & Guillaume, 2014; Pan *et al.*, 2015; Legleiter, 2016; Legleiter *et al.*, 2018; Dilbone *et al.*, 2018; Legleiter & Fosness, 2019; Legleiter & Harrison, 2019; Legleiter, 2021).

#### Imagery processing method:

- Shallow water reflectance modelling (Lyzenga *et al.*, 2006).
- Optimal Band Ratio Analysis (OBRA) (Winterbottom & Gilvear, 1997; Legleiter *et al.*, 2009; Legleiter & Harrison, 2019; Legleiter, 2021).
  - OBRA of Progressively Truncated Input Depths (OPTID) (Legleiter *et al.*, 2018; Legleiter & Fosness, 2019).
  - Stratified Optimal Band Ratio Analysis (SOBRA) (Legleiter *et al.*, 2018).
  - Generalised OBRA (GenOBRA) (Legleiter & Harrison, 2019; Legleiter & Fosness, 2019).
  - Lowess OBRA (Dilbone *et al.*, 2018; Legleiter & Harrison, 2019).
  - Generalised OPTID (Legleiter & Fosness, 2019; Legleiter & Harrison, 2019).
- Stmf Relative Water Depth (RDW) algorithm and Lyzenga algorithm (Rossi *et al.*, 2020).
- Spectral matching and look up tables (Lesser & Mobley, 2007).
- Maximum likelihood (Jay & Guillaume, 2014).
- Image-to-Depth Quantile Transformation (IDQT) (Legleiter, 2016; Dilbone *et al.*, 2018).
- Support Vector Regression (SVR) (Pan *et al.*, 2015).
- K-Nearest Neighbours (KNN) (Legleiter & Harrison, 2019).
- Neural Networks (Mandlburger *et al.*, 2021).

#### Other resources:

- Radiative transfer, scattering and other physical processes (Mobley, 1994; Mobley *et al.*, 2022)<sup>24</sup>.
- Radiative transfer modeling (Mobley, 1998).
- Radiometric calibration (Alevizos & Alexakis, 2022).
- Measurement of Inherent Optical Properties (IOPs) (Legleiter & Fosness, 2019; Legleiter & Harrison, 2019).
- The Optical River Bathymetry Toolkit (ORByT) (Legleiter, 2021)<sup>25</sup>.

#### Practical implementation of bathymetry from water colour and spectral attenuation:

Remote sensing of rivers with drones carrying multispectral cameras such as the Airphen Hyphen, or MicaSense RedEdge-MX and RedEdge-MX Blue (dual camera system) is easy, practical, and relatively cost effective. This data is far simpler to collect and process than push broom hyperspectral camera data (Section 2.1.3) and also has higher spatial accuracy. Multispectral imagery can be processed with SfM software (i.e. Agisoft Metashape or Pix4D), and GCPs can be incorporated to generate georeferenced

<sup>23</sup> Imagery was Red, Green, Blue, Coastal Blue (RGBC) where  $\lambda$  Coastal Blue was 400 to 460 nm.

<sup>24</sup> <https://www.oceanopticsbook.info/>

<sup>25</sup> <https://code.usgs.gov/cjl/orbyt-optical-river-bathymetry-toolkit/>

orthomosaics and DEMs/DSMs. Multispectral cameras can also be operated with calibration tarpaulins (or targets) and downwelling irradiance sensors to convert upwelling radiance data to reflectance. The spatial accuracy of multispectral imagery, and the ability to generate DEMs/DSMs provides a distinctive advantage over push broom hyperspectral scanners, where a DSM needs to be obtained by another means and used for georectification of the hyperspectral imagery. While the spectral resolution of hyperspectral cameras is better, which helps with classification tasks, deployment of these systems on drones is not as practical for mapping large areas. The recent release of the Optical River Bathymetry Toolkit (Legleiter, 2021) has provided a convenient way to use multispectral data for bathymetry estimation. Bathymetry of wetted regions from OBRA and ORByT can then be fused with DEMs/DSMs of terrestrial (dry) regions derived from SfM. This enables full coverage of a river reach, from only one multispectral camera flight. For very shallow and clear rivers it is also possible to extract bathymetry from through water imagery corrected for surface refraction for multispectral imagery (Section 4.7.7), however this method will struggle if there are a lack of distinctive features to match, limiting maximum depths and suitable bed substrate characteristics compared to spectral techniques.

#### Recommendations for future work:

- Future work on automated delineation of the wetted surface of rivers to create highly accurate masks is recommended. This could likely be achieved by incorporating a thermal infrared data channel as well as RGB or multispectral imagery for use in classifications. This would enable the generation of masks that could be used to separate the accurate terrestrial parts of DEMs/DSMs derived from SfM from the wetted regions. These masks would also function to delineate the input regions for bathymetry from colour and spectral attenuation. This would be particularly beneficial for braided rivers (Figure 4.20), that have a heterogenous wetted surface which is time consuming to manually delineate.
- It is also recommended to investigate hybrid approaches that fuse depth estimates from through water imagery corrected for surface refraction (for shallow regions with heterogenous bed material with different reflectance characteristics) with bathymetry from colour and spectral attenuation for deeper regions.

#### **4.7.7 Through water imagery corrected for surface refraction**

For shallow, clear water, with distinctive bottom features, bathymetry can be resolved from through water imagery corrected for surface refraction (Westaway *et al.*, 2000 & 2001; Butler *et al.*, 2002; Woodget *et al.*, 2015; Dietrich, 2017; Mulsow *et al.*, 2018; Skarlatos & Agrafiotis, 2018; Mandlburger, 2019; Agrafiotis *et al.*, 2020; Cao *et al.*, 2020). These methods have been around for a long time (Tewinkel, 1963; Rinner, 1969; Okamoto, 1984) but have gained popularity as the use of drones for aerial surveying has increased. Likewise, the ready availability of quality Structure from Motion (SfM) software such as Agisoft Metashape and Pix4D has greatly improved the practicality of dense point matching.

The use of this technique usually assumes a planar water surface, such that an underwater object (key point) observed from two different locations and viewing angles (matched key point), can be described by two refracted light rays that lie within two separate (but intersecting) planes (Tewinkel, 1963). These planes will intersect in a line that defines the 2D (i.e. XY) coordinates of the matched key point. However, the problem of depth estimation occurs because the projection of each light ray onto the other intersecting plane will occur at a different depth (for unequal viewing angles) due to refraction at the air-water interface (Dietrich, 2017; Cao *et al.*, 2020). Refraction is a function of the angle of intersection of each of the light rays with the water surface (i.e. Snell's law) (Tewinkel, 1963) and the refractive index of

water (Thormählen *et al.*, 1985; Harvey *et al.*, 1998). Refraction correction can be addressed with a range of methods, such as: simple 1D corrections for small refraction angles (Woodget *et al.*, 2015); iterative approaches (Dietrich, 2017); and methods involving the midpoint of skew lines (Cao *et al.*, 2020). If the intrinsic and extrinsic parameters of each camera (image) are known with high precision, and the water surface equation is known/defined, then forward intersection ray tracing methods can be used (Mulsow *et al.*, 2018), where 3D points are resolved from the closest distance between matched refracted rays. This approach is promising if a small proportion of the imagery is covered in water, such that underwater regions could be masked, and dry (terrestrial regions) used for ‘optimising cameras’ (i.e. calculating accurate intrinsic and extrinsic camera parameters), then forward intersection ray tracing methods used for bathymetry of the masked underwater regions. However, if the majority of the imagery is covered in water, then the problem becomes more challenging as it is very difficult to obtain accurate intrinsic and extrinsic camera parameters from underwater (refracted) key points (Mulsow *et al.*, 2018).

There are five main limitations for using bathymetry from through water imagery corrected for surface refraction: (1) water clarity; (2) sufficient/suitable bed features (i.e. key points) for matching; (3) evaluation of the water surface elevation/equation (for most methods); (4) the assumption that the water surface is planar; (5) errors in camera/image parameters, such as the location of the camera origin.

#### Future directions:

If water surface 3D geometry can be evaluated, then more advanced algorithms that account for surface geometry (i.e. waves) can be implemented (Okamoto, 1984; Mulsow *et al.*, 2018; Cassidy *et al.*, 2020; Cao *et al.*, 2020) (e.g. ray tracing methods with refraction at the air water interface and solving for the midpoint of the shortest distance between skew lines). However, the reconstruction of 3D water surface geometry is non-trivial, as it must be captured at the same time as the through water images of the bed. We are currently working on the use of the aerial stereoscopic camera (Section 2.1.2) for water surface reconstruction and simultaneous through water imaging of the bed. Our approach uses coloured tracer particles (Section 2.3) that can be separated from bed features and used for defining the water surface. This approach is promising, however higher densities of tracer particles are needed than were present in the initial tests, with further fieldwork and development required. While an interesting scientific development, it must be acknowledged that this method is not particularly practical, or accessible due to the specialist hardware and data processing required. As such, existing methods for bathymetry from through water imagery corrected for surface refraction that assume a planar water surface (i.e. Dietrich, 2017)<sup>26</sup> are more widely applicable.

### **4.7.8 Bathymetric LiDAR**

Bathymetric LiDAR (i.e. green LiDAR) is another promising technology for mapping rivers. Bathymetric LiDAR has also been around for quite a long time; however systems have traditionally been large, heavy, expensive, and often experimental (or with restricted access) (Hilldale & Raff, 2008; Kinzel *et al.*, 2013). The recent development of smaller light weight systems (Table 4-1) is opening up exciting possibilities for river bathymetric mapping, with some systems light enough to be deployed from drones (Kinzel *et al.*, 2021; Acharya *et al.*, 2021; Islam *et al.*, 2022). These smaller light weight systems are also designed for deployment from low altitudes, resulting in smaller laser footprints, higher resolution, and higher point densities. This makes them better suited for mapping heterogenous river bathymetry than traditional higher altitude airborne bathymetric LiDAR systems.

---

<sup>26</sup> <https://github.com/geojames/pvBathySfM>

Table 4-1: Examples of LiDAR systems for remote sensing river bathymetry (as of June, 2022).

<b>LiDAR system</b>	<b>Weight (kg)</b>	<b>Scan pattern</b>	<b>Suitable carrier vehicle</b>	<b>References and links</b>
TDOT 3 Green	~2.7	Line <sup>27</sup>	Medium lift drone (10-15 kg)	(Mano <i>et al.</i> , 2020; Islam <i>et al.</i> , 2022) <sup>28</sup> <a href="https://amuseoneself.com/data/amuseoneself_dot3_en.pdf">https://amuseoneself.com/data/amuseoneself_dot3_en.pdf</a>
Mapper4000U (under development)	4.4	Elliptical	Heavy lift drone (15-25 kg)	(Wang <i>et al.</i> , 2022)
Astralite EDGE™	5	Line (whisk broom)	Heavy lift drone (15-25 kg)	(Kinzel <i>et al.</i> , 2021) <a href="https://www.astralite.net/_files/ugd/7f51ca_490c729a3c80449a85f56d37eb535f15.pdf">https://www.astralite.net/_files/ugd/7f51ca_490c729a3c80449a85f56d37eb535f15.pdf</a>
RIEGL BDF-1	~5.3	Point samples (bathymetric depth finder)	Heavy lift drone (15-25 kg) (e.g. RIEGL Bathycopter)	(Mandlburger <i>et al.</i> , 2016; LeWinter <i>et al.</i> , 2018) <a href="http://www.riegl.com/uploads/ttxpxpriegeDownloads/RIEGL_BDF-1_Datasheet_2019-05-31.pdf">http://www.riegl.com/uploads/ttxpxpriegeDownloads/RIEGL_BDF-1_Datasheet_2019-05-31.pdf</a>
RIEGL 840-G	12-15	Circular	Very heavy lift drone >25 kg, helicopter (low altitude)	(Mandlburger <i>et al.</i> , 2020) <a href="http://www.riegl.com/uploads/ttxpxpriegeDownloads/RIEGL_VQ-840-G_Datasheet_2022-03-15.pdf">http://www.riegl.com/uploads/ttxpxpriegeDownloads/RIEGL_VQ-840-G_Datasheet_2022-03-15.pdf</a>
Fugro RAMMS	~14 (pod) 35 (stack)	Line (push broom)	Pod configuration: Very heavy lift drone (>25 kg) Stack configuration: Light aircraft, helicopter	(Ventura, 2020) <a href="https://www.fugro.com/Widgets/MediaResourcesList/MediaResourceDownloadHandler.ashx?guid=eebbbf2-f3db-6785-9f9dff250019aa6e&amp;culture=en">https://www.fugro.com/Widgets/MediaResourcesList/MediaResourceDownloadHandler.ashx?guid=eebbbf2-f3db-6785-9f9dff250019aa6e&amp;culture=en</a>
RIEGL VQ-880-G II	~65	Circular	Light aircraft, helicopter	<a href="http://www.riegl.com/uploads/ttxpxpriegeDownloads/RIEGL_VQ-880-GII_Datasheet_2022-04-04.pdf">http://www.riegl.com/uploads/ttxpxpriegeDownloads/RIEGL_VQ-880-GII_Datasheet_2022-04-04.pdf</a>
RIEGL VQ-880-GH	~70	Circular	Light aircraft, helicopter	(Mandlburger, 2015) <sup>29</sup> <a href="http://www.riegl.com/uploads/ttxpxpriegeDownloads/RIEGL_VQ-880-GH_Datasheet_2022-04-04.pdf">http://www.riegl.com/uploads/ttxpxpriegeDownloads/RIEGL_VQ-880-GH_Datasheet_2022-04-04.pdf</a>

Some of the new systems (such as the TDOT 3 Green) are promising, but still need to be independently tested (Mandlburger *et al.*, 2020). There are also environmental limitations for the deployment of Bathymetric LiDAR, notably optical clarity (turbidity)<sup>30</sup>, and likely also water surface geometry/waves

<sup>27</sup> The scanning architecture is not specified and may be whisk broom or push broom.

<sup>28</sup> Likely these references used an older version of the TDOT Green.

<sup>29</sup> Study from April 2013 to October 2014, used models RIEGL VQ-820-G and VQ-880-G.

<sup>30</sup> Most bathymetric LiDAR systems are limited to 1-2 Secchi depths (3 Secchi depths is quoted for Fugro RAMMS).

(which may decrease accuracy due to refraction at the air-water interface). It also remains to be seen how the price of these systems will change over time, as they are currently extremely expensive (i.e. >\$300k NZD), putting them out of the reach of most researchers or institutions. The high cost of this hardware also generates further questions as to whether it is sensible to fly them on drones. While drones are convenient to use, they do have a much higher probability of crashing than manned aircraft (e.g. hardware/software faults, pilot errors, or environmental conditions). Until these systems are available at lower prices, they are unlikely to be widely adopted for remote sensing river bathymetry.

#### 4.7.9 Other techniques for bathymetry

##### Bathymetry from surface turbulence

Another method for estimating bathymetry is from integral length scales  $L_{ij,k}$  of surface turbulence (Johnson & Cowen, 2016). Where  $L_{11,1}$  captures the characteristic streamwise length scale of surface turbulent structures from streamwise velocity fluctuations, and  $L_{22,1}$  captures the characteristic streamwise length scale of surface turbulent structures from transverse velocity fluctuations. The use of  $L_{22,1}$  is generally preferred over  $L_{11,1}$ , since  $L_{22,1}$  requires less spatial coverage (Johnson & Cowen, 2016). While these methods are promising for flume data (particularly with a smooth bed), they are more challenging to apply in the field, where bathymetry is more heterogeneous. It is also harder to measure high resolution surface velocities for a long duration in the field, from which integral length scales can be calculated (Detert *et al.*, 2017). This is mainly due to practical limitations on the volumes of tracer particles that are needed to achieve high densities of surface velocities (Detert *et al.*, 2017).

The use of advanced infrared cameras (Legleiter *et al.*, 2017; Schweitzer & Cowen, 2021) may overcome issues with tracer particle densities and recording duration that occur for introduced visible tracers. However, field tests of IR cameras by Legleiter *et al.*, (2017) indicate that bathymetry from integral length scales of surface turbulence were outperformed by spectral methods such as OBRA (Section 4.7.6). Likely accuracy is influenced by the heterogeneity of depth in natural rivers (compared to flume experiments), leading to a wider range of turbulent length scales at the surface. The accuracy of these techniques may improve as the resolution and field of view of IR cameras increases (Legleiter *et al.*, 2017).

Beyond the use of integral length scales to estimate depth, there are other surface velocimetry approaches that also show promise. For example: from surface dissipation rates of turbulent kinetic energy (Jin & Liao, 2019); or the continuity equation for bathymetry over spatially heterogeneous bedform models (Lin *et al.*, 2022). While not yet operational for regular fieldwork, this is a promising area for the future, particularly for turbid flooded rivers, where methods requiring clear water cannot be used. Further research is recommended to improve the understanding of the free-surface behaviour of shallow turbulent flows (Muraro *et al.*, 2021) and improve the accuracy of bathymetry from surface velocity fields. Likewise further work is needed to improve the practicality of these methods, both for data collection with drones (e.g. flight time, coverage, and tracer densities), and for data processing.

##### Bathymetry from surface waves

Bathymetry can also be estimated from the propagation of surface wave fields (Polcyn *et al.*, 1970; Holman *et al.*, 2013; Dolcetti *et al.*, 2022). These methods were originally developed for coastal applications (Polcyn *et al.*, 1970), but have been extended to the more complicated case of rivers (Dolcetti *et al.*, 2022) where flow velocities are spatially heterogeneous (i.e. vertical velocity profiles and lateral variability). Data processing can focus on the 3D water surface structure, or frequency-dependent

characterisation of the wave field. Data for evaluating wave fields can be obtained in many ways, for example: single cameras (Holman *et al.*, 2013; Dolcetti *et al.*, 2022); stereoscopic cameras (Fedele *et al.*, 2013); aerial laser scanners (Gorman & Hicks, 2005); and microphone arrays (Dolcetti *et al.*, 2021).

During the ‘drone flow’ project, tests were performed using a terrestrial laser scanner (Snoopy A-Series from LiDAR USA) (Section 4.5.2) to quantify water surface 3D structure. However, low numbers of returns were received from the water surface (due to penetration into the water). This is similar to the results of (Höfle *et al.*, 2009) where high numbers of laser shot dropouts and low backscatter energy were used to classify water regions. It is unknown whether the feasibility of this technique would improve for highly turbid rivers (i.e. during large floods) or when there is a lot of floating debris and foam. The rotating nature of the LiDAR scan head, also creates issues, as it does not create an instantaneous ‘snapshot’ of the surface structure. Instead, terrain is built up from multiple scan passes (since the data acquisition from each scan head rotation is relatively low), making it less well suited for capturing transitory terrain features (i.e. waves) with a single scan pass. Another approach for evaluating water surface 3D structure was also tested during the drone flow project, by using a synchronous stereoscopic camera mounted on a drone (Section 2.1.2). While this was more promising, there were two main limitations: (1) the high densities of tracer particles needed for water surface reconstruction; (2) camera motion between frames creating problems for 3D surface reconstruction. Further development is needed, with the simpler case of deployment from a rigid structure (i.e. a bridge) being addressed before moving to aerial deployment of a moving camera system. For aerial deployment it is also recommended to first focus on narrow channels with fixed reference points for image stabilisation and referencing, before extending deployments to wide rivers and flood flows (where camera origin from RTK GPS and orientation from the IMU are required). An ideal system for 3D water surface reconstruction would likely be a stereoscopic camera system comprised of two high performance infrared cameras (Legleiter *et al.*, 2017; Schweitzer & Cowen, 2021). This would enable high densities of surface tracers to be achieved, without needing artificially introduced particles, however the cost and complexity of such a system likely makes it unrealistic in the near term.

#### Bathymetry from flow resistance:

Further methods for depth estimation have been proposed by Legleiter & Kinzel, (2021) that are based on the use of a flow resistance equation. This new approach is known as Depths Inferred from Velocities Estimated by Remote Sensing (DIVERS). It assumes steady, uniform, one-dimensional flow and a direct proportionality between the velocity estimated at a given location and the local water depth, with no lateral transfer of mass or momentum (Legleiter & Kinzel, 2021). While further testing, validation, and potentially refinement, are needed, initial results are encouraging (Legleiter & Kinzel, 2021). Other related progress in this area has been made by Branch *et al.*, (2021) to estimate bed drag coefficients from surface turbulence. While bathymetry from flow resistance is promising, further work is needed before it is sufficiently accurate and practical to apply.

#### **4.7.10 Summary of practicality of bathymetry techniques**

There is no ‘silver bullet’ for bathymetry estimation in rivers. All methods have their ‘pros’ and ‘cons’, covering cost, complexity, and suitability for different measurement conditions. The easiest methods to apply typically use ADCPs or depth sounders (Sections 4.7.1 to 4.7.3), since the data processing is simple, and other forms of ‘reference bathymetry’ are not needed. For flooded turbid rivers where contact measurements are not possible, the use of aerial GPR is promising (Section 4.7.5). For small-scale high-resolution bathymetry of clear rivers/channels the use of underwater imagery with underwater GCPs is effective (Section 4.7.4). For larger scale surveys of relatively clear and shallow channels, there are three

potential methods: (1) bathymetry from colour and spectral attenuation (Section 4.7.6); (2) through water imagery corrected for surface refraction (Section 4.7.7); and (3) bathymetric LiDAR (Section 4.7.8). With the selection of an appropriate method depending on available equipment and channel characteristics (i.e. clarity and bed cover).

## 4.8 Surface velocity to depth averaged velocity (alpha)

The accuracy of discharge measurements derived from surface velocities are highly dependent on the accuracy of conversions from surface velocity to depth averaged velocity (i.e. alpha) through  $\alpha = \frac{u}{u_s}$ . Different methods for estimating alpha were investigated in detail during the ‘drone flow’ project (e.g. Smart & Biggs, 2020; Smart, 2021a,b; Biggs *et al.*, 2021; and Smart, 2022). With Biggs *et al.*, (2021) providing a comprehensive ‘Field guide for selecting alpha’<sup>31</sup> that is designed for field hydrologists and researchers. An overview of different methods for estimating alpha is provided below.

### Site alpha from accurate reference discharge and discharge from surface velocimetry with $\alpha=1$ :

This is Method 1b from Biggs *et al.*, (2021) and is recommended if both an accurate reference discharge measurement  $Q_{Ref}$  and an accurate surface velocity measurement are available at the site.

$$\alpha = \frac{Q_{Ref}}{Q_{S,\alpha=1}}$$

Typically,  $Q_{Ref}$  is obtained from contact measurements (e.g. ADCP, POEM<sup>32</sup>, current meter, dilution gauging), and  $Q_{S,\alpha=1}$  is obtained from surface velocity measurements (i.e. surface image velocimetry, doppler radar), but with the alpha coefficient set to 1. It is easy to obtain  $Q_{S,\alpha=1}$  using drone based aerial imagery and processing in software such as Hydro-STIV (Section 4.1), then evaluating discharge with  $\alpha = 1$  (Figure 4.2). See Biggs *et al.*, (2021) for detailed explanations, derivations, and examples.

This approach has multiple advantages over other methods because surface velocities are measured directly, rather than being extrapolated from in situ velocity measurements (i.e. from ADCPs), which have significant near surface uncertainty due to blanking distances, wind effects and secondary currents. By repeating this approach at multiple discharges (i.e. stage levels) a site-specific stage-alpha rating curve can be constructed. These site-specific stage-alpha rating curves can then be extrapolated to estimate alpha at discharges higher than those that can be measured directly with instream equipment, improving the accuracy of flood gaugings.

### Site alpha from extrapolated ADCP velocity data:

This is Method 1a from Biggs *et al.*, (2021) and is recommended if ADCP velocity profiles are available at a study site. This is a standard method for estimating alpha (e.g. Hauet *et al.*, 2018; Randall, 2021), with velocity profiles typically measured with ADCPs (Section 2.5.1), then extrapolated to the surface and used to estimate alpha. This approach generally works well, however there can be uncertainties introduced due to ADCP blanking distances and extrapolation to the surface (particularly in windy conditions). To improve the accuracy of this method surface velocities can also be measured directly (i.e. from surface image velocimetry, or doppler radar) and combined with velocity profile data. Velocity profile data can either come from surface ADCPs (i.e. down-looking), or ideally up-looking ADCPs on benthic landers (Section 2.5.3) that are synchronised with surface velocity measurements. However, data

<sup>31</sup> [https://www.researchgate.net/publication/352833904\\_River\\_discharge\\_from\\_surface\\_velocity\\_measurements\\_A\\_field\\_guide\\_for\\_selecting\\_alpha](https://www.researchgate.net/publication/352833904_River_discharge_from_surface_velocity_measurements_A_field_guide_for_selecting_alpha)

<sup>32</sup> <https://niwa.co.nz/our-services/instruments/instrumentsystems/products/water-flow-instruments/poem>

collection and processing for this is more complicated than the velocity profile extrapolation methods that are typically employed in QRev (e.g. Randall, 2021).

#### Alpha from log law profiles:

This is Method 2a from Biggs *et al.*, (2021) and is recommended if reference discharge (or velocity profiles) are unavailable, but data on depth, slope, and surface velocity are available. Typically, this data can be obtained from remote sensing of rivers (i.e. ‘drone flow’ measurements).

For relatively deep flows where  $H \gg Z_0$  and  $u_* = \sqrt{gHS}$ ,

$$\alpha = 1 - \frac{\sqrt{gHS}}{\kappa u_s}$$

where  $H$  is depth,  $Z_0$  is the roughness coefficient from the log law velocity profile,  $u_*$  is friction velocity,  $g$  is gravitational acceleration,  $S$  is slope,  $\kappa = 0.40546$  is the Von Kármán constant (Smart, 2022), and  $u_s$  is the time averaged surface velocity (Smart & Biggs, 2020).

This equation was improved by Biggs *et al.*, (2021) to cover both relatively deep and relatively shallow flows, as:

$$\alpha = \frac{1}{1 - e^{-\left(\frac{u_s \kappa}{\sqrt{gHS}}\right)}} - \frac{\sqrt{gHS}}{\kappa u_s}$$

These equations are derived to estimate alpha for a single vertical profile, however, to estimate discharge a ‘site averaged’ alpha is needed. The recommended approach uses  $Q_{S,\alpha=1}$  (which was also employed in ‘Method 1b’) and can be easily obtained from software such as Hydro-STIV. Site averaged alpha for relatively deep flows where  $H \gg Z_0$  becomes:

$$\alpha_{site} = 1 - \frac{A\sqrt{gHS}}{\kappa Q_{S,\alpha=1}}$$

and site averaged alpha for relatively shallow flows becomes:

$$\alpha_{site} = \frac{1}{1 - e^{-\left(\frac{Q_{S,\alpha=1}\kappa}{A\sqrt{gHS}}\right)}} - \frac{A\sqrt{gHS}}{\kappa Q_{S,\alpha=1}}$$

See Biggs *et al.*, (2021) for derivations and detailed explanation of this method. The major advantage of this method is that all input parameters can be easily obtained from remote sensing data. For example, bathymetry can be obtained from aerial GPR, surface velocities from LSPIV or STIV, and slope from a DEM derived from aerial surveying of the reach.

Downsides to this approach are that: slope can be hard to measure accurately (particularly in low gradient rivers);  $u_* = \sqrt{gHS}$  may be inaccurate in some cases (Smart & Biggs, 2020); and log profiles are

assumed to extend to the water's surface, which deviates from reality in many cases due to surface wind effects and secondary currents.

#### Alpha from power law profiles:

This is Method 2b from Biggs *et al.*, (2021) and can be used if velocity profiles are well represented by a power law. For power laws expressed with the form  $\frac{\bar{u}}{u_*} = a \left(\frac{z}{d}\right)^M$ , alpha is:

$$\alpha = \frac{1}{M + 1}$$

It is also common to see power laws expressed with the form  $\frac{\bar{u}}{u_*} = a \left(\frac{z}{d}\right)^{\frac{1}{m}}$  (e.g. ISO748, 2007; Welber *et al.*, 2016; Johnson & Cowen, 2017) in which case alpha is:

$$\alpha = \frac{m}{m + 1}$$

While results are equivalent whether using  $M$  or  $\frac{1}{m}$ , it is important to be aware of the difference. The power law exponent provided in QRev is  $M$ .

#### Alpha from site characteristics:

This is Method 3b from Biggs *et al.*, (2021) and should be used if general information about the site roughness can be estimated. For example, a smooth artificial channel will have an alpha coefficient of ~0.9 (Rantz, 1982). A summary of the recommended estimates for alpha are provided in Table 4-2 and Table 4-3, with further information in Biggs *et al.*, (2021). For deep flows higher values of alpha have been reported, which may be due to velocity dip at the water's surface. For sites greater than 2 m deep Hauet *et al.*, (2018) recommend using  $\alpha = 0.90$ . We agree that this is prudent for deep sites, but recommend estimating alpha from Table 4-2 or Table 4-3 for shallower sites if more information is available.

Table 4-2: Estimating  $\alpha$  based on site roughness and expected power law profile exponents (Le Coz *et al.*, 2011; Fujita, 2018), where the power law exponent is represented as  $1/m$  or  $M$ .

	<b>normal</b>	<b>smooth</b>	<b>rough</b>	<b>very rough</b>	<b>extreme cases</b>
m	6-7	10	4	2-3	
M	0.143-0.167	0.1	0.25	0.333-0.5	
$\alpha$	0.86-0.87	0.91	0.8	0.67-0.75	0.6-1.2

Table 4-3: Estimating  $\alpha$  from relative depth and power law exponents using  $\alpha = 1/(M+1)$  (Smart, 2021b). Based on data from Hicks & Mason, (1991) covering more than 100 New Zealand rivers.

H/d <sub>84</sub>	M	$\alpha$
>30	0.16	0.86
10 - 30	0.19	0.84
2 - 10	0.58	0.63
< 2	1.59	0.37

### Alpha ‘default’ value:

This is Method 3a from Biggs *et al.*, (2021) and should be used if there is no other information available about the measurement site. The default value of  $\alpha = 0.857$  originates from integration of a 1/6<sup>th</sup> power law velocity profile (Smart & Biggs, 2020), and has been widely applied over the years as 0.85 or 0.86 (Rantz, 1982). However, as relative roughness changes (i.e. shallow rough bed flows vs deep flows in smooth artificial channels) then alpha will deviate from the default value resulting in significant errors. Typically, site characteristics can be used to better estimate alpha, rather than using the ‘default’ value.

### Workflow diagram for selecting the alpha estimation method:

With six different methods for selecting alpha presented above, it may be challenging to select the best one. To help with this, a workflow diagram has been included below (Figure 4.21), with further information provided in Biggs *et al.*, (2021) – Appendix E.

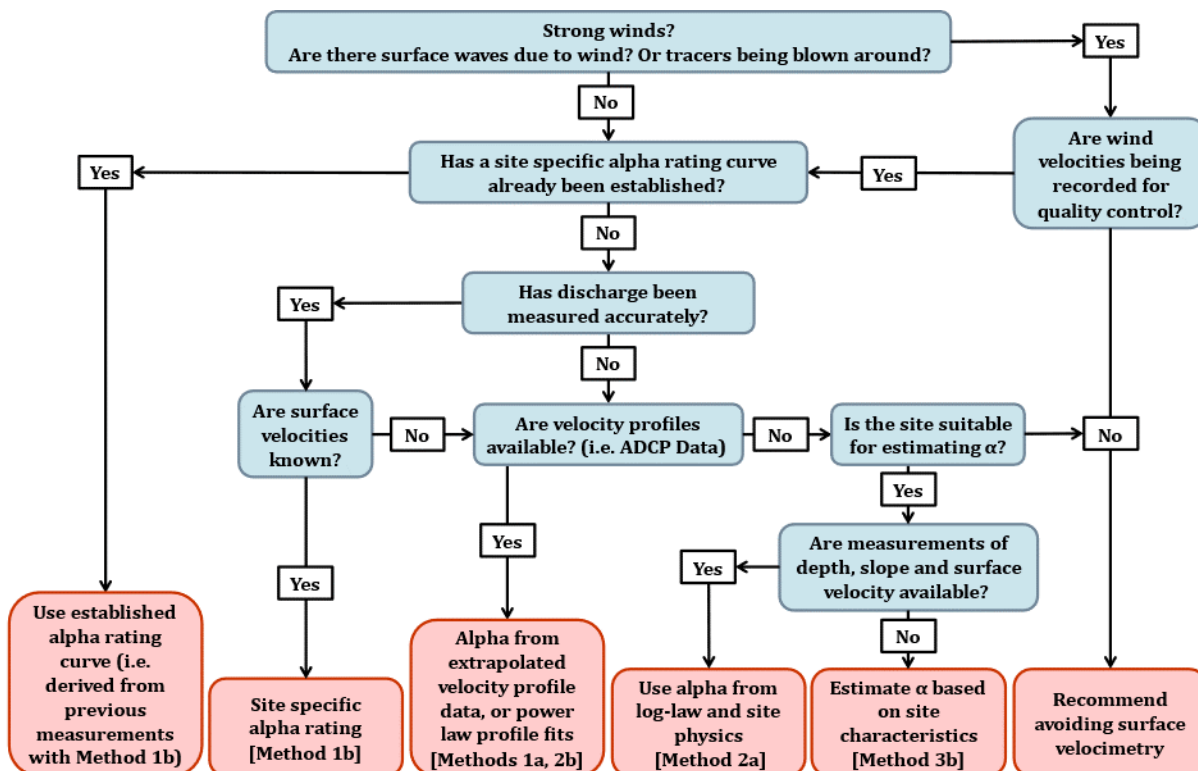


Figure 4.21: Workflow diagram for selecting the alpha estimation method from Biggs *et al.*, (2021).

Sites unsuitable for estimating alpha without instream measurements (Figure 4.21) are ones with highly three dimensional flow, where velocity profile shapes cannot be estimated and will not follow a log law or power law profile. This commonly occurs for channels with flow resistance distributed throughout the water column (not just from the bed), such as channels full of aquatic vegetation (Biggs *et al.*, 2019).

#### 4.8.1 Wind effects on surface velocimetry

Surface wind is a significant problem for surface velocimetry methods (Hauet *et al.*, 2018; Peña-Haro *et al.*, 2020; Randall, 2021). Wind blowing upstream will slow surface velocities and increase alpha values, while wind blowing downstream will increase surface velocities and decrease alpha values. Wind effects are very complicated to address analytically (Smart, 2021a,b) as impacts on the water surface velocity

depend on many factors such as: wind shear stress (e.g. wind velocity profiles and turbulence); fetch; surface roughness (which has a feedback loop with wind generated surface waves); surface tracer types (i.e. surface particles such as wood shavings, or surface features such as boils and eddies); and likely the turbulent mixing characteristics of the channel itself (i.e. vertical mixing of wind disturbed surface water).

Detailed wind measurements were undertaken during the ‘drone flow’ project to quantify the effect of wind on velocity profiles and alpha (Sections 2.5.2 and 2.5.5). Further field measurements and analysis of this data to generate firm conclusions is ongoing. Until this work is completed, we recommend using the workflow diagram from Figure 4.21 if wind is present at the site. If possible, it is also recommended to measure representative wind velocities at the site using anemometers or climate stations (Section 2.5.5) for Quality Control (QC). Further information about wind and alpha is contained in Biggs *et al.*, (2021).

## 4.9 Sediment size estimation from imagery

Sediment grain size analysis is often needed for river surveys. Techniques such as bulk sieving (Kondolf & Lisle, 2003) are accurate, but they are very time consuming, resulting in limited spatial coverage. Bulk sieving is also impractical when substrate sizes are very coarse (i.e. large boulders), and other methods such as Wolman counts are usually applied instead. Sediment size estimation from imagery provides a promising alternative to manual sediment measurements. However, these techniques only cover surface sediment (as do Wolman counts) and are limited by the spatial resolution of the input imagery, such that there is a minimum grain size that can be resolved. Therefore, other methods and equipment may also need to be applied in conjunction with image analysis if grain size distributions of fine sediments are also required (Hicks & Gomez, 2003; Haddadchi, 2017).

Sediment size estimation from imagery can be achieved using many different methods. For example: image analysis that delineates grain boundaries (Buscombe, 2008; Detert & Weitbrecht, 2013); statistical methods (Buscombe & Masselink 2009); wavelet methods (Buscombe, 2013); combined 2D/3D methods (Detert *et al.*, 2018; Detert *et al.*, 2019b); and deep learning methods (Buscombe, 2020). There is also a range of useful software that has been released for grain size analysis from images<sup>33,34</sup>. For example, the user-friendly MATLAB tool BASEGRAIN (Figure 4.22).

---

<sup>33</sup> <https://github.com/dbuscombe-usgs>

<sup>34</sup> <https://basement.ethz.ch/download/tools/basegrain.html>

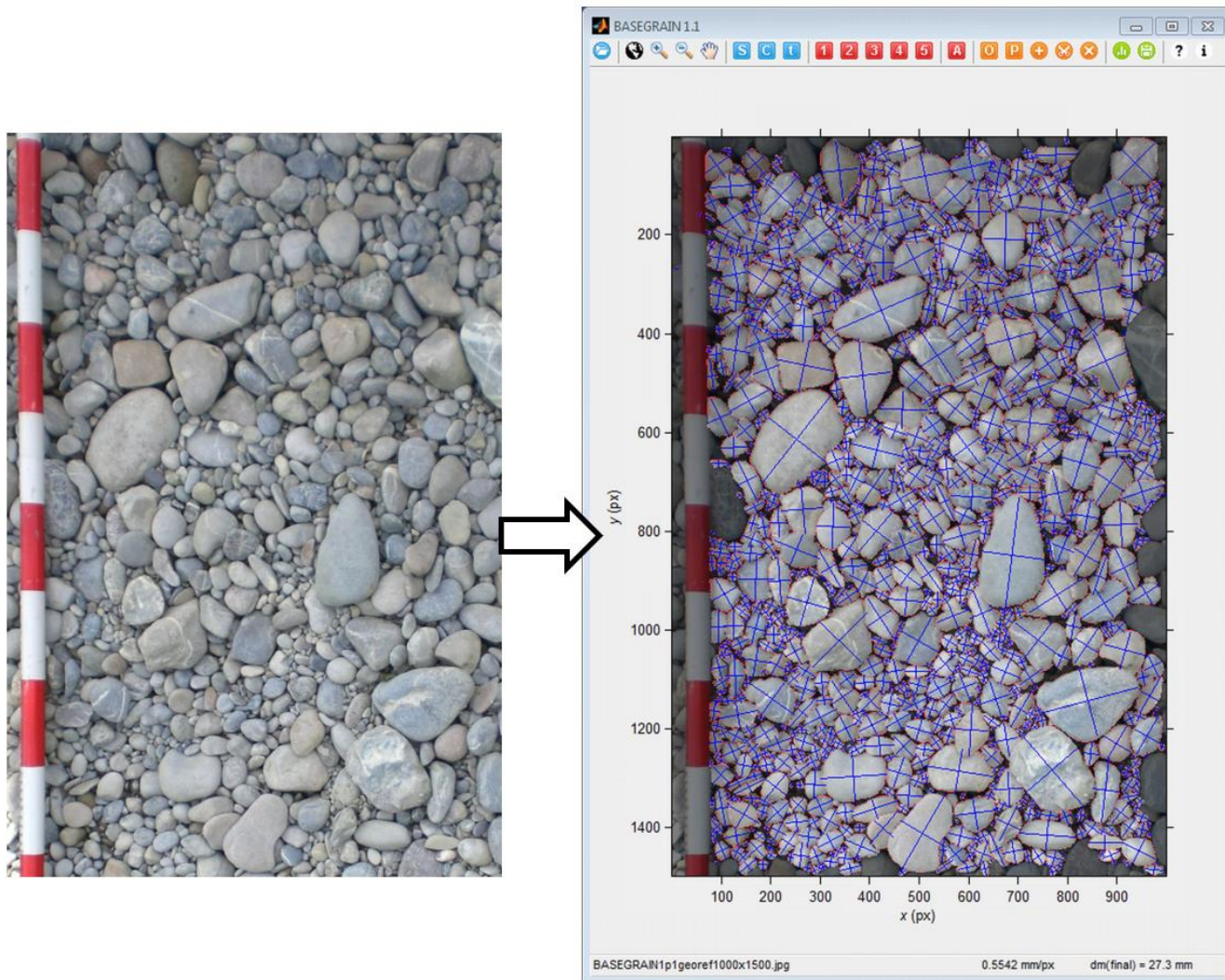


Figure 4.22: Grain size analysis with BASEGRAIN (Detert & Weitbrecht, 2013).

Images for sediment size estimation are usually acquired manually (Figure 4.22), or with drones during aerial surveys (for terrestrial sediment). When using drones, it is important to achieve high spatial resolution in the collected imagery. Usually this is achieved by low altitude flights for continuous mapping (i.e. 20-40 m). It can also be achieved by ‘point sampling’ at specific locations distributed throughout the study reach. For example, the whole reach can be mapped at higher altitudes (i.e. 60-120 m) for larger spatial coverage, then lower altitudes (i.e. 5-20 m) can be used for high resolution ‘sediment samples’. The camera and flight parameter calculator in Appendix E can be useful for planning flights and altitudes to obtain the image spatial resolution required. For grain size analysis it is very important to obtain clear, sharp imagery, with negligible blur. It is worth testing camera settings (notably focus and shutter speed) on a small subset of recorded images before commencing a full survey. For small surveys (or a small set of images) software such as BASEGRAIN is convenient (Detert & Weitbrecht, 2013), however for larger surveys (or a larger set of images), wavelet based analysis methods are more practical to apply and automate (Buscombe, 2013).

The measurement of underwater substrate size distributions is also possible. Underwater imagery and GCPs can be used to generate high resolution underwater orthomosaics, DEMs, and 3D models (Figure 4.23, Section 4.6, Section 4.7.4). These are well suited to grain size analysis methods that utilise both 2D

imagery and 3D spatial information (Figure 4.24, Detert *et al.*, 2019b). Further work is recommended to improve these methods.

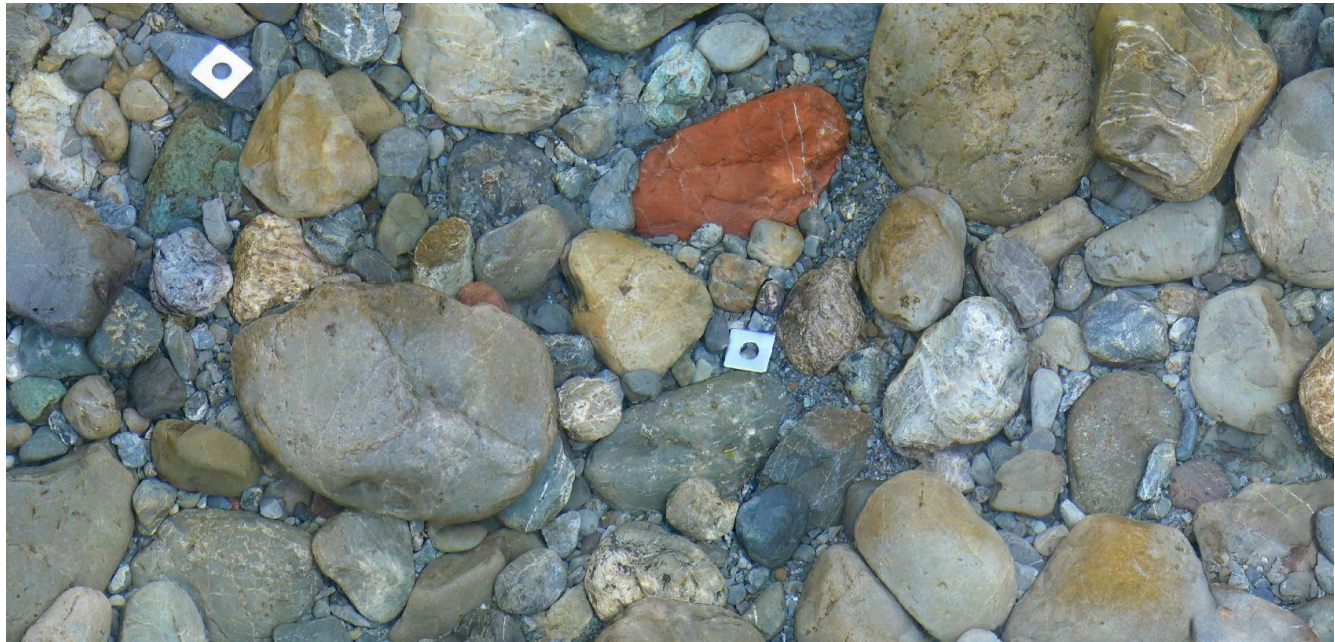


Figure 4.23: High resolution underwater georeferenced orthomosaic (Waingawa River, New Zealand).

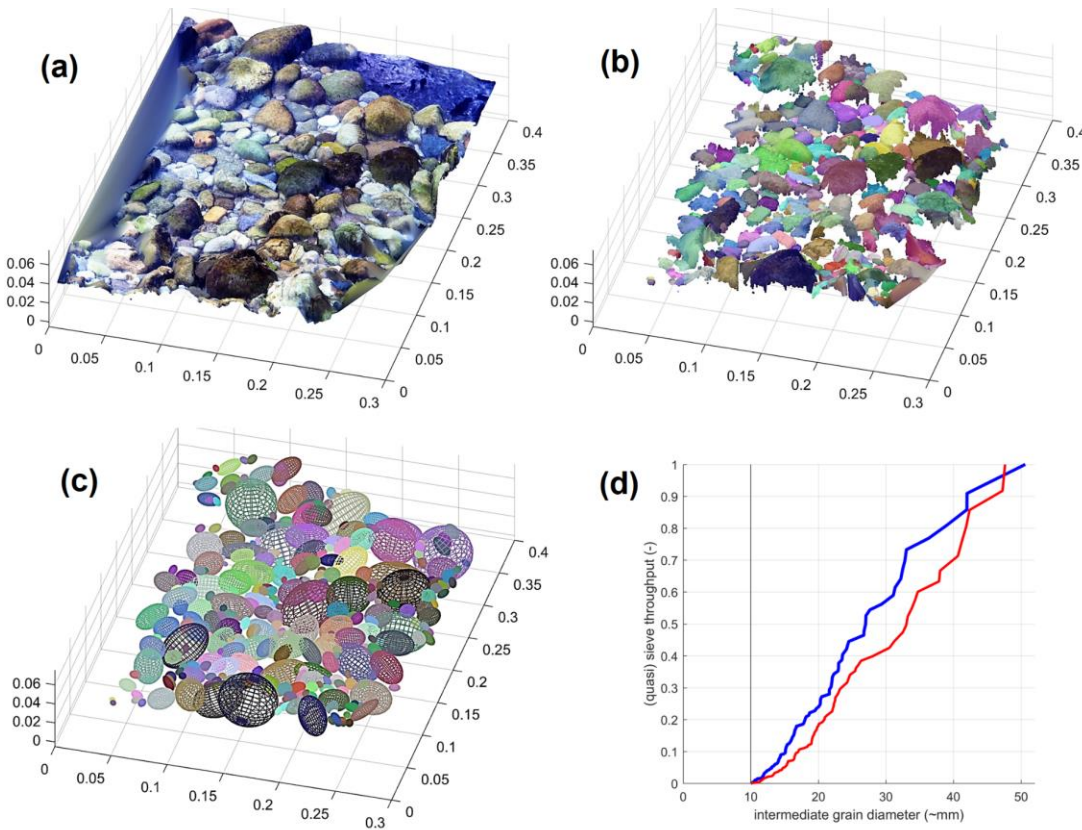


Figure 4.24: Grain size analysis of underwater sediment including 3D spatial data (Detert *et al.*, 2019b), showing: 3D model derived from underwater imagery (a); segmented 3D model based on analysis of the

2D orthomosaic in BASEGRAIN (b); fitting ellipsoids to the segmented 3D points (c); comparison of size distribution with BASEGRAIN in 2D (blue line) and 3D (red line) (d).

## 5 Summary of general advice for improving surface image velocimetry measurements

Surface image velocimetry is a powerful tool for flow measurement, however the inherent uncertainties of flow measurement from surface velocities must be understood. The relationship between surface velocity and depth averaged velocity ( $\alpha$ ) is only one potential source of uncertainty, and there can be significant challenges in accurately measuring surface velocities. More extensive recommendations can be found from sources such as Fujita, (2018), Engel *et al.*, (2021) and Randall, (2020; 2021). Here, a few recommendations are provided to improve the quality of input surface velocity data.

- Cameras must record videos with a consistent frame rate. Most cameras do this (i.e. DSLR, drone cameras, phone cameras etc), however avoid any IP cameras that only record ‘changes in motion’ where frame rate is inconsistent to minimise data storage or transmission (e.g. security cameras).
- Use cameras with rectilinear lenses where possible (i.e. not fisheye) to reduce errors associated with image correction.
- For fixed camera stations on channel banks mount cameras as high as possible to maximise the angular field of view (i.e. looking down on the channel), also try to include the full flow extent of large floods in the field of view.
- For fixed camera stations try to choose straight reaches with consistent geometry (i.e. a long run).
- Try to select sites where high flows are contained, rather than spilling out onto a flood plain.
- Select a measurement location with a stable cross section (if one exists).
- Try to avoid sites where distributed flow resistance throughout the water column creates irregular velocity profiles, for example: submerged aquatic vegetation, upstream bridge piers, and flood flows through riparian vegetation.
- For fixed camera stations place cameras on the bank that is facing away from the prevailing sun direction (i.e. cameras facing south in the southern hemisphere) to minimise surface reflections.
- For fixed camera stations a stable camera tower (i.e. pole or mast) is needed to minimise imagery vibration. Camera covers, wipers and heaters may be needed to remove rain drops and lens fog.
- For fixed camera stations install and survey more ground control points than are needed for orthorectification (i.e. more than 10) and distribute them widely around the site to fill as much of the image field of view as possible. This will help with image rectification and calculation of any lens distortion. It will also provide redundancy in case any ground control points are lost, obscured, mis-surveyed, or bumped/moved.
- Tracer particles are extremely important. For most routine gauging (outside of large floods) there will likely be insufficient tracer particles to use LSPIV for image processing. For sparse tracer particles STIV is recommended (or potentially PTV or FTV).
- If necessary, tracer particles can be added to a river from an upstream location, or using a drone mounted distribution system (Figure 5.1).
- For imagery with dappled sun glint (such as shallow flows with surface waves) tracer particles can be colour red using non-toxic biodegradable dye, then imagery can be thresholded in the HSV colour space prior to image processing to extract tracer particles (Biggs *et al.*, 2022a).
- Surface waves can also cause problems and errors for surface image velocimetry, as specular reflection from waves can be interpreted as bright tracer particles that are moving (Benetazzo *et al.*, 2017). The use of contrasting tracer particles (e.g. black particles on a bright background, or coloured particles for image thresholding) is recommended. The use of larger tracer particles (e.g. clumps of grass or vegetation thrown into the flow upstream) can also help to address this

problem. Imagery with specular reflection from surface waves is generally easier to process using STIV software such as Hydro-STIV or RIVeR-STIV, since manually defined gradient lines can be used to trace the passage of tracer particles and distinguish them from moving surface wave reflections.

- Aerial imagery processing is not trivial and often requires user judgement. The software Hydro-STIV is very user friendly, however in many situations the use of manually defined gradient lines in the STIV images is needed.
- Drone imagery will usually need to be stabilised before processing with surface velocimetry software. This can be performed in Fudaa-LSPIV, Hydro-STIV, or MATLAB.
- To obtain imagery with the best distribution of tracer particles, it is recommended to record longer videos (e.g. 5 minutes), then cut them to a suitable length for analysis (e.g. 1 minute). There are many ways to cut and edit videos, however a convenient method is to view the video in VLC media player, then ‘Record’ the best 1 minute section, which will export it as a separate video file (saved in the ‘Videos’ folder by default).
- In addition to wind measurements, it is also recommended to record additional meta data about the channel characteristics and gauging (e.g. substrate, site geometry [i.e. straight run, with a deep pool and bend 100 m downstream], rising/falling limb, aquatic vegetation, moving bed material, turbulence, waves etc). This information can be useful for categorising the site/gauging.

Discharge gauging from surface image velocimetry is non-trivial, and user-related errors are common (Detert, 2020). It is recommended for staff to attend training sessions and workshops prior to undertaking this work (where possible). The learning process can also be simplified by collecting easy to process input data. For example, well seeded (lots of tracer particles), rectilinear (not fisheye), orthorectified (down looking) and stabilised (not shaky, rotating, or drifting) drone footage, greatly simplifies data processing. Recording imagery that is already orthorectified also removes multiple sources of uncertainty (Le Coz *et al.*, 2021) and simplifies error analysis calculations.



Figure 5.1: NIWA environmental monitoring technician Hamish Sutton flying a tracer particle distribution system in the Tekapo Canal (left) and Rangitata River (right).

## 6 Conclusions

This user guide provides readers with an introduction to the wide range of equipment and measurement techniques that can be used for river remote sensing. It summarises developments across a broad area of research, and the references contained herein will assist readers seeking more detailed information about a specific measurement topic. The appendices of this user guide contain links to open source software for data processing, and CAD files for equipment development. There are multiple areas of research within this user guide where the ‘drone flow’ project team are continuing development, such as: bathymetry from aerial GPR; bathymetry from surface waves; stereoscopic flow gauging stations (oblique imagery) without GCPs; and the effect of surface wind on velocity profiles. Further advice about these topics is likely to be released in the future.



Figure 6.1: Surface velocity measurements with tracer particle distribution in a hydropower canal in New Zealand.

## 7 Future recommendations

Recommendations for future work are provided in more detail throughout this user guide at the end of each relevant section, however a summary of key points is provided here:

- The development of an upgraded stereoscopic camera with higher resolution and higher frame rate (dual USB3 busses, or larger in camera memory buffers) is recommended (Section 2.1.2).
- The development of an underwater imagery glass bottom boat for high resolution bathymetric mapping and 3D riverbed reconstruction is recommended (Sections 2.1.4 and 4.6).
  - Including an assessment of the accuracy of underwater orthomosaics and DEMs from imagery without GCPs, but with RTK GPS for camera origin (Sections 2.1.4 and 4.6).
- The development of expanding tracer particles is recommended (Section 2.3.1).
- A detailed investigation of the accuracy of using raindrop splash points (and advected surface texture) as tracers for LSPIV is recommended (Section 2.3.1).
- Investigation of other colours of dyed tracer particles is recommended (Sections 2.3.2 and 2.3.3).
- A detailed comparison of aerial GPR antenna hardware (from different manufacturers) is recommended, with upgrades to include an IMU and RTK/PPK GPS (Sections 2.5.4 and 4.7.5).
- The development of more advanced processing algorithms for aerial GPR data are recommended (Sections 2.5.4 and 4.7.5).
- A detailed assessment of the accuracy of bathymetry from aerial GPR is recommended, with its limitations well defined (Sections 2.5.4 and 4.7.5).
- A detailed investigation of the use of thermal infrared imagery (combined with RGB or multispectral imagery) for automatic delineation of channel boundaries and wetted regions is recommended (Sections 2.5.7 and 4.7.6).
- The development and deployment of stereoscopic fixed camera stations is recommended, to enable measurement of water surface elevation, 3D reconstruction of surrogate GCPs at water level, and orthorectification without needing surveyed GCPs (Section 4.2).
- A systematic investigation of the potential of drones with RTK GPS is recommended. Covering:
  - Measurement of river widths and the locations of surrogate GCPs (Section 4.3).
  - Sections of surface image velocimetry in wide rivers, by projecting imagery onto the water surface from camera origin, field of view, and water surface elevation (Section 4.4).
  - The accuracy of orthomosaics and DSMs/DEM without GCPs (Section 4.5.1).
- A systematic investigation to assess the accuracy of fused DSMs/DEM obtained from a single multispectral flight is recommended. Where terrestrial regions are obtained from SfM, while underwater regions are obtained from bathymetry from colour (or through water imagery corrected for surface refraction) (Sections 4.5.1, 4.7.6, and 4.7.7).
- Further work on through water imagery corrected for surface refraction, that uses ray tracing methods and water surface geometry is recommended (Section 4.7.7).
- A detailed assessment of the relative accuracy and limitations of different bathymetric LiDAR systems is recommended, including the new TDOT 3 Green model (Section 4.7.8).
- Further work on bathymetry from surface waves using a stereoscopic camera for 3D surface reconstruction is recommended, but with the stereoscopic camera fixed in space for simplicity (e.g. rigidly attached to a bridge) (Section 4.7.9).
- Further work on velocity profiles and alpha for shallow flows (i.e. low relative submergence) is recommended (Section 4.8).
- Further work on surface wind, surface shear stress, tracer movement (from wind loading), and velocity profiles is recommended (Section 4.8.1).
- Further work on the velocity dip phenomenon is recommended to separate the effects of secondary currents and surface air/wind interactions (Section 4.8.1).
- Investigation of underwater multispectral imagery for classification of rock lithology, grain size analysis, and periphyton mapping is recommended (Sections 2.1.4 and 4.6).
- Further work on grain size analysis that incorporates 3D information is recommended, to estimate the geometry of each grain hidden below bed level (Section 4.9).

## Acknowledgments

The work was funded by NIWA's 'drone flow' Research Programme, MBIE Smart Ideas Grant C01X1812, the support of which is gratefully acknowledged. Fieldwork in the Tekapo Canal was funded by NIWA's eFlows programme through the 'Velocity Profiles and Surface Wind' project FWWA2103. Development of the 'field guide for selecting alpha' was funded by MBIE Envirolink Advice Contracts C01X1936 2066-TSDC169 and C01X2008 2115-TSDC176. The authors would like to thank Jérôme Le Coz, Alexandre Hauet and Mark Randall for valuable discussions and advice during the project. The authors would like to thank Hydro Technology Institute Ltd (the developers of HydroSTIV) for collaborating on the project. The authors would also like to thank the hydropower companies Meridian Energy, Genesis Energy, and Trustpower for access to their field sites. The lead author of this advice document would like to acknowledge the valuable contributions of the entire project team (see below) and apologise in advance to any contributors who have been missed out in the acknowledgements. There are no known conflicts of interest related to the work.

### Drone flow team (NIWA Staff):

Alec Dempster
Andrew Lorrey
Andrew Starr
Arman Haddadchi
Brendon Smith
David Plew
Doug Booker
Duncan MacPherson
Graeme Smart
Guglielmo Stecca
Hamish Biggs
Hamish Sutton
Hayden McDermott
Jochen Bind
John-Mark Woolley
Murray Hicks
Richard Gorman

### Drone flow team (external collaborators):

Aeronavics Ltd
Hydro Technology Institute (Hydro-STIV Developers)
Jess Kerr (Scion)
Martin Detert (Meisser Surveying Ltd)
Matt Gardiner (Land River Sea Ltd)
Michael McDonald (Environment Southland)
Mike Ede (Marlborough District Council)
Nicholas Holwerda (Basins Environmental Ltd)
Robert Connell (Scion)
Phil Downes (Environment Canterbury)
Stuart Cameron (University of Aberdeen)
Tony Gray (Environment Canterbury)
Vladimir Nikora (University of Aberdeen)

## **Amendments**

The author welcomes the submission of suggestions for corrections and improvements to this document via email ([Hamish.Biggs@niwa.co.nz](mailto:Hamish.Biggs@niwa.co.nz)). If a revised version of this user guide is released in the future then amendments will be summarised here, along with appropriate acknowledgements and attribution.

## References

- Acharya, B., Bhandari, M., Bandini, F., Pizarro, A., Perks, M., Joshi, D., Wang, S., Dogwiler, T., Ray, R., Kharel, G. & Sharma, S. (2021). Unmanned aerial vehicles in hydrology and water management: Applications, challenges, and perspectives. *Water Resources Research*, 57(11).
- Agisoft. (2022). Agisoft Metashape User Manual: Professional Edition, Version 1.7. [https://www.agisoft.com/pdf/metashape-pro\\_1\\_7\\_en.pdf](https://www.agisoft.com/pdf/metashape-pro_1_7_en.pdf)
- Agrafiotis, P., Karantzalos, K., Georgopoulos, A. & Skarlatos, D. (2020). Correcting image refraction: Towards accurate aerial image-based bathymetry mapping in shallow waters. *Remote Sensing*, 12(2), 322.
- Alevizos, E. & Alexakis, D. (2022). Evaluation of radiometric calibration of drone-based imagery for improving shallow bathymetry retrieval. *Remote Sensing Letters*, 13(3), 311-321.
- Al-Mamari, M., Kantoush, S., Kobayashi, S., Sumi, T. & Saber, M. (2019). Real-Time Measurement of Flash-Flood in a Wadi Area by LSPIV and STIV. *Hydrology*, 6(1), 27.
- Annan, A.P. & Davis, J. (1977). Impulse radar applied to ice thickness measurements and freshwater bathymetry. Technical report, Current Research Part B, GSC Paper 77-1b, Geological Survey of Canada, 63–65.
- Annan, A.P. (2003). Ground penetrating radar principles, procedures and applications. *Sensors and software*, 278.
- Baker, G., Jordan, T. & Pardy, J. (2007). An introduction to ground penetrating radar (GPR). Special Papers-Geological Society of America, 432, 1-18.
- Beres Jr, M. & Haeni, F. (1991). Application of ground-penetrating-radar methods in hydrogeologic studies. *Groundwater*, 29(3), 375-386.
- Biggs, H., Nikora, V., Gibbins, C., Cameron, S., Papadopoulos, K., Stewart, M., Fraser, S., Vettori, D., Savio, M., O'Hare, M., Kucher, M. & Hicks, D.M. (2019). Flow interactions with an aquatic macrophyte: a field study using stereoscopic particle image velocimetry. *Journal of Ecohydraulics*, 4(2), 113-130.
- Biggs, H. (2019). Drones in hydraulics, IAHR Hydrolink magazine, feature article of the “Drone Special”, 4-6.
- Biggs, H. (2020). Aquatic vegetation aerial monitoring. In: *Unmanned Aerial Remote Sensing - UAS for Environmental Applications* (Ed. D. Green). CRC Press.
- Biggs, H., Smart G., Doyle, M., Holwerda, H., McDonald, M. & Ede, M. (2021). River discharge from surface velocity measurements – A field guide for selecting alpha. Envirolink Advice Report, Christchurch, New Zealand.
- Biggs, H., Smith, B., Detert, M. & Sutton, H. (2022a). Surface image velocimetry: Aerial tracer particle distribution system and techniques for reducing environmental noise with coloured tracer particles. *River Research and Applications*. 1-7.
- Biggs, H., Heath, M., Kuczynski, A., Bind, J., Daly, O., Safi, K. & Wood, S. (2022b). Microcoleus Aerial Monitoring User Guide, Envirolink Tools Report, Christchurch, New Zealand.
- Benetazzo, A., Gamba, M. & Barbirol, F. (2017). Unseeded large scale PIV measurements corrected for the capillary-gravity wave dynamics. *Rendiconti Lincei*, 28(2), 393-404.

- Booker, D., Henderson, R. & Whitehead, A. (2016). National water allocation statistics for environmental reporting. Prepared for the Ministry for the Environment. NIWA Client Report no. 2017065CH.
- Branch, R., Horner-Devine, A., Chickadel, C., Talke, S., Clark, D. & Jessup, A. (2021). Surface turbulence reveals riverbed drag coefficient. *Geophysical Research Letters*, 48(10), e2020GL092326.
- Buscombe, D. (2008). Estimation of grain-size distributions and associated parameters from digital images of sediment. *Sedimentary Geology*, 210(1-2), 1-10.
- Buscombe, D. & Masselink, G. (2009). Grain-size information from the statistical properties of digital images of sediment. *Sedimentology*, 56(2), 421-438.
- Buscombe, D. (2013). Transferable wavelet method for grain-size distribution from images of sediment surfaces and thin sections, and other natural granular patterns. *Sedimentology*, 60(7), 1709-1732.
- Buscombe, D. (2020). SediNet: A configurable deep learning model for mixed qualitative and quantitative optical granulometry. *Earth Surface Processes and Landforms*, 45(3), 638-651.
- Butler, J., Lane, S., Chandler, J. & Porfiri, E. (2002). Through-water close range digital photogrammetry in flume and field environments. *The Photogrammetric Record*, 17(99), 419-439.
- Cao, B., Deng, R. & Zhu, S. (2020). Universal algorithm for water depth refraction correction in through-water stereo remote sensing. *International Journal of Applied Earth Observation and Geoinformation*, 91, 102108.
- Cao, L., Weitbrecht, V., Li, D. & Detert, M. (2020). Airborne Feature Matching Velocimetry for surface flow measurements in rivers. *Journal of Hydraulic Research*, 59(4), 1-14.
- Carboneau, P., Dugdale, S., Breckon, T., Dietrich, J., Fonstad, M., Miyamoto, H. & Woodget, A. (2020). Adopting deep learning methods for airborne RGB fluvial scene classification. *Remote Sensing of Environment*, 251, 112107.
- Cassidy, M., Mélou, J., Quéau, Y., Lauze, F. & Durou, J. (2020). Refractive multi-view stereo. In 2020 International Conference on 3D Vision (3DV) (pp. 384-393). IEEE.
- Congalton, R. & Green, K. (2009). Assessing the Accuracy of Remotely Sensed Data: Principles and Practices. CRC Press, Boca Raton, Florida.
- Costa, J., Spicer, K., Cheng, R., Haeni, F., Melcher, N., Thurman, E., Plant, W. & Keller, W. (2000). Measuring stream discharge by non-contact methods: A proof-of-concept experiment. *Geophysical Research Letters*, 27(4), 553-556.
- Costa, J., Cheng, R., Haeni, F., Melcher, N., Spicer, K., Hayes, E., Plant, W., Hayes, K., Teague, C. & Barrick, D. (2006). Use of radars to monitor stream discharge by noncontact methods. *Water Resources Research*, 42(7).
- Detert, M. & Weitbrecht, V. (2013). User guide to gravelometric image analysis by BASEGRAIN. In: Advances in River Sediment Research, Proceedings of the 12th International Symposium on River Sedimentation ISRS 2013, (pp. 1789-1796). Kyoto, Japan. CRC Press.
- Detert, M., Johnson, E. & Weitbrecht, V. (2017). Proof-of-concept for low-cost and non-contact synoptic airborne river flow measurements. *International Journal of Remote Sensing*, 38(8-10), 2780-2807.
- Detert, M., Kadinski, L. & Weitbrecht, V. (2018). On the way to airborne gravelometry based on 3D spatial data derived from images. *International Journal of Sediment Research*, 33(1), 84-92.

- Detert, M., Cao, L. & Albayrak, I. (2019a). Airborne Image Velocimetry Measurements at the Hydropower Plant Schiffmühle on Limmat River, Switzerland. In Proceedings of the 2nd International Symposium and Exhibition on Hydro-Environment Sensors and Software, HydroSenSoft 2019 (pp. 211-217). IAHR.
- Detert, M., Rachelly, C., Brezzi, L. & Biggs, H. (2019b). Image-based 3D measurement of size, location, and orientation of gravel grains. Proceedings of the 11th river, coastal and estuarine morphodynamics symposium (RCEM 2019), Auckland, New Zealand.
- Detert, M. (2020). How to Avoid and Correct Biased Riverine Surface Image Velocimetry. Water Resources Research, 57(2), 1-17.
- Dietrich, J. (2017). Bathymetric Structure-from-Motion: extracting shallow stream bathymetry from multi-view stereo photogrammetry. Earth Surface Processes and Landforms, 42(2), 355-364.
- Dilbone, E., Legleiter, C., Alexander, J. & McElroy, B. (2018). Spectrally based bathymetric mapping of a dynamic, sand-bedded channel: Niobrara River, Nebraska, USA. River Research and Applications, 34(5), 430-441.
- Dolcetti, G., Alkmim, M., Cuenca, J., De Ryck, L. & Krynnin, A. (2021). Robust reconstruction of scattering surfaces using a linear microphone array. Journal of Sound and Vibration, 494, 115902.
- Dolcetti, G., Hortobágyi, B., Perks, M., Tait, S. & Dervilis, N. (2022). Using Non-contact Measurement of Water Surface Dynamics to Estimate River Discharge. (Draft manuscript)
- Dugdale, S. (2016). A practitioner's guide to thermal infrared remote sensing of rivers and streams: recent advances, precautions and considerations. Wiley Interdisciplinary Reviews: Water, 3(2), 251-268.
- Engel, F., Holmes Jr., R. & Oberg, K. (2021) Guidelines for the collection of video for LSPIV. <https://my.usgs.gov/confluence/pages/viewpage.action?pageId=546865360>
- EnviroColor (2021). Siera Red Mulch Dye Product Information. <https://www.envirocolor.com/product-page/sierra-red-mulch-dye-9-600-sq-ft-1-gallon>
- Faux, R., Lachowski, H., Maus, P., Torgersen, C. & Boyd, M. (2001). New approaches for monitoring stream temperature: airborne thermal infrared remote sensing. Project report. Remote Sensing Applications Laboratory, Salt Lake City, UT.
- Fedele, F., Benetazzo, A., Gallego, G., Shih, P. C., Yezzi, A., Barbariol, F. & Ardhui, F. (2013). Space–time measurements of oceanic sea states. Ocean Modelling, 70, 103-115.
- Feurer, D., Bailly, J., Puech, C., Le Coarer, Y. & Viau, A. (2008). Very-high-resolution mapping of river-immersed topography by remote sensing. Progress in Physical Geography, 32(4), 403-419.
- Fonstad, M., Dietrich, J., Courville, B., Jensen, J. & Carboneau, P. (2013). Topographic structure from motion: a new development in photogrammetric measurement. Earth surface processes and Landforms, 38(4), 421-430.
- Fountain, J. (2021). Using GPS and GPS compasses with ADCPs. USGS Webinar.
- Fujita, I. (2018) Principles of surface velocity gaugings. The 4<sup>th</sup> IAHR-WMO-IAHS Training Course on Stream Gauging. Lyon, France.
- Fujita, I., Notoya, Y., Tani, K. & Tateguchi, S. (2019). Efficient and accurate estimation of water surface velocity in STIV. Environmental Fluid Mechanics, 19(5), 1363-1378.

- Furukawa, Y. & Ponce, J. (2010). Accurate, dense, and robust multiview stereopsis. *IEEE transactions on pattern analysis and machine intelligence*, 32(8), 1362-1376.
- Gentile, V., Mróz, M., Spitoni, M., Lejot, J., Piégay, H. & Demarchi, L. (2016). Bathymetric mapping of shallow rivers with UAV hyperspectral data. In Proceedings of the Fifth International Conference on Telecommunications and Remote Sensing (ICTRS 2016), Milan, Italy.
- Gluckman, P. (2017). New Zealand's fresh waters: Values, state, trends and human impacts. Office of the Prime Minister's Chief Science Advisor. Wellington, New Zealand.
- Gorman, R. & Hicks, D.M. (2005). Directional wavelet analysis of inhomogeneity in the surface wave field from aerial laser scanning data. *Journal of physical oceanography*, 35(6), 949-963.
- Haddadchi, A. (2017). Review of suspended sediment measurement techniques. NIWA report 2017210CH, Christchurch New Zealand.
- Handcock, R., Torgersen, C., Cherkauer, K., Gillespie, A., Tockner, K., Faux, R. & Tan, J. (2012). Thermal infrared remote sensing of water temperature in riverine landscapes. In: *Fluvial Remote Sensing for Science and Management* (Eds: Carbonneau, P. & Piégay, H.), John Wiley & Sons, Chichester, UK.
- Hartley, R. & Zisserman, A. (2003). *Multiple view geometry in computer vision*. Cambridge University Press.
- Harvey, A., Gallagher, J. & Sengers, J. (1998). Revised formulation for the refractive index of water and steam as a function of wavelength, temperature and density. *Journal of Physical and Chemical Reference Data*, 27(4), 761-774.
- Hauet, A., Morlot, T. & Daubagnan, L. (2018) Velocity profile and depth-averaged to surface velocity in natural streams: A review over a large sample of rivers. In Proceedings of River Flow 2018, Lyon, France.
- Hicks, D.M. & Gomez, B. (2003). Sediment transport. In: *Tools in Fluvial Geomorphology*, Editors: Kondolf, G.M. & Piégay, H. John Wiley & Sons, Chichester, UK.
- Hicks, D.M., Shankar, U., Duncan, M., Rebuffe, M. & Aberle, J. (2006). Use of remote-sensing technology to assess impacts of hydro-operations on a large, braided, gravel-bed river: Waitaki River, New Zealand. In: *Braided rivers - process, deposits, ecology and management* (editors: Sambrook-Smith, G., Best J., Bristow, C. & Petts, G.). IAS Special Publication No. 36, Blackwell, 311-326.
- Hilldale, R. & Raff, D. (2008). Assessing the ability of airborne LiDAR to map river bathymetry. *Earth Surface Processes and Landforms*, 33(5), 773-783.
- Höfle, B., Vetter, M., Pfeifer, N., Mandlburger, G. & Stötter, J. (2009). Water surface mapping from airborne laser scanning using signal intensity and elevation data. *Earth Surface Processes and Landforms*, 34(12), 1635-1649.
- Holman, R., Plant, N. & Holland, T. (2013). cBathy: A robust algorithm for estimating nearshore bathymetry. *Journal of geophysical research: Oceans*, 118(5), 2595-2609.
- Hong, J., Guo, W., Wang, H. & Yeh, P. (2017). Estimating discharge in gravel-bed river using non-contact ground-penetrating and surface-velocity radars. *River Research and Applications*, 33(7), 1177-1190.
- Hydro Technology Institute (2022). Hydro-STIV Operation Manual. Osaka, Japan.

- Intel. (2012). USB 3.0 Radio Frequency Interference Impact on 2.4 GHz Wireless Devices. Intel White Paper.
- Islam, M., Yoshida, K., Nishiyama, S., Sakai, K. & Tsuda, T. (2022). Characterizing vegetated rivers using novel unmanned aerial vehicle-borne topo-bathymetric green lidar: Seasonal applications and challenges. *River Research and Applications*, 38(1), 44-58.
- ISO748. (2007). Hydrometry — Measurement of liquid flow in open channels using current-meters or floats. International Organization for Standardization.
- James, M., Chandler, J., Eltner, A., Fraser, C., Miller, P., Mills, J., Noble, T., Robson, S. & Lane, S. (2019). Guidelines on the use of structure-from-motion photogrammetry in geomorphic research. *Earth Surface Processes and Landforms*, 44(10), 2081-2084.
- Javernick, L., Brasington, J. & Caruso, B. (2014). Modeling the topography of shallow braided rivers using Structure-from-Motion photogrammetry. *Geomorphology*, 213, 166-182.
- Jay, S. & Guillaume, M. (2014). A novel maximum likelihood based method for mapping depth and water quality from hyperspectral remote-sensing data. *Remote sensing of environment*, 147, 121-132.
- Jin, T. & Liao, Q. (2019). Application of large-scale PIV in river surface turbulence measurements and water depth estimation. *Flow Measurement and Instrumentation*, 67, 142-152.
- Jodeau, M., Hauet, A., Le Coz, J., Faure, J. & Bodart, G. (2020). Fudaa-LSPIV Version 1.7.3 User Manual. EDF & INRAE, Lyon, France.
- Johnson, E. & Cowen, E. (2016). Remote monitoring of volumetric discharge employing bathymetry determined from surface turbulence metrics. *Water Resources Research*, 52(3), 2178-2193.
- Jowett, I. (1997). Instream flow methods: a comparison of approaches. *Regulated Rivers: Research & Management*, 13(2), 115-127.
- Kasvi, E., Salmela, J., Lotsari, E., Kumpula, T. & Lane, S. (2019). Comparison of remote sensing based approaches for mapping bathymetry of shallow, clear water rivers. *Geomorphology*, 333, 180-197.
- Kinzel, P., Legleiter, C. & Nelson, J. (2013). Mapping river bathymetry with a small footprint green LiDAR: applications and challenges 1. *JAWRA Journal of the American Water Resources Association*, 49(1), 183-204.
- Kinzel, P. & Legleiter, C. (2019). sUAS-based remote sensing of river discharge using thermal particle image velocimetry and bathymetric lidar. *Remote Sensing*, 11(19), 2317.
- Kinzel, P., Legleiter, C. & Grams, P. (2021). Field evaluation of a compact, polarizing topo-bathymetric lidar across a range of river conditions. *River Research and Applications*, 37(4), 531-543.
- Kondolf, G.M. & Lisle, T. (2003). Bed sediment measurement. In: Tools in Fluvial Geomorphology, Editors: Kondolf, G.M. & Piégay, H. John Wiley & Sons, Chichester, UK.
- Lane, J., Dawson, C., White, E. & Fulton, J. (2020). Non-contact measurement of river bathymetry using sUAS Radar: Recent developments and examples from the Northeastern United States. In proceedings of the Fifth International Conference on Engineering Geophysics (ICEG), Al Ain, United Arab Emirates.
- Le Coz, J., Hauet, A., Pierrefeu, G., Dramais, G. & Camenen, B. (2010). Performance of image-based velocimetry (LSPIV) applied to flash-flood discharge measurements in Mediterranean rivers. *Journal of hydrology*, 394(1-2), 42-52.

- Le Coz, J., Duby, P., Dramais, G., Camenen, B., Laronne, J., Zamler, D. & Zolezzi, G. (2011). Use of emerging non-intrusive techniques for flood discharge measurements. *5<sup>th</sup> International Conference on Flood Management*. Tokyo, Japan.
- Le Coz, J., Patalano, A., Collins, D., Guillén, N., García, C., Smart, G., Bind, J., Chiaverini, A., Boursicaud, R., Dramaïs, G. & Braud, I. (2016). Crowdsourced data for flood hydrology: Feedback from recent citizen science projects in Argentina, France and New Zealand. *Journal of Hydrology*, 541, 766-777.
- Le Coz, J., Renard, B., Vansuyt, V., Jodeau, M. & Huet, A. (2021). Estimating the uncertainty of video-based flow velocity and discharge measurements due to the conversion of field to image coordinates. *Hydrological Processes*, 35(5), 1-18.
- Legleiter, C., Roberts, D. & Lawrence, R. (2009). Spectrally based remote sensing of river bathymetry. *Earth Surface Processes and Landforms*, 34(8), 1039-1059.
- Legleiter, C. (2016). Inferring river bathymetry via image-to-depth quantile transformation (IDQT). *Water Resources Research*, 52(5), 3722-3741.
- Legleiter, C., Kinzel, P. & Nelson, J. (2017). Remote measurement of river discharge using thermal particle image velocimetry (PIV) and various sources of bathymetric information. *Journal of Hydrology*, 554, 490-506.
- Legleiter, C., Overstreet, B. & Kinzel, P. (2018). Sampling strategies to improve passive optical remote sensing of river bathymetry. *Remote Sensing*, 10(6), 935.
- Legleiter, C. & Fosness, R. (2019). Defining the limits of spectrally based bathymetric mapping on a large river. *Remote Sensing*, 11(6), 665.
- Legleiter, C. & Harrison, L. (2019). Remote sensing of river bathymetry: Evaluating a range of sensors, platforms, and algorithms on the upper Sacramento River, California, USA. *Water Resources Research*, 55(3), 2142-2169.
- Legleiter, C. (2021). The optical river bathymetry toolkit. *River Research and Applications*, 37(4), 555-568.
- Legleiter, C. & Kinzel, P. (2021). Depths Inferred from Velocities Estimated by Remote Sensing: A Flow Resistance Equation-Based Approach to Mapping Multiple River Attributes at the Reach Scale. *Remote Sensing*, 13(22), 4566.
- Lesser, M. & Mobley, C. (2007). Bathymetry, water optical properties, and benthic classification of coral reefs using hyperspectral remote sensing imagery. *Coral Reefs*, 26(4), 819-829.
- LeWinter, A., Pfennigbauer, M., Gadomski, P., Finnegan, D., Schwarz, R., Podoski, J. & Truong, M. (2018). Unmanned aircraft system-based lidar survey of structures above and below the water surface: Hilo Deep Draft Harbor Breakwater, Hawaii. In: *Lidar Remote Sensing for Environmental Monitoring XVI*. SPIE.
- Li, W., Liao, Q. & Ran, Q. (2019). Stereo-imaging LSPIV (SI-LSPIV) for 3D water surface reconstruction and discharge measurement in mountain river flows. *Journal of Hydrology*, 578, 124099.
- Lin, Y., Ho, H., Lee, T. & Chen, H. (2022). Application of Image Technique to Obtain Surface Velocity and Bed Elevation in Open-Channel Flow. *Water*, 14(12), 1895.
- Lyzenga, D. (1978). Passive remote sensing techniques for mapping water depth and bottom features. *Applied optics*, 17(3), 379-383.

- Lyzenga, D., Malinas, N. & Tanis, F. (2006). Multispectral bathymetry using a simple physically based algorithm. *IEEE Transactions on Geoscience and Remote Sensing*, 44(8), 2251-2259.
- Ma, S., Tao, Z., Yang, X., Yu, Y., Zhou, X. & Li, Z. (2013). Bathymetry retrieval from hyperspectral remote sensing data in optical-shallow water. *IEEE Transactions on Geoscience and Remote Sensing*, 52(2), 1205-1212.
- Mandlburger, G., Hauer, C., Wieser, M. & Pfeifer, N. (2015). Topo-bathymetric LiDAR for monitoring river morphodynamics and instream habitats—A case study at the Pielach River. *Remote Sensing*, 7(5), 6160-6195.
- Mandlburger, G., Pfennigbauer, M., Wieser, M., Riegl, U. & Pfeifer, N. (2016). Evaluation of a novel UAV-borne topo-bathymetric laser profiler. *The International Archives of Photogrammetry, Remote Sensing and Spatial Information Sciences*, 41, 933.
- Mandlburger, G. (2019). Through-water dense image matching for shallow water bathymetry. *Photogrammetric Engineering & Remote Sensing*, 85(6), 445-455.
- Mandlburger, G., Pfennigbauer, M., Schwarz, R., Flöry, S. & Nussbaumer, L. (2020). Concept and performance evaluation of a novel UAV-borne topo-bathymetric LiDAR sensor. *Remote Sensing*, 12(6), 986.
- Mandlburger, G., Kölle, M., Nübel, H. & Soergel, U. (2021). BathyNet: A deep neural network for water depth mapping from multispectral aerial images. *PFG—Journal of Photogrammetry, Remote Sensing and Geoinformation Science*, 89(2), 71-89.
- Manfreda, S., Dal Sasso, S., Pizarro, A. & Tauro, F. (2019). New Insights Offered by UAS for River Monitoring. In *Applications of Small Unmanned Aircraft Systems* (pp. 211-234). CRC Press.
- Mano, K., Sakai, K., Tachibana, K., Sakita, K. & Nishiyama, S. (2020). The measurement accuracy and measurement characteristics of green lidar drone. *International Archives of the Photogrammetry, Remote Sensing & Spatial Information Sciences*. Volume XLIII-B1-2020.
- Martínez-Carricando, P., Agüera-Vega, F., Carvajal-Ramírez, F., Mesas-Carrascosa, F., García-Ferrer, A. & Pérez-Porras, F. (2018). Assessment of UAV-photogrammetric mapping accuracy based on variation of ground control points. *International journal of applied earth observation and geoinformation*, 72, 1-10.
- Melcher, N., Costa, J., Haeni, F., Cheng, R., Thurman, E., Buursink, M., Spicer, K., Hayes, E., Plant, W., Keller, W. & Hayes, K. (2002). River discharge measurements by using helicopter-mounted radar. *Geophysical Research Letters*, 29(22), 41-1.
- MfE (2017). Clean water – 90% of rivers and lakes swimmable by 2040. Ministry for the Environment.
- Mobley, C. (1994). Light and water: radiative transfer in natural waters. Academic press. San Diego, California.
- Mobley, C. (1998). Hydrolight 4.0 users guide. Sequoia Scientific, Mercer Island, Washington.
- Mobley, C., Boss, E. & Roesler, C. (2022). The Ocean Optics Web Book. Funded by NASA. <https://www.oceanopticsbook.info/>
- Mulsow, C., Kenner, R., Bühler, Y., Stoffel, A. & Maas, H. (2018). Subaqueous digital elevation models from UAV-imagery. *International Archives of the Photogrammetry, Remote Sensing & Spatial Information Sciences*, 42(2).
- Muraro, F., Dolcetti, G., Nichols, A., Tait, S. & Horoshenkov, K. (2021). Free-surface behaviour of shallow turbulent flows. *Journal of Hydraulic Research*, 59(1), 1-20.

- Muste, M., Fujita, I. & Hauet, A. (2008). Large-scale particle image velocimetry for measurements in riverine environments. *Water resources research*, 44(4), 1-14.
- Okamoto, A. (1984). Orientation problem of two media photographs with curved boundary surfaces. *Photogrammetric engineering and remote sensing*, 50(3), 303-316.
- Overstreet, B. & Legleiter, C. (2017). Removing sun glint from optical remote sensing images of shallow rivers. *Earth Surface Processes and Landforms*, 42(2), 318-333.
- Pan, Z., Glennie, C., Legleiter, C. & Overstreet, B. (2015). Estimation of water depths and turbidity from hyperspectral imagery using support vector regression. *IEEE Geoscience and Remote Sensing Letters*, 12(10), 2165-2169.
- Patalano, A., García, C. & Rodríguez, A. (2017). Rectification of Image Velocity Results (RIVeR): A simple and user-friendly toolbox for large scale water surface Particle Image Velocimetry (PIV) and Particle Tracking Velocimetry (PTV). *Computers & Geosciences*, 109, 323-330.
- Peña-Haro, S., Lüthi, B., Lukes, R. & Carrel, M. (2020). Wind effect on image-based river surface velocity measurements. *EGU General Assembly 2020* (online).
- Pix4D. (2022). Pix4Dmapper 4.1 User Manual, Pix4D, Lausanne, Switzerland.
- Polcyn, F., Brown, W. & Sattinger, I. (1970). The measurement of water depth by remote sensing techniques. Report for the Spacecraft Oceanography Project, The University of Michigan, Ann Arbor, Michigan.
- Puleo, J., McKenna, T., Holland, K. & Calantoni, J. (2012). Quantifying riverine surface currents from time sequences of thermal infrared imagery. *Water Resources Research*, 48(1).
- Ran, Q., Li, W., Liao, Q., Tang, H. & Wang, M. (2016). Application of an automated LSPIV system in a mountainous stream for continuous flood flow measurements. *Hydrological Processes*, 30(17), 3014-3029.
- Randall, M. (2020). LSPIV or STIV and other tips. Presentation at NZHS Technical Workshop 2020, Tauranga, New Zealand.
- Randall, M. (2021). National Industry Guidelines for hydrometric monitoring – Part 11: Application of surface velocity methods for velocity and open channel discharge measurements. Bureau of Meteorology, Melbourne, Australia.
- Rantz, S. (1982). Measurement and computation of stream-flow: Measurement of stage and discharge. U.S. Geological Survey Water Supply Paper 2175.
- Rehmel, M. (2013). GPS best practices for moving-boat ADCP measurements. USGS Webinar.
- Resonon. (2021a). Spectronon User Manual V3.4.0. Resonon Inc, Bozeman, Montana.
- Resonon. (2021b). Airborne User Manual V6.3. Resonon Inc, Bozeman, Montana.
- Richards, J. (2013). Remote sensing digital image analysis (5th Edition). Springer.
- Rinner, K. (1969). Two Media Photogrammetry. *Photogrammetric Engineering*, Vol. 35, pp. 275-282.
- Rossi, L., Mammi, I. & Pelliccia, F. (2020). UAV-derived multispectral bathymetry. *Remote Sensing*, 12(23), 3897.
- Schweitzer, S. & Cowen, E. (2021). Instantaneous River-Wide Water Surface Velocity Field Measurements at Centimeter Scales Using Infrared Quantitative Image Velocimetry. *Water Resources Research*, 57(8), 1-28.

- Skarlatos, D. & Agrafiotis, P. (2018). A novel iterative water refraction correction algorithm for use in structure from motion photogrammetric pipeline. *Journal of Marine Science and Engineering*, 6(3), 77.
- Smart, G. & Biggs, H. (2020). Remote gauging of open channel flow: Estimation of depth averaged velocity from surface velocity and turbulence. In Proc. River Flow (Vol. 2020, pp. 1-10).
- Smart, G. (2021a). Superficial Flow Measurement. NZHS Technical Workshop. Christchurch, New Zealand.
- Smart, G. (2021b). Is delta alpha uniform charlie? International Surface Velocimetry Workshop. Hull, UK.
- Smart, G. (2022). A base for the log law and Von Karman's constant problem. *Journal of Hydraulic Research*, [In Press].
- Spicer, K., Costa, J. & Placzek, G. (1997). Measuring flood discharge in unstable stream channels using ground-penetrating radar. *Geology*, 25(5), 423-426.
- Štroner, M., Urban, R., Reindl, T., Seidl, J. & Brouček, J. (2020). Evaluation of the Georeferencing Accuracy of a Photogrammetric Model Using a Quadrocopter with Onboard GNSS RTK. *Sensors*, 20(8), 2318.
- Tewinkel, G. (1963). Water depths from aerial photographs. *Photogrammetric Engineering*, 29(6), 1037-1042.
- Thielicke, W. & Stamhuis, E. (2014). PIVlab—towards user-friendly, affordable and accurate digital particle image velocimetry in MATLAB. *Journal of open research software*, 2(1).
- Thielicke, W. & Sonntag, R. (2021). Particle Image Velocimetry for MATLAB: Accuracy and enhanced algorithms in PIVlab. *Journal of Open Research Software*, 9(1).
- Thormählen, I., Straub, J. & Grigull, U. (1985). Refractive index of water and its dependence on wavelength, temperature, and density. *Journal of physical and chemical reference data*, 14(4), 933-945.
- Tomaštík, J., Mokroš, M., Surový, P., Grznárová, A. & Merganič, J. (2019). UAV RTK/PPK Method—An Optimal Solution for Mapping Inaccessible Forested Areas?. *Remote sensing*, 11(6), 721.
- Ventura, D. (2020). Coastal zone mapping with the world's first airborne multibeam bathymetric lidar mapping system. In: *Hydrographische Nachrichten* 115. Rostock: Deutsche Hydrographische Gesellschaft. 48-53
- Wagner, C. & Mueller, D. (2011). Comparison of bottom-track to global positioning system referenced discharges measured using an acoustic Doppler current profiler. *Journal of Hydrology*, 401(3-4), 250-258.
- Wang, D., Xing, S., He, Y., Yu, J., Xu, Q. & Li, P. (2022). Evaluation of a New Lightweight UAV-Borne Topo-Bathymetric LiDAR for Shallow Water Bathymetry and Object Detection. *Sensors*, 22(4), 1379.
- Wawrzyniak, V., Piégay, H., Allemand, P., Vaudor, L. & Grandjean, P. (2013). Prediction of water temperature heterogeneity of braided rivers using very high resolution thermal infrared (TIR) images. *International Journal of Remote Sensing*, 34(13), 4812-4831.
- Weitbrecht, V., Kühn, G. & Jirka, G.H. (2002). Large scale PIV-measurements at the surface of shallow water flows. *Flow Measurement and Instrumentation*, 13(5-6), 237-245.

- Welber, M., Le Coz, J., Laronne, J., Zolezzi, G., Zamler, D., Dramais, G., Hauet, A. & Salvaro, M. (2016). Field assessment of noncontact stream gauging using portable surface velocity radars (SVR). *Water Resources Research*, 52(2), 1108-1126.
- Westaway, R., Lane, S. & Hicks, D.M. (2000). The development of an automated correction procedure for digital photogrammetry for the study of wide, shallow, gravel-bed rivers. *Earth Surface Processes and Landforms*, 25(2), 209-226.
- Westaway, R., Lane, S. & Hicks, D.M. (2001). Remote sensing of clear-water, shallow, gravel-bed rivers using digital photogrammetry. *Photogrammetric Engineering and Remote Sensing*, 67(11), 1271-1282.
- Westaway, R., Lane, S. & Hicks, D.M. (2003). Remote survey of large-scale braided, gravel-bed rivers using digital photogrammetry and image analysis. *International Journal of Remote Sensing*, 24(4), 795-815.
- Westoby, M., Brasington, J., Glasser, N., Hambrey, M. & Reynolds, J. (2012). ‘Structure-from-Motion’ photogrammetry: A low-cost, effective tool for geoscience applications. *Geomorphology*, 179, 300-314.
- Winterbottom, S. & Gilvear, D. (1997). Quantification of channel bed morphology in gravel-bed rivers using airborne multispectral imagery and aerial photography. *Regulated Rivers: Research & Management*, 13(6), 489-499.
- Woodget, A., Dietrich, J. & Wilson, R. (2019). Quantifying below-water fluvial geomorphic change: The implications of refraction correction, water surface elevations, and spatially variable error. *Remote Sensing*, 11(20), 2415.

## Glossary

ADCP	Acoustic Doppler Current Profiler.
Agisoft Metashape	SfM software for creating georeferenced orthomosaics and DEMs from input imagery.
Bathymetry	Underwater equivalent to topography (essentially a map of depth).
CAA	Civil Aviation Authority (the governing body for aircraft and drone regulations in New Zealand).
CAD	Computer Aided Design.
DEM	Digital Elevation Model.
Discharge	The volume of water flowing down a channel each second (also known as volumetric flow rate or volumetric discharge).
Drone	Synonym for: Unmanned Aerial Vehicle (UAV), Unmanned Aerial System (UAS), Uncrewed Aerial Vehicle (UAV), and Remotely Piloted Aircraft System (RPAS). Drone is used throughout this user guide for consistency and simplicity.
DSM	Digital Surface Model. Provides the elevation of the top of the landscape (i.e. tree canopies, water surface, and land) as opposed to a DEM which typically provides ground elevation underneath vegetation. In cases where the ground is mapped directly DEMs and DSMs are equivalent.
EFL	Effective Focal Length.
EMI	Electro-Magnetic Interference.
EXIF	Exchangeable Image File Format. This is the supplementary information and ‘tags’ that are attached to an image (such as GPS data). Some of this information can be obtained by right clicking an image in windows explorer (for example) and viewing image properties. However, the full suite of available EXIF information needs to be extracted using other software such as MATLAB (see Appendix A).
FoV	Field of View.
FPS	Frames Per Second.
FPV	First Person View.
FTV	Feature Tracking Velocimetry.
FUDAA LSPIV	Software for processing surface velocimetry videos using LSPIV.
GCP	Ground Control Point.
Georeferenced Orthomosaic	2D photo map that is accurately scaled and in real world coordinates. Georeferenced orthomosaics can then be opened in software such as ArcMap, ENVI, QGIS, or MATLAB for image classification and further processing.
Gimbal	Device under a drone that holds a camera and maintains its orientation (usually nadir/vertical) independently of the drone orientation. This avoids changes in camera orientation as the drone flies, or in response to atmospheric turbulence.
GNSS	Global Navigation Satellite System.
GPR	Ground Penetrating Radar.
GPS	Global Positioning System.
HSV	Hue Saturation Value colour space for processing RGB imagery.
HydroSTIV	Software for processing surface velocimetry videos using STIV or PTV.
IMU	Inertial Measurement Unit (used to measure orientation and accelerations).
LiDAR	Light Detection And Ranging is used to resolve digital elevation models of terrain at high resolution. Terrestrial LiDAR systems typically use infrared light (typical

	wavelength of 1064 nm), whereas bathymetric LiDAR systems use green light (typical wavelength of 532 nm, which is frequency doubled from 1064 nm). Bathymetric LiDAR systems are constantly improving, however their high price of >\$300k NZD, limits their uptake and deployment.
LiPo	Lithium Polymer (battery type).
LSPIV	Large Scale Particle Image Velocimetry.
MBIE	Ministry of Business, Innovation and Employment (Government Agency in New Zealand).
MfE	Ministry for the Environment (Government Agency in New Zealand).
MVS	Multi View Stereo algorithms (Furukawa & Ponce, 2010) are used when generating dense point clouds in SfM photogrammetry and for excluding moving objects.
Nadir	Vertically oriented (i.e. parallel with the force of gravity). Nadir imagery is captured from a camera in a gimbal under an aerial vehicle to make maps.
NIWA	National Institute of Water and Atmospheric Research.
Orthomosaic	2D photo map usually created by SfM software.
PCB	Printed Circuit Board.
Pix4D	SfM software for creating georeferenced orthomosaics and DEMs from input imagery.
Physical habitat	Physical habitat is the local combination of depth, velocity, and substrate (Jowett, 1997).
PIV	Particle Image Velocimetry (used to evaluate velocities from the motion of groups of tracer particles).
POEM	Pressure Operated Electronic Meter (for measuring depth and velocity).
PPK GPS	Post Processed Kinematic Global Positioning System.
PTV	Particle Tracking Velocimetry (used to evaluate velocities from the motion of individual tracer particles).
PWM	Pulse Wave Modulation.
QC	Quality Control.
QRev	Software for processing ADCP data.
RAM	Random Access Memory.
Raster	A rectangular grid of data (i.e. image matrices) compared to point or vector data.
RC	Remote Control.
RGB	Red Green Blue. This is the standard imagery collected by digital cameras, where sensor response covers three broad (and usually overlapping) spectral bands.
RIVeR	Rectification of Image Velocity Results. Software from the USGS for performing LSPIV.
RIVeR-STIV	Rectification of Image Velocity Results STIV. Software from the USGS for performing STIV.
ROI	Region Of Interest (usually a polygon from which training or validation pixels are extracted).
RTK GPS	Real Time Kinematic Global Positioning System.
SDK	Software Development Kit.
SfM	Structure from Motion. This is a technique where multiview stereo algorithms are used to process many overlapping images (from different viewpoints) to create

	point clouds (Hartley & Zisserman, 2003), digital elevation models, and georeferenced orthomosaics. The recommended software packages are Agisoft Metashape or Pix4D.
SSD	Solid State Drive.
Stereoscopic	Using two or more cameras to resolve depth of field in images (i.e. stereovision).
STIV	Space Time Image Velocimetry.
SVR	Surface Velocity Radar.
SxS Pro	Section by Section Pro is a software for measuring discharge with Teledyne RDI ADCPs using sections and is commonly used for flood gauging with moving bed.
Turbid	Murky, or not visually clear due to suspended sediment.
UAS	Unmanned Aerial System, or Uncrewed Aerial System (see ‘Drone’).
UAV	Unmanned Aerial Vehicle, or Uncrewed Aerial Vehicle (see ‘Drone’).

## Appendix A: Drone flow toolbox – GitHub repository

The ‘drone flow’ project has released a range of files through a GitHub repository as part of the open source ‘drone flow’ toolbox. This release is designed to accelerate the development and uptake of ‘drone flow’ technology in New Zealand and globally. All files are released without any warranty or guarantees and are intended for educational purposes only to accelerate the development of similar systems.

Repository address: <https://github.com/HamishBiggs/DroneFlow>

### The repository contains:

- Useful MATLAB functions and scripts (Appendix A – below).
  - Some code that was developed by collaborators is proprietary and could not be released.
- Acquisition software for stereoscopic camera and image capture settings (Appendix B).
- Cross sections from moving boat ADCP gaugings (Appendix C).
- CAD files for ‘drone flow’ hardware (Appendix D).
- A camera and flight parameter calculator (Appendix E).
- Supplementary files (e.g. GCP templates).

### Provided functions and classes:

'bigGKClean.m', 'cellStrMatrix2csvFaster.m', 'checkGCPLocations.m',  
'copyFilesWithRegularExpression.m', 'createPolygonBinsFromOrthogonalUnitVectors.m',  
'CrossSectionsFromQRevR2019b.m', 'CrossSectionsFromRTKGPSBathy.m', 'despikeDataBasic.m',  
'despikingClass.m', 'DF\_Cal.m', 'DF\_Cam.m', 'dischargeFromSurfaceVelocitiesAndCrossSection.m',  
'discreteSmoothFit.m', 'discreteSmoothFitFixedEnds.m', 'drawShapeFileOfPIVBoundaries.m',  
'expandNaNRegions.m', 'extractColumn.m', 'extractFrames.m', 'fixFileNumbering.m',  
'generateAveragingKernel.m', 'generateCalibrationTargetImage2.m', 'genericFigureScaling.m',  
'genericFigureScaling2.m', 'getExifData.m', 'getImageShiftMono.m', 'getPreviousDir.m',  
'glintMaskScriptRGB.m', 'glintMaskScriptSingleChannelMultispec.m', 'magicWandDelete.m',  
'makeGroundControlPointsBlueYellow.m', 'makeGroundControlPointsBlueYellowCanvas.m',  
'makeGroundControlPointsNumOnly.m', 'mergeImagesIntoFolder.m', 'namesOfAllSubDirs.m',  
'polygons2MaskFast.m', 'processGPRCrossSection.m', 'readTextFileGeneric.m', 'saveFiguresPNG.m',  
'saveFiguresPNGNoRescaling.m', 'smooth1D.m', 'TDC.m', 'vectorIntersection.m',  
'videoStabilisation.m', 'writeCurrentDir.m'.

### Included external files and functions:

Filenames:	Attribution:	Website:	Why included?
exiftool.exe	Phil Harvey	<a href="https://exiftool.org/">https://exiftool.org/</a>	exiftool.exe is needed for extraction of exif data from images with ‘getExifData.m’. The 2018 version is provided, since it is the version that getExifData.m has been extensively tested and used with.
insidepoly.m	Bruno Luong	<a href="https://www.mathworks.com/matlabcentral/fileexchange/27840-2d-polygon-interior-detection">https://www.mathworks.com/matlabcentral/fileexchange/27840-2d-polygon-interior-detection</a>	Much faster detection of points that are within polygons with mex files: insidepoly_dbengine_mexw64 insidepoly_sgengine_mexw64
xcorr2_fft.m	Alessandro Masullo	<a href="https://www.mathworks.com/matlabcentral/fileexchange">https://www.mathworks.com/matlabcentral/fileexchange</a>	Much faster than MATLABs inbuilt xcorr2.m see below for discussion.

		<a href="#">change/53570-xcorr2_fft-a-b</a>	
--	--	---	--

### File locations:

The files above are contained in: ‘Matlab general code released.zip’. The files for extracting bathymetry from moving boat ADCP cross sections (see Section 4.7.1 and Appendix C) are contained in: ‘Matlab Cross Sections from ADCPs and QRev.zip’.

### Code not included:

LSPIV and STIV code is not provided, since excellent implementations that are easy to use already exist (e.g. Fudaa LSPIV, River, River STIV, or Hydro STIV). In MATLAB, PIVLab (Thielicke & Stamhuis, 2014; Thielicke & Sonntag, 2021) provides a good starting point for LSPIV. Alternatively, custom PIV algorithms can be easily developed. The function ‘xcorr2\_fft.m’ developed by Alessandro Masullo has been included in the code above, and is highly recommended over MATLAB’s inbuilt ‘xcorr2.m’ and ‘conv2.m’, which are related by  $xcorr2(a,b) = conv2(a, rot90(conj(b),2))$ . During tests aligning bands of multispectral camera imagery ‘xcorr2\_fft.m’ was 122x faster than ‘xcorr2.m’, with speed gains particularly prominent for large matrices. There are also parallel and GPU implementations of 2D cross correlation that would be worth exploring for custom LSPIV algorithm development, such as ‘GPUConv2.m’<sup>35</sup> from Dirk-Jan Kroon and ‘cudaconv.m’<sup>36</sup> from Alexander Huth.

MATLAB also contains powerful functionality in the Computer Vision Toolbox<sup>37</sup> for feature detection and matching. This has wide ranging applications including: camera calibration; feature tracking; velocimetry (Cao *et al.*, 2020); image/video stabilisation; orthorectification; and 3D scene reconstruction. 3D reconstruction of static scenes can be performed using Structure from Motion (SfM) techniques where the camera moves in space, whereas 3D reconstruction of dynamic scenes can be undertaken using synchronous stereoscopic (or multiview) images. For feature matching applications, the use of Oriented Robust and Brief (ORB) features<sup>38</sup> is recommended as a good starting point for both speed and accuracy.

---

<sup>35</sup> <https://www.mathworks.com/matlabcentral/fileexchange/29648-gpuconv2>

<sup>36</sup> <https://www.mathworks.com/matlabcentral/fileexchange/20220-fast-2d-gpu-based-convolution>

<sup>37</sup> [https://www.mathworks.com/help/vision/referencelist.html?type=function&s\\_tid=CRUX\\_topnav](https://www.mathworks.com/help/vision/referencelist.html?type=function&s_tid=CRUX_topnav)

<sup>38</sup> <https://www.mathworks.com/help/vision/ref/detectorbfeatures.html>

## **Appendix B: Stereoscopic camera acquisition software and config settings for BFS-U3-51S5C-C cameras**

To accelerate parallel developments of similar stereoscopic cameras by others, we have also released our image acquisition software for the stereoscopic camera (i.e. 2x BFS-U3-51S5C-C) cameras through the ‘drone flow’ toolbox (<https://github.com/HamishBiggs/DroneFlow>).

### **Files:**

- ‘Drone\_flow\_stereoscopic\_camera\_acquisition.zip’
- ‘stereoscopicCameraAcquisitionConfig.txt’

The code is released without any warranty or guarantees and is intended for educational purposes only to accelerate developments by others who are using similar cameras and the Spinnaker SDK.

The settings that we use for camera acquisition are:

```
// s/n of primary camera
primary_camera=18383707

// s/n of secondary camera
secondary_camera=18383709

// path for saving images (remember \ at the end). //Note: an extra subdirectory with the current system time will be created within this directory.
image_path=C:\Drone_flow\images\

// image file format: 0 = RAW, 1 = JPG, 2=PNG //Note: PNG has very very slow write speed and is not recommended.
image_type=0

// Pixel format type: see Blackfly S Technical Reference for details
pixel_format=RGB8Packed

// capture frequency in Hz (10 Hz is the max recommended stable frame rate for stereoscopic RGB full frame)
capture_frequency=10

// exposure time in us
exposure_time=0

// auto exposure setting: 0 = off, 1 = once, 2 = continuous
exposure_auto=2

// auto exposure lighting mode: 0 = autodetect, 1 = front, 2 = back, 3 = normal //Note: do not use 'autodetect' causes error.
Recommend 'normal'.
auto_elm=3

// auto exposure light metering mode: 0 = average, 1 = spot, 2 = partial, 3 = centre weighted, 4 = histogram peak
auto_emm=0

// auto exposure time lower limit in us
auto_etll=50

// auto exposure time upper limit in us (1/1000 seconds for limited motion blur) //WARNING: When testing in low light this
needs to be increased, then decreased again for field deployment.
auto_etul=1000
```

```

// auto exposure control priority: 0 = gain, 1 = exposure time. //Note: In the field use 1 for exposure time. In the office (low
light) gain is more appropriate.
auto_ecp=1

// Auto Gain setting: 0 = off, 1 = once, 2 = continuous
gain_auto=2

//Auto white balance setting: 0 = off, 1 = once, 2 = continuous //Recommend 0 //Note: when continuous the response of the
cameras can be quite different and they diverge in colour and brightness...
auto_wb=0

//Defined white balance if auto white balance off. Red:Green x1000 for integer input//Recommend 0.54x1000=540
manual_wb_rg=540;

//Defined white balance if auto white balance off. Blue:Green x1000 for integer input//Recommend 1.66x1000=1660
manual_wb_bg=1660;

//Auto exposure grey value auto: 0 = off, 1 = continuous
//For manual control, set Target Grey Value Auto to Continuous and then set the desired image average in Target Grey Value.
This value is a percentage of the maximum pixel value.
//For automatic control, set Target Grey Value Auto to Off. The target image average is then automatically determined
according to user-defined AE modes and other AE features.
auto_GV_on=1;

//Auto exposure target grey value for continuous mode: Expressed as an integer percentage. I.e. 40%.
target_GV=40;

//Gamma correction on: 0 = off, 1 = on
gamma_correction_on=1

//Gamma correction value: x 10000 for integer output. I.e. 0.4545x10000=4545 (where 0.4545 is recommended for sRGB).
gamma_value=4545;

// X,Y pixel decimation: set to 1 or 2. //Note1: These cameras can't support decimation more than 2. //Note2: There are also
binning methods for averaging pixels available.
x_decimation=1
y_decimation=1

// Width, height of Region of Interest (2448 × 2048 is max)
x_roi=2448
y_roi=2048

// X,Y coordinates of top left corner of Region of Interest. //Note: Image origin is top left.
x_offset=0
y_offset=0
trigger_port=COM7

//Runtime minor bugs: Setting Auto Exposure Lighting Mode to 'autodetect' causes errors. Recommend 'normal'.

```

## **Appendix C: Cross sections from moving boat ADCP gaugings**

Code for extracting cross sections from moving boat ADCP gaugings has also been provided through the ‘drone flow’ toolbox.

Repository address: <https://github.com/HamishBiggs/DroneFlow>

File to download: ‘Matlab Cross Sections from ADCPs and QRev.zip’

For MATLAB programmers the file ‘CrossSectionsFromQRevR2019b.m’ has been provided.

For those who are not MATLAB programmers (or don’t have access to MATLAB software), a precompiled file ‘CrossSectionsFromQRevR2019b.exe’ has been provided for use with the free MATLAB runtime environment.

First, install MATLAB runtime environment R2019b (9.7) from:

<https://www.mathworks.com/products/compiler/matlab-runtime.html>

Then run: ‘CrossSectionsFromQRevR2019b.exe’

Supplementary files are provided in ‘Matlab Cross Sections from ADCPs and QRev.zip’, such as example input data from QRev, example inputs to the command line (just answering questions), and example output plots and cross sections.

### **Workflow for extracting cross sections from moving boat ADCP gaugings:**

- Process the moving boat ADCP gauging in QRev and check the transects that should be included in bathymetry extraction for the cross section.
- Save the QRev file (i.e. a .mat file).
- Run ‘CrossSectionsFromQRevR2019b.exe’.
- Select the .mat file saved by QRev.
- A terminal dialogue box will pop up showing the progress of data processing and providing options for the user to respond to.
- An example of the terminal dialogue is provided below.
- If figures of cross sections obscure the terminal window, navigate back to it on the taskbar.
- The code works with data from the latest versions of QRev (i.e. QRev 4.29 and QRevInt 1.18 at the time of writing) and should also work with data from most older versions of QRev.
- If there are any errors/bugs running this code please contact [Hamish.Biggs@niwa.co.nz](mailto:Hamish.Biggs@niwa.co.nz) as there may be variations in the input data that have not been previously encountered and need to be handled as special cases.

### **Example of the terminal dialogue during data processing:**

```
Running CrossSectionsFromQRev.m
Processed transect 1 of 6
Processed transect 2 of 6
Processed transect 3 of 6
Processed transect 4 of 6
Processed transect 5 of 6
Processed transect 6 of 6
```

Type distance reference to use, input options: VTG or GGA or BT (VTG is recommended). Then press enter.

VTG<sup>39</sup>

Select the cross sections to use for averaging

- 1 = 201103\_Tekapo Canal Gauging\_1\_000.PD0
- 2 = 201103\_Tekapo Canal Gauging\_1\_001.PD0
- 3 = 201103\_Tekapo Canal Gauging\_1\_002.PD0
- 4 = 201103\_Tekapo Canal Gauging\_1\_003.PD0
- 5 = 201103\_Tekapo Canal Gauging\_1\_004.PD0
- 6 = 201103\_Tekapo Canal Gauging\_1\_005.PD0

Type the cross section indices to use. For multiple indices, use a comma separated list (e.g. 1 or 1,3,4,6 etc). Then press enter.

1,2,3,4,5,6

Use user input cross section width? Type: Y to proceed, or N to use average width from cross section reference that was previously selected (e.g. VTG). Then press enter.

N<sup>40</sup>

Processing selected cross sections, from VTG data

Rescaling cross sections based on average VTG width

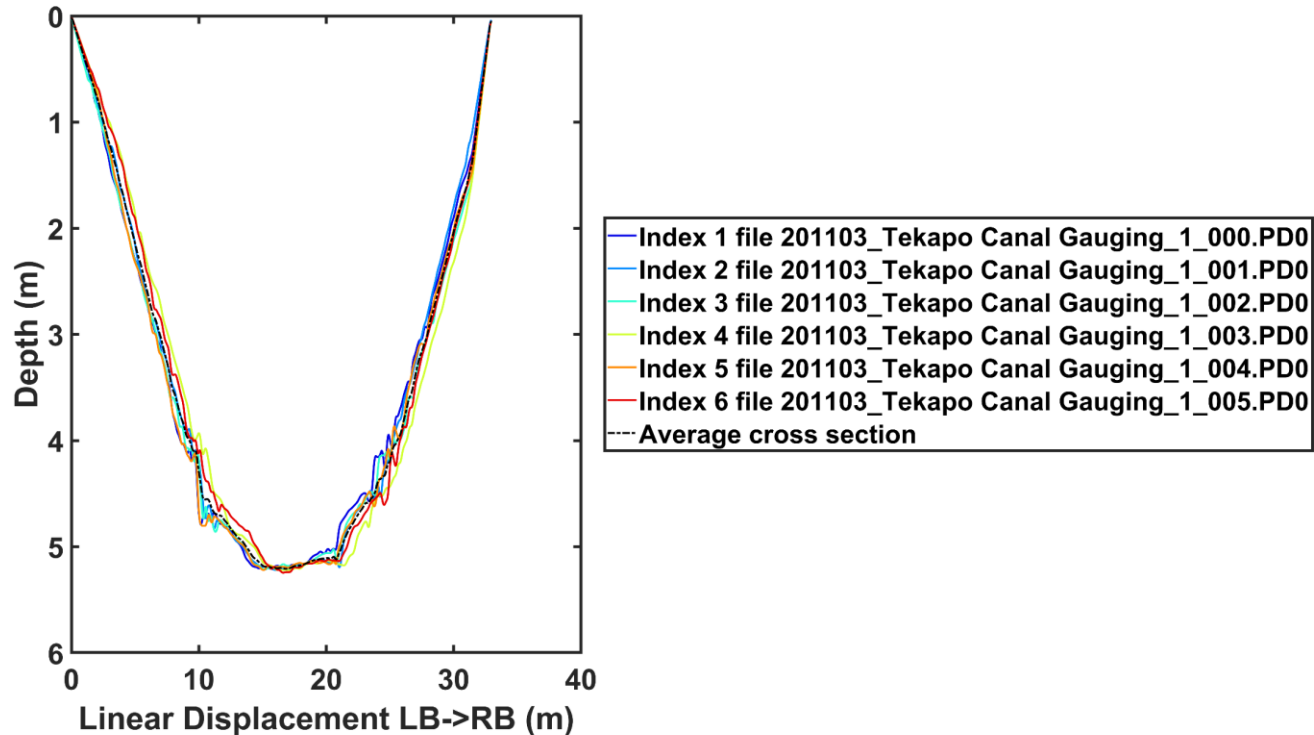


Figure C.1: A figure showing all of the selected transects will appear. Check how well the selected transects correspond, and if there are any outliers. If there are outliers, then reselect the transects to be used for the final average output cross section.

<sup>39</sup> If GPS data is not available, then Bottom Track (BT) will be selected by default.

<sup>40</sup> This enables users to manually enter cross section width if needed. This is useful if cross section width has been measured accurately with RTK GPS, or if the moving boat transects were on a diagonal path across the river, and total width needs to be corrected for. In general, this is not needed for most deployments and displacement from VTG (or BT without moving bed) is usually quite accurate (particularly when averaging multiple transects).

Happy with cross section processing? Ready to output cross section data? Type: Y to proceed, or N to change selection options.

N

Type distance reference to use, input options: VTG or GGA or BT (VTG is recommended). Then press enter.

VTG

Select the cross sections to use for averaging

- 1 = 201103\_Tekapo Canal Gauging\_1\_000.PD0
- 2 = 201103\_Tekapo Canal Gauging\_1\_001.PD0
- 3 = 201103\_Tekapo Canal Gauging\_1\_002.PD0
- 4 = 201103\_Tekapo Canal Gauging\_1\_003.PD0
- 5 = 201103\_Tekapo Canal Gauging\_1\_004.PD0
- 6 = 201103\_Tekapo Canal Gauging\_1\_005.PD0

Type the cross section indices to use. For multiple indices, use a comma separated list (e.g. 1 or 1,3,4,6 etc). Then press enter.

1,2,3,5

Use user input cross section width? Type: Y to proceed, or N to use average width from cross section reference that was previously selected (e.g. VTG). Then press enter.

N

Processing selected cross sections, from VTG data

Rescaling cross sections based on average VTG width

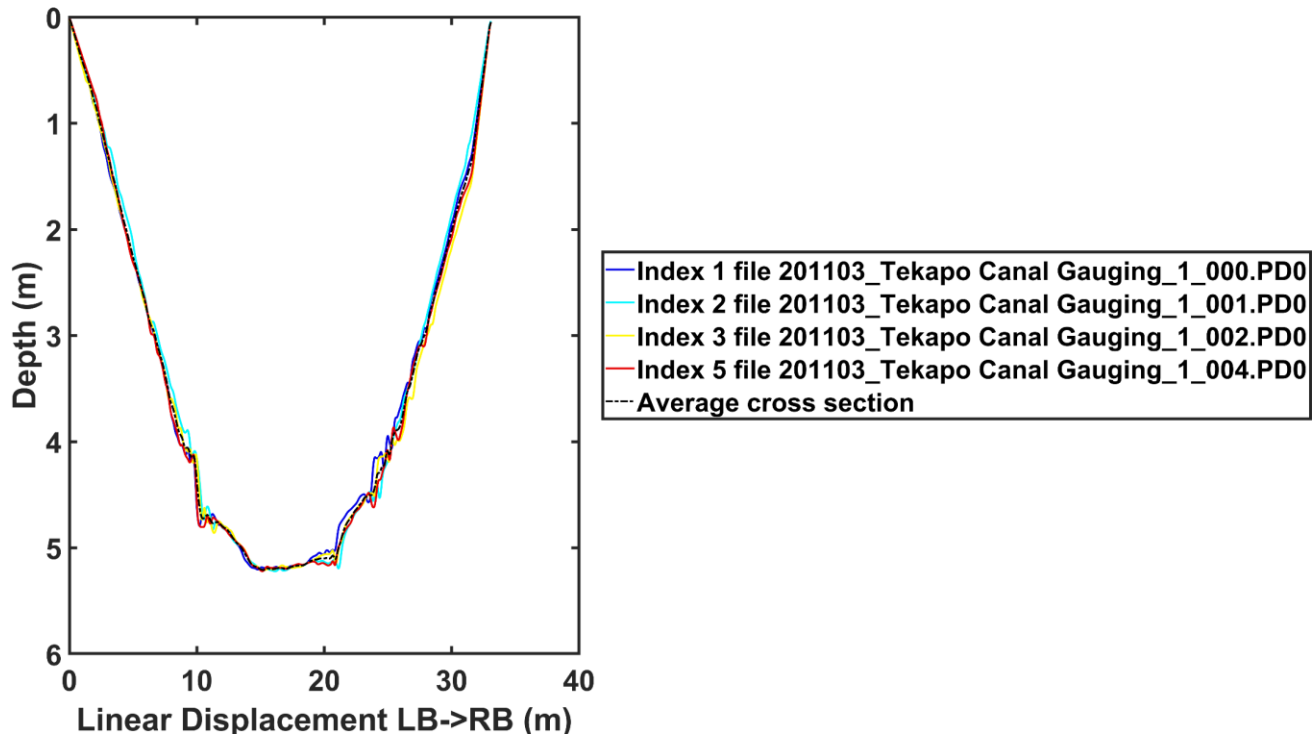


Figure C.2: Reselected transects without outliers (i.e. without Index 4 and 6). The average cross section is now ready for export.

Happy with cross section processing? Ready to output cross section data? Type: Y to proceed, or N to change selection options.

Y

Type the cross section water level in meters if manually measured (i.e. with GPS). It is usually set to zero for orthorectified drone imagery, but should be measured in real world coordinates for oblique imagery with ground control points. If a water level staff is used, then real world water level can be calculated from a GPS measurement of the staff zero point.  
Then press enter.

0

Saving the QRev data structure as C:\XS\_Example\2022\_05\_11\_12\_27\_42\_QRevData.mat

Saving the individual cross sections

Saving the average cross section

Would you also like to save all the figures as images (useful for QC)? Type: Y to save figures, or N if figures are not needed.

N

CrossSectionsFromQRevR2019b has completed processing. Please close the application.

## Appendix D: CAD files of ‘drone flow’ hardware

CAD files for hardware developed during the ‘drone flow’ project are also provided through the GitHub repository <https://github.com/HamishBiggs/DroneFlow>.

Which contains the following zip files:

- ‘ADCP Benthic Lander CAD Files.zip’
- ‘Stereoscopic Camera Chassis CAD files.zip’
- ‘Stereoscopic Camera Frame and GPS antennas CAD Files.zip’
- ‘Tracer Particle Distribution System CAD Files.zip’

Some proprietary files from 3<sup>rd</sup> parties that are used in assemblies could not be provided, however the key files needed for fabrication (i.e. CNC machining aluminium) or 3D printing are provided.

An overview of the CAD file assemblies are shown in Figure D.1 to Figure D.5:

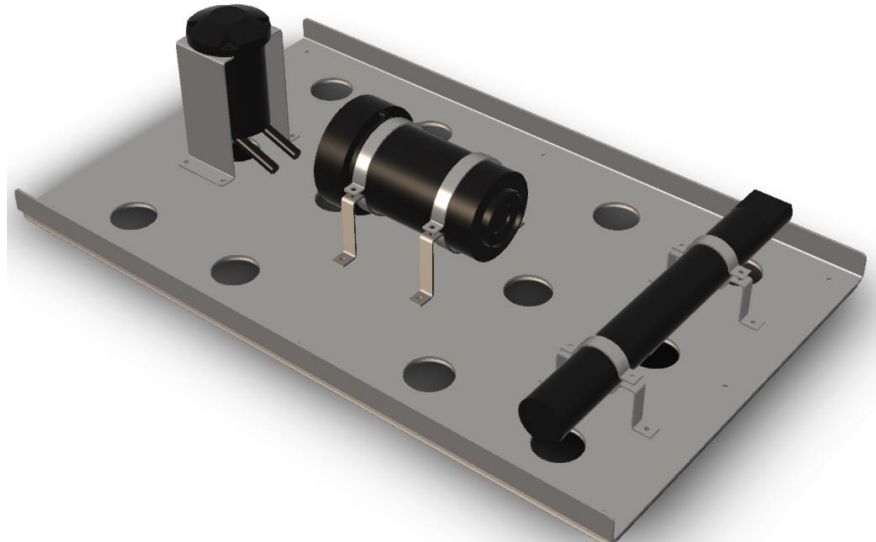


Figure D.1: ADCP benthic lander with Nortek Signature and Nortek Aquadopp.

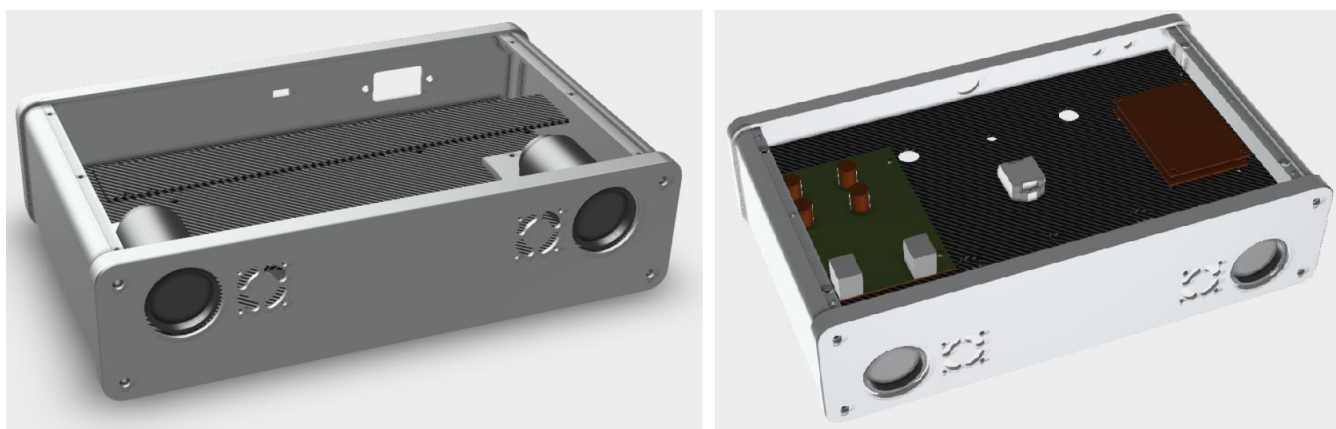


Figure D.2: Stereoscopic camera chassis top (left) and bottom (right).

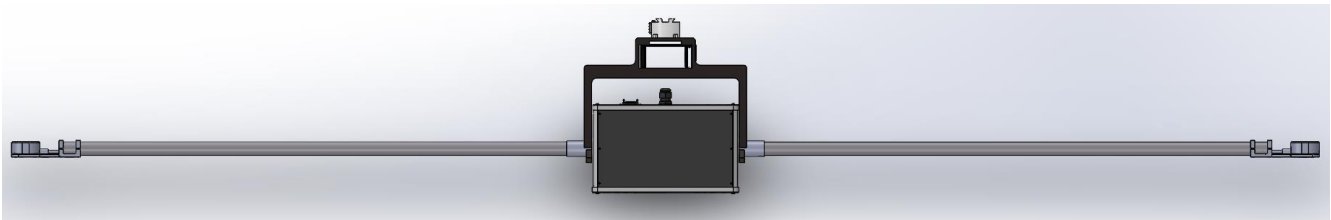


Figure D.3: Stereoscopic camera full assembly with mounting brackets and GPS antenna booms.

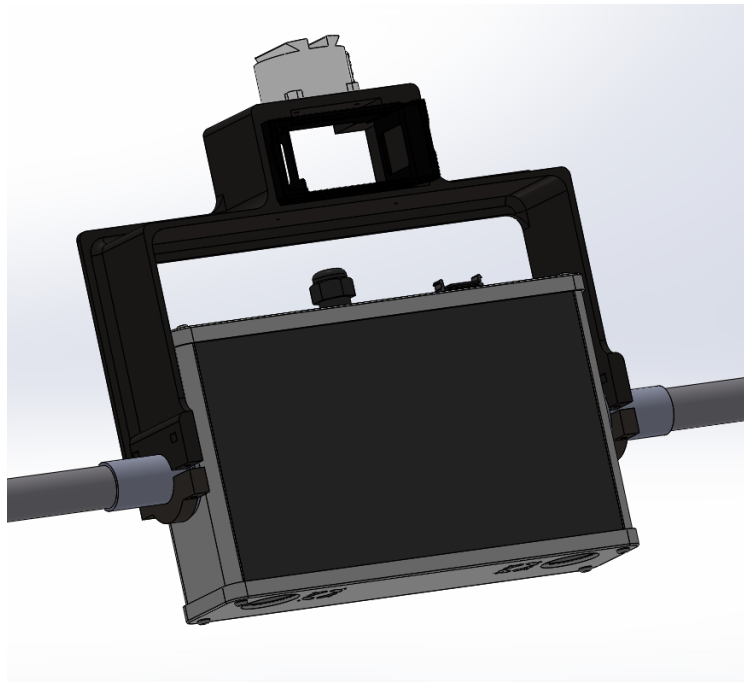


Figure D.4: Stereoscopic camera frame, zoomed oblique view.



Figure D.5: The CAD files provided also contain mounting brackets for GPS antennas (left), mounting brackets for the tracer particle distribution system (centre) and various saddle clamps (right). Most of these components are well suited to 3D printing with a Markforged X7 machine, with layers of continuous carbon fibre used where high rigidity is needed.

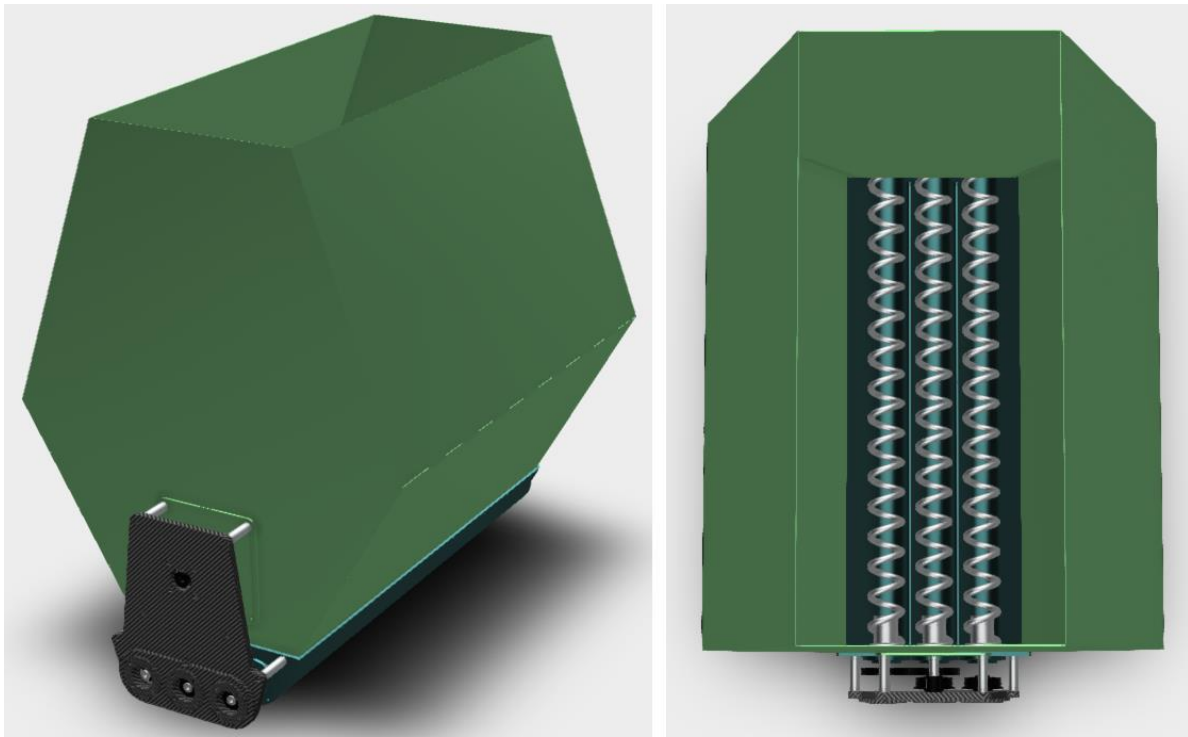


Figure D.6: Tracer particle distribution system, oblique view (left), top down view (right).

## Appendix E: Camera and flight parameter calculator

Some camera payloads require to be flown independently of the drone, so that they are essentially run in standalone ‘timelapse’ mode, rather than being triggered by the drone at regular distance intervals (which occurs for integrated camera gimbal packages). To facilitate calculations of flight speed, altitude, flight line spacing etc, a camera calculator excel spreadsheet was created. This spreadsheet has also been released through the GitHub repository and can be easily modified to include cameras payloads with other field of view and frame rate characteristics. Some camera examples are provided in Figure E.1, with camera constants entered at the top of the spreadsheet and variables such as desired flight altitude, image interval (i.e. 1/frame rate), and overlap entered in the middle of the spreadsheet. The camera and flight parameter calculator is mainly used for planning aerial surveying missions, however it can also be useful for calculating ground sample distance (i.e. pixel resolution) and image footprint size for surface velocimetry videos. If used for videos, care should be taken to input the correct resolution and field of view that the video is recorded in, as this will often differ from the full camera field of view and resolution used for capturing images.

Link: [https://github.com/HamishBiggs/DroneFlow/tree/Camera\\_FoV\\_and\\_Flight\\_Calculator](https://github.com/HamishBiggs/DroneFlow/tree/Camera_FoV_and_Flight_Calculator)

	Phantom RGB	X5S RGB	X5S RGB	SONY A5100 RGB	XTR Thermal	Stereo 35mm	Stereo 12mm	Hyperspec
Pixels wide	5472	5280	5280	6000	640	2448	2448	900
Pixels high	3648	3956	3956	4000	512	2048	2048	1
Diagonal FOV (degrees) [if known]	84	72	27	110				
Horizontal FOV (degrees) [if known]					69	14.33062	40.27261	36.5
Vertical FOV (degrees) [if known]					56	10.7725	30.7525	
Calculated HFOV (degrees)	73.67974	60.35132551	21.751733	99.83577712	69	14.33062	40.27261	36.5
Calculated VFOV (degrees)	53.08007	47.08007741	16.383372	76.77210654	56	10.7725	30.7525	0.04198514
Image format	3 to 2	4 to 3	4 to 3	3 to 2	5 to 4	~6 to 5	~6 to 5	900 to 1
Max frame rate (Hz)	0.5	0.5	0.5	1	0.5	10	10	249
		Panasonic Lumix G Leica DG Summilux 15mm f/1.7 ASPH	Olympus M.Zuiko Digital 45mm F1.8	VOIGTLANDER 15MM 4.5 E SUPER WIDE				
Notes								
Launch site altitude (m)	0	0	0	0	0	0	0	0
Desired altitude AGL (m)	60	80	80	80	120	20	50	100
Front overlap (%)	80	80	80	84	80	80	80	0
Side overlap (%)	60	60	60	68.4	60	60	60	50
Image interval to use (s)	2	2	2	2	2	0.5	1	0.01
Flight speed to use (m/s)	6	5	5	10	6	10	10	8
Camera landscape (L) or Portrait (P)*	L	L	L	L	L	P	L	L
Altitude to set AGL (m)	60	80	80	80	120	20	50	100
Min image interval (s)	2	2	2	1	2	0.1	0.1	0.00401606
Camera Mega Pixels (MP)	19.96186	20.88768	20.88768	24	0.32768	5.013504	5.013504	0.0009
Ground sample distance (cm)	1.642942	1.761955723	0.5822208	3.168775918	25.77304	0.154062	1.497821	7.32778994
Image horizontal footprint (m)	89.90177	93.0312622	30.741256	190.1265551	164.9474	3.771428	36.66667	65.9501094
Image vertical footprint (m)	59.93452	69.70296842	23.032653	126.7510367	127.6103	5.028572	27.5	0.0732779
Max flight speed(m/s)	5.993452	6.970296842	2.3032653	20.28016588	12.76103	10.05714	55	18.2461969
Distance between flight lines (m)	35.96071	37.21250488	12.296502	60.07999141	65.97897	1.508571	14.66667	32.9750547
Flight speed for [Image interval to use]	5.993452	6.970296842	2.3032653	10.14008294	12.76103	2.011429	5.5	7.32778994
Image interval for [Flight speed to use]	1.997817	2.788118737	0.9213061	2.028016588	4.253675	0.100571	0.55	0.00915974
Image framerate for [Flight speed to us]	0.500546	0.358664782	1.0854155	0.493092614	0.235091	9.943181	1.818182	109.173435

Figure E.1: Example of the camera and flight parameter calculator with constants, variables, and outputs.